ECAP-2016-026

Characterisation of Silicon Photomultipliers with Xenon Scintillation Light for the nEXO Experiment

Master's Thesis

submitted by

Tobias Ziegler

November 21, 2016

performed at

Erlangen Centre for Astroparticle Physics
Friedrich-Alexander-Universität Erlangen-Nürnberg

Supervisor: PD. Dr. T. Michel
Prof. Dr. G. Anton

ERLANGEN CENTRE FOR ASTROPARTICLE PHYSICS

FRIEDRICH-ALEXANDER UNIVERSITÄT ERLANGEN-NÜRNBERG

Contents

Introduction

Neutrinos — the only uncharged leptons in the Standard Model of particle physics are still subject of recent research. Early experiments in the 1950s and '60s provided experimental evidence of the existence of the particle [1], which had been postulated in 1930 by W. Pauli. The observation of neutrino oscillations [2, 3] during the past decades has established a new field of research in particle physics. Since neutrino oscillations require massive neutrinos, which are not incorporated in the Standard Model, the field of research referring to this observation is known as "Physics beyond the Standard Model". Several basic properties of massive neutrinos remain unresolved to this day, like the neutrino mass hierarchy, the absolute mass scale as well as the question whether or not the neutrino is its own anti-particle. The latter question originated in Majorana's new mathematical method of describing neutrinos formulated in 1937 [4]. Its implication contradicts the previous hypothesis of leptons possessing each a specific associated anti-particle. A confirmation of the Majorana nature of neutrinos would have a fundamental impact on our understanding of particle physics and on the evolution of the universe.

To establish the nature of neutrinos, the neutrinoless double beta decay provides the best prospect of success. The nEXO experiment ("new Enriched Xenon Observatory") is a future multi-tonne low-background experiment dedicated to the search for the neutrinoless double beta decay of ^{136}Xe, whose observation would provide evidence of the Majorana nature of neutrinos. The next-generation experiment will use enriched xenon on a tonne-scale to increase its sensitivity drastically compared to current experiments. The concept of the experiment was impressively demonstrated by its predecessor experiment EXO-200. Events are to be detected by collecting both ionisation and scintillation signal, analogously to EXO-200. The detector will be a single-phase time projection chamber filled with liquid xenon. The nEXO experiment will deploy more advanced detector technologies compared to its predecessor in order to maximise the physics potential of the experiment.

The nEXO experiment will use Silicon Photomultipliers (SiPMs) to detect UV-scintillation light emitted by xenon after an event has occurred. The aim of this thesis is to characterise several models of SiPMs in order to find a device that meets the strict requirements for the extremely low background experiment. A SiPM is based on a semi-conductor technology that allows to detect and resolve single photons. Compared to other, well-established types of photodetectors, SiPMs combine several advantages like the possibility for application in low background environments as required by the nEXO experiment. On the downside, this type of detector is typically not well-suited for the detection of UV-light. However, recent progress in the development of new technologies has enabled the detection of such wavelengths. The detection efficiency for UV-photons has increased during the past years, promising a suitable technology for the application in the nEXO experiment in the near future.

In this thesis, the neutrinoless double beta decay is reviewed shortly with a focus on the experimental approach to observing it, particularly with the nEXO experiment. Chapter 1 concludes with a discussion of the technology of SiPMs and its application in the nEXO experiment. In the following chapter, the setup which is used for the characterisation of SiPMs is presented as well as the specific detectors which are characterised. A focus of this thesis lies on the implementation of a C++ and ROOT based analysis software which is reviewed in chapter 3. The two subsequent chapters discuss the characterisation of the SiPMs. Chapter 4 addresses the characterisation in the absence of light whereas chapter 5 discusses the examination of the photon detection efficiency for UV-photons.

Chapter 1

Theoretical Background

Contents

In this chapter the background for the upcoming thesis is reviewed. The thesis is contextualised into a bigger physical scope. If you are familiar with the discussed topics feel free to skip this chapter.

At first the neutrinoless double beta decay ($0\nu\beta\beta$ decay) and its implication on nuclear physics are discussed. Demands for a competitive experiment are given as well as a list of suitable nuclei. Important experiments in data-taking or in research and development (R&D) phase are given.

The chapter proceeds with a review of the nEXO experiment which is a next-generation $0\nu\beta\beta$ decay experiment. Its design and working principle are explained and improvements in comparison to its predecessor, EXO-200, are outlined. The physical reach of nEXO is discussed shortly and integrated into the field of research.

Silicon Photomultipliers (SiPMs) will be used in nEXO as photodetectors and are characterised in this thesis. Here, the functionality of this novel type of photon detectors is explained. SiPMs are compared with different types of photon detectors regarding several criteria. The chapter concludes with a discussion of the requirements of SiPMs for the future nEXO experiment.

1.1 Neutrinoless Double Beta Decay

1.1.1 Basic Physical Concepts

The beta decay is a well known physical process in which a neutron in an atomic nucleus decays into a proton. The atomic number Z of a mother nucleus X is increased by one after the decay into a daughter nucleus Y (see equation (1.1)). The mass number A remains the same. Besides the emission of an electron, an electron anti-neutrino is emitted. This particle was first postulated by W. Pauli in 1930 followed by a complete theory on the beta decay by E. Fermi in 1933.

$$ {}^{A}_{Z}\mathrm{X} \rightarrow {}^{A}_{Z+1}\mathrm{Y} + e^- + \bar{\nu}_e \tag{1.1} $$

The energy difference between initial and final states is called Q-value. Using the Bethe-Weizsäcker-Formula one can compute the binding energy E_B of an atomic nucleus [5]:

$$ E_B = a_V A - a_S A^{2/3} - a_F \left(N - Z\right)^2 \cdot A^{-1} - a_C Z^2 \cdot A^{-1/3} + \delta \cdot a_P A^{-1/2} \tag{1.2} $$

where a_X denote constant factors and N the number of neutrons in the nucleus. Nuclei having even numbers of both protons and neutrons are called even-even-nuclei. For these nuclei applies $\delta = +1$, for odd-odd-nuclei $\delta = -1$ and $\delta = 0$ otherwise. This results in a higher binding energy for even-even-nuclei as can be seen in figure 1.1. If the binding energy of the mother nucleus is lower than that of the related daughter nucleus the beta decay is energetically forbidden. In this case the mother nucleus is either stable or capable of a second-order decay called double beta decay ($2\nu\beta\beta$ decay) which was first described by M. Goeppert-Mayer in 1935 [7]. In this decay two neutrons decay quasi simultaneously within one process into two protons in the nucleus. The chemical transition is shown in equation (1.3). The corresponding Feynman diagram is shown in figure 1.2a.

$$ {}^{A}_{Z}\mathrm{X} \rightarrow {}^{A}_{Z+2}\mathrm{Y} + 2e^- + 2\bar{\nu}_e \tag{1.3} $$

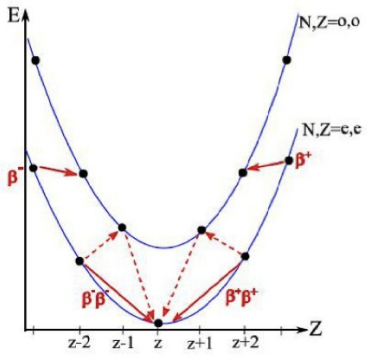

Figure 1.1: Mass parabolae calculated with the Weizsäcker-Formula. The upper parabola corresponds to odd-odd-nuclei. The lower parabola corresponds to even-even-nuclei. Decays into daughter nuclei with lower energies are allowed whereas those into daughter nuclei with higher energies are not. Picture taken from [6].

This decay is higly suppressed due to the additional vertices but it was observed by several experiments for a variety of $2\nu\beta\beta$ decay-nuclei. The first direct observation of the $2\nu\beta\beta$ decay succeeded in 1987 by M. Moe using ^{82}Se and measured a half-life of $T_{1/2} = 1.1^{+0.8}_{-0.3} \cdot 10^{20}\,\mathrm{yr}$ (68 % C.L.) [8]. Since then many experiments have measured the half-life of the $2\nu\beta\beta$ decay of several nuclei.

A modification of the $2\nu\beta\beta$ decay is the so called $0\nu\beta\beta$ decay[1]. A subgroup of the Heidelberg-Moscow Collaboration published a first observation of this decay [10] that was highly controversial within the community [11] and that was disconfirmed by several recent experiments. Hence the $0\nu\beta\beta$ decay remains a hypothetical decay. The corresponding Feynman diagram is shown in figure 1.2b. In this scenario no neutrino is emitted by the nucleus. This can be explained illustratively by the emission of one anti-neutrino at one vertex and the absorbtion of it as a neutrino at the other vertex. In reality the process is much more complicated [9]. The simplified explanation uses the condition of neutrinos being their own anti-particles, i.e. $\nu = \bar{\nu}$, resulting in neutrinos being Majorana particles [4]. Furthermore neutrinos must have mass to be able to flip their helicity. Helicity is the projection of the spin $\vec{S}$ of a particle with respect to its direction of motion $\hat{p}$. This condition must be met because the weak interaction only couples to left-handed particles and right-handed anti-particles. Recent experiments have observed neutrino oscillations between different neutrino flavours which imply that neutrinos have mass. Thereby neutrinos are able to flip their helicity [2, 3, 12].

The half-life of nuclei that can undergo $0\nu\beta\beta$ decay can be calculated as follows [13]:

$$\left(T_{1/2}\right)^{-1}_{0\nu\beta\beta} = G_{0\nu}\left(Q_{\beta\beta}, Z\right) \cdot \left|M_{0\nu}\right|^2 \cdot m^2_{\beta\beta} \tag{1.4}$$

where $G_{0\nu}\left(Q_{\beta\beta}, Z\right)$ denotes the phase space factor of the $0\nu\beta\beta$ decay which can be calculated with relatively little uncertainty. $M_{0\nu}$ corresponds to the nuclear matrix element (NME) which is calculated based on nuclear models containing the kinematics of the decay. Depending on

[1] The explanations given here only consider the exchange of a light Majorana neutrino. The discussion on non-standard scenarios like emission of heavy neutrinos or neutralinos or the emission of Majorons lie beyond the scope of this work and can be reviewed in suitable literature like for example [9].

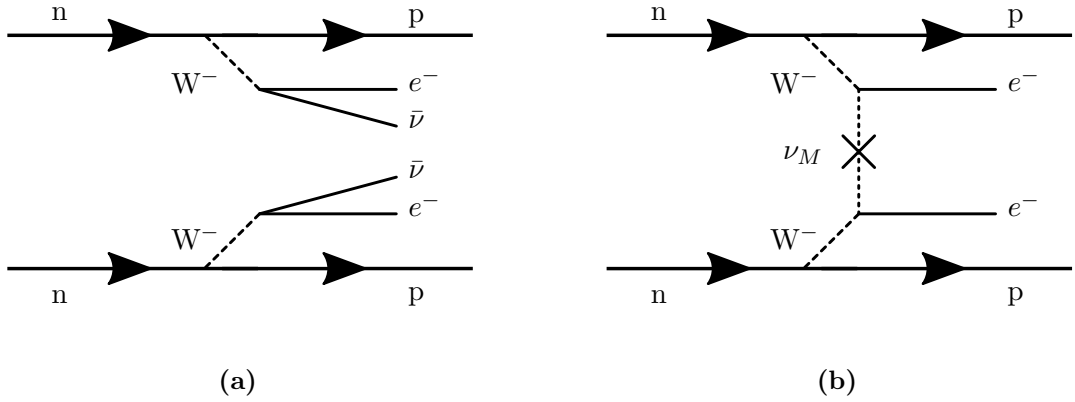

Figure 1.2: Feynman diagrams of the $2\nu\beta\beta$ decay **(a)** and of the $0\nu\beta\beta$ decay **(a)**.

the applied model, the results can vary notably. The main techniques being used are: ISM, QRBA, IBM, GCM [14–16]. $m_{\beta\beta}$ is the effective Majorana mass. Neutrino oscillations imply a difference between mass eigenstates and flavour eigenstates of neutrinos. The electron neutrino ν_e for example is a mixture of the three mass eigenstates ν_1, ν_2 and ν_3. Both eigenstate spaces are connected via a rotational matrix U. Using the entries of this matrix that correspond to the electron neutrino U_{ei} along with the corresponding mass eigenstates m_i, one can calculate the effective Majorana mass [14]:

$$m_{\beta\beta} = \left| \sum_{i=1}^{3} m_i U_{ei}^2 \right| \tag{1.5}$$

Using equation (1.4) it is possible to relate the half-life directly to the Majorana mass. This enables to compare the sensitivities of experiments that use different nuclei, since the Majorana mass is independent on the used nuclei.

1.1.2 Implications on Theoretical Physics

There are many reasons why experiments are looking for the $0\nu\beta\beta$ decay. Besides the mere discovery of a new decay channel, the $0\nu\beta\beta$ decay can provide answers to several questions in both nuclear and neutrino physics.

As seen in equation (1.4) the measured half-life of the $0\nu\beta\beta$ decay can be connected directly to an effective Majorana neutrino mass[2]. Measurements of neutrino oscilllations are only sensitive to the three (squared) mass differences Δm_{12}^2, $\left|\Delta m_{13}^2\right|$ and $\left|\Delta m_{23}^2\right|$ with $\Delta m_{ij}^2 = m_i^2 - m_j^2$ [17]. The sign of Δm_{12}^2 can be deduced from matter effects yielding $m_2^2 > m_1^2$. Since the signs of both other squared mass differences are still unknown two mass hierarchies could be realised in nature (see also figure 1.3):

- The so-called normal hierarchy where $m_1 < m_2 < m_3$
- The inverted hierarchy where $m_3 < m_1 < m_2$

Measuring the half-life of the $0\nu\beta\beta$ decay and thus the effective neutrino mass one can get additional constraints on the mass hierarchy and may be able to identify which of the two mass hierarchies is realised in nature. Furthermore one can obtain constraints on the absolute neutrino mass scale from measuring the half-life of the $0\nu\beta\beta$ decay.

As mentioned in the previous section, the conditions for a $0\nu\beta\beta$ decay are firstly that neutrinos have mass and secondly that they are Majorana particles. Both conditions lead to physics beyond the Standard Model. The latter condition implies neutrinos being their own anti-particles. It was shown by Schechter and Valle in 1982 [18] that regardless of the exact mechanism of the $0\nu\beta\beta$ decay the conclusion $\nu = \bar{\nu}$ holds if the decay exists. Proving the Majorana nature of neutrinos would give rise to leptogenesis and could help understanding the asymmetry between matter and antimatter in the Universe.

[2] The uncertainties and fluctuations of the calculation of the NME result in an uncertainty of 20 - 30 % when converting half-life to neutrino mass [14]

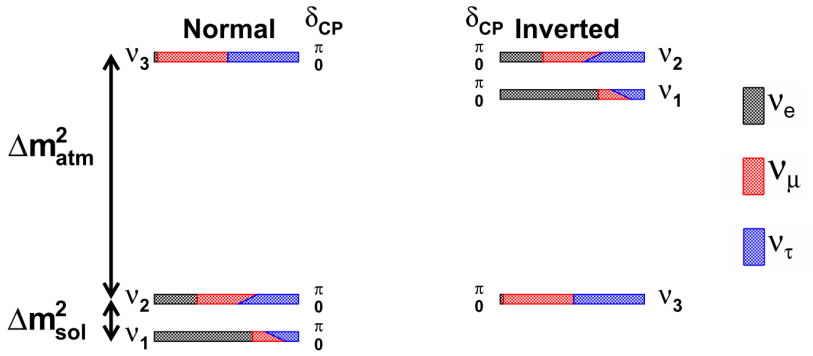

Figure 1.3: Possible neutrino hierarchies. Since only $m_2 > m_1$ is known by sign two hierarchies are possible. The normal hierarchy with $m_3 > m_2 > m_1$ and the inverted one with $m_2 > m_1 > m_3$. The colours denote the flavour compositions of the particular mass eigenstates as function of the unknown CP phase δ_{CP}. The squared mass difference Δm^2_{21} is measured using solar neutrinos and the Δm^2_{32} is measured using atmospheric neutrinos. Picture taken from [17].

1.1.3 Experimental Approach

As seen in the section so far, the $0\nu\beta\beta$ decay is an extremely rare decay, if it even exists. In order to be able to detect this process within a reasonable time, experiments must use large decay masses. Current experiments use decay masses of 10 - 100 kg. Next generation experiments will increase these decay masses by at least one order of magnitude. In order to have maximum sensitivity on a potential $0\nu\beta\beta$ decay, most experiments look for multiple signatures that indicate the decay. The most important one is the sum energy of both emitted electrons of the decay. Only with good energy resolution one can discriminate between a possible $0\nu\beta\beta$ decay and a $2\nu\beta\beta$ decay. In addition, the decay topology and particle identification are used to distinguish signal (meaning events from $2\nu\beta\beta$ decay and from $0\nu\beta\beta$ decay) from background. The latter arises for example from decays of natural radioactivity or cosmogenics. More advanced methods like observing the resulting daughter nucleus could increase the sensitivity significantly. However, these methods are technically challenging.

The energy spectra of the sum of both emitted electrons of the $2\nu\beta\beta$ decay and of the hypothetical $0\nu\beta\beta$ decay are shown schematically in figure 1.4. On the one hand, the spectrum of the $2\nu\beta\beta$ decay is continuous since a part of the energy is transferred to the anti-neutrinos, that cannot be detected. Thus the summed energy of both electrons cannot reach the Q-value. On the other hand, the spectrum of the $0\nu\beta\beta$ decay is discrete at the Q-value since all the released energy is transferred to the electrons.

All nuclei that are capable of the $0\nu\beta\beta$ decay are also capable of the $2\nu\beta\beta$ decay. Therefore, this background cannot be suppressed by extrinsic means. In order to limit this intrinsic background experiments aim at an energy resolution that is as high as possible. The energy resolution Res (E_0) is defined as the width ΔE of a broadened mono-energetic signal rescaled by its energy E_0. In the Gaussian case the mono-energetic signal blurs as shown in equation (1.6).

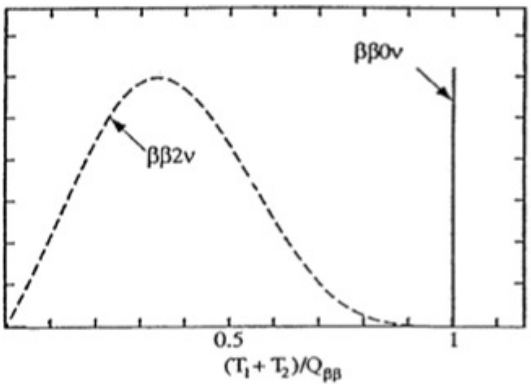

Figure 1.4: Sum energy spectrum of the emitted electrons from the $2\nu\beta\beta$ decay and from the $0\nu\beta\beta$ decay. The former is continous since the neutrinos carry some of the energy. The latter is discrete since only two electrons are emitted that carry all the energy which equals Q. The relative height of both spectra is not to scale. Plot taken from [6].

A higher energy resolution $\mathrm{Res}\,(E_0) = \frac{\Delta E}{E_0}$ allows to discriminate signals that lie in close proximity.

$$\delta\,(E - E_0) \longrightarrow \frac{1}{\sqrt{2\pi\Delta E}} \exp\left(\frac{(E - E_0)^2}{2\,(\Delta E)^2}\right) \tag{1.6}$$

Keeping in mind that the decay ratio of both decays is at least $\sim 10 \cdot 10^6$ yielding on average about $\sim 10 \cdot 10^6$ intrinsic background events from $2\nu\beta\beta$ decays per one $0\nu\beta\beta$ decay event. The only way of discriminating between both decays is energy resolution. For that reason it is essential – but not sufficient – to achieve a high energy resolution.

A main issue for experiments looking for the $0\nu\beta\beta$ decay is background. An important value in this subject is the background b in an energy window ΔE around the Q-value. It is defined as [19]:

$$b = c \cdot Mt \cdot \Delta E \tag{1.7}$$

where c denotes the background rate in ($\#\,{}^{\mathrm{counts}}/_{\mathrm{keV\cdot kg\cdot yr}}$) and Mt the overall exposure of the decay mass M. Dominant background components arise from natural decay chains that originate in small impurities within the detector material and in material surrounding the experiment. Natural radioactivity of detector components is a main background component as well. Further background can arise from natural ^{220}Rn or ^{222}Rn, from atmospheric mouns or from neutrons. External background is shielded by operating the experiments underground and by using passive or active veto systems [14].

The main goal in designing an experiment is to maximise the sensitivity[3] to the $0\nu\beta\beta$ decay. In case no $0\nu\beta\beta$ decay is observed this results in an upper limit on the decay rate $\left(T_{1/2}\right)^{-1}_{0\nu\beta\beta}$ which can be translated to an upper limit on the effective Majorana mass $m_{\beta\beta}$ (see equation (1.4)).

[3]This quantity describes an average upper limit on $\left(T_{1/2}\right)^{-1}_{0\nu\beta\beta}$ when performing the experiment or a simulation of the experiment many times.

For the idealised case of no background the upper limit improves with $(Mt)^{-1/2}$ [19]:

$$m_{\beta\beta} \sim \sqrt{\frac{1}{\epsilon}} \cdot \left(\frac{1}{Mt}\right)^{1/2} \tag{1.8}$$

The signal detection efficency is denoted by ϵ. In the more realistic case with a certain background b the sensitivity on $m_{\beta\beta}$ changes with $(Mt)^{-1/4}$ [19]:

$$m_{\beta\beta} \sim \sqrt{\frac{1}{\epsilon}} \cdot \left(\frac{c\Delta E}{Mt}\right)^{1/4} \tag{1.9}$$

This consideration implies clearly the severe influence of both high background and bad energy resolution on the sensitivity and hence on the performance of experiments. Hence both characteristics have to meet excellent standards in order to maximise the physical capabilities of an experiment.

As seen so far, designing a reasonable experiment is a multi feature task. Both technical and financial limitations require trade-offs. A perfect example is the choice of the deployed nuclei. Some of the 35 suitable nuclei have conveniently high natural abundances but suffer low Q-values where natural radioactivity is worse. Therefore, different experiments use different nuclei depending on their focus. A list of the most often used nuclei is given in table 1.1. The focuses of an experiment can be for example excellent energy resolution or background suppression. An overview of recent and proposed experiments is given in table 1.2 together with their achieved lower limits on the half-life of the $0\nu\beta\beta$ decay of the associated nuclei.

Table 1.1: Overview of the most important nuclei used for the search for the $0\nu\beta\beta$ decay. The abundancies are taken from [20]. Q-values and half-life limits are taken from the references given, respectively.

Nucleus	$Q_{\beta\beta}$ [keV]	Natural Abundance [%]	Current half-life limit (90 % C.L.) [a]
^{48}Ca	4272	0.187	$5.8 \cdot 10^{22}$ [21]
^{76}Ge	2039	7.75	$3.0 \cdot 10^{25}$ [22]
^{82}Se	2995	8.82	$3.6 \cdot 10^{23}$ [23]
^{96}Zr	3350	2.80	$9.2 \cdot 10^{21}$ [23]
^{100}Mo	3034	9.74	$1.1 \cdot 10^{24}$ [24]
^{116}Cd	2805	7.51	$1.7 \cdot 10^{23}$ [25]
^{130}Te	1528	34.08	$3.0 \cdot 10^{24}$ [26]
^{136}Xe	2458	8.86	$1.1 \cdot 10^{26}$ [27]
^{150}Nd	3368	5.64	$2.0 \cdot 10^{22}$ [28]

Table 1.2: A selection of recent and granted experiments. The used nuclei with their isotopic mass are given as well as the (targeted) energy resolution at the Q-value. For further information see the given references.

Experiment	Nucleus	Isotopic Mass [kg]	Energy Resolution FWHM at Q [%]	Important Publications
CUORE	^{130}Te	206	0.33	[29, 30]
EXO-200	^{136}Xe	141	1.53	[31–33]
GERDA	^{76}Ge	35	0.15	[22, 34]
KAMLAND-Zen	^{136}Xe	343	4.66	[27, 35, 36]
NEMO3	^{48}Ca	0.007	6.8-8.6	[23, 24, 37–39]
	^{82}Se	0.932	8.2-10.2	
	^{96}Zr	0.0094	7.7-9.7	
	^{100}Mo	6.914	8.1-10.2	
	^{116}Cd	0.405	8.4-10.6	
	^{130}Te	0.454	11.4-14.3	
	^{150}Nd	0.0366	7.7-9.6	
NEXT	^{136}Xe	100	< 1	[40, 41]

1.2 The nEXO Experiment

The nEXO experiment is the successor of the EXO-200 experiment. The experiment is now in the R&D phase and benefits from the sophisticated design of EXO-200. Like in the predecessor experiment the detector will be a single-phase time projection chamber (TPC) filled with liquid xenon (LXe). The xenon will be enriched to about 90 % with ^{136}Xe which is capable of the $2\nu\beta\beta$ decay and therefore a candidate for the $0\nu\beta\beta$ decay. Hence, xenon is used as source and detection medium simultaneously. Events are detected by collecting both ionisation and scintillation signals and are fully reconstructed using these signals. This feature and the monolithic structure of the nEXO detector enables excellent background rejection. Besides technical improvements compared to EXO-200, nEXO will scale up in xenon mass from 200 kg to 5000 kg. The experiment will probably be placed underground in the SNOLAB in Canada [42].

1.2.1 Conceptual Design

The TPC of nEXO is a cylindrical vessel made out of copper with a height of 1.3 m and a diameter of 1.3 m. It will be placed inside a cryostat filled with HFE [43] keeping the temperature of the LXe at a constant level of around −110 °C. The cryostat is embedded into a vacuum sphere to isolate the cryostat thermally. This sphere is surrounded by a big water tank which serves as passive and active veto against cosmic rays. The conceptual design as an artist view of the nEXO-experiment is shown in figure 1.5. To achieve a high level of radiopurity the usage of materials is kept to a minimum. The experiment benefits from the increased xenon mass because external background events are shielded by the xenon near the surfaces leaving the inner part of the detector extremely clean. The experiment will be placed underground at a depth of 6000 metre water equivalent (mwe) in order to sufficiently shield cosmogenic background.

The signal in nEXO is detected using two different types of detector systems. One is designed for detecting xenon scintillation light and the other one for detecting charge carriers. Charge emerges from ionisation processes and the charge carriers are separated by a homogeneous electric field. Field shaping rings on the wall of the TPC keep the electric field homogeneous throughout the entire TPC. The conceptual design of the TPC is shown in figure 1.5.

Negative charge carriers, i.e. electrons, are drifted to charge readout tiles on the anode plane on the top surface of the TPC. To achieve this, the xenon has to be extremely clean so that the charge carriers are not absorbed by impurities. The pad-like quadratic readout tiles with a 3 mm pitch detect the currents induced by the charge carriers drifting towards the tiles. Thereby, both the (x, y)-coordinates of an event can be derived as well as the energy deposited in secondary charge carriers. The modules are connected in a diagonal pattern which provides spatial resolution and decreases the number of channels. The signal is processed inside the TPC at cryogenic temperatures which reduces noise due to shorter cable lengths and thus smaller capacitances. These two measures are taken also to reduce the number of cables and feedthroughs and thus intrinsic radioactivity as well as to simplify the construction of the detector.

The scintillation light is detected using SiPMs which are novel detectors for single photon detection (see section 1.3). The SiPMs will be placed on the inner wall of the TPC behind the field shaping rings and will cover an area of about $4\,\mathrm{m}^2$. To simplify the implementation of all SiPMs and to reduce the number of feedthroughs and cables due to radiopurity concerns, the SiPMs will be mechanically ganged to groups of about 64 chips. The signals from these modules will also be processed inside the TPC. In the current status of the experimental design, the signals from the SiPMs are only used to count photons and not to reconstruct the position of an event.

The attenuation length of a gamma photon with an energy near the Q-value is about 8.5 cm. Relating this range with the diameter of the nEXO detector of 1.3 m, the capability of shielding external and surface background with the outer part of the LXe in the TPC will be enhanced drastically compared to EXO-200 which has a diameter of only 0.4 m. This feature is called self-shielding and leaves the inner part of the volume of the TPC which is called fiducial volume extremely clean. By restricting the final $0\nu\beta\beta$ decay analysis to the fiducial volume the background contribution can be reduced significantly.

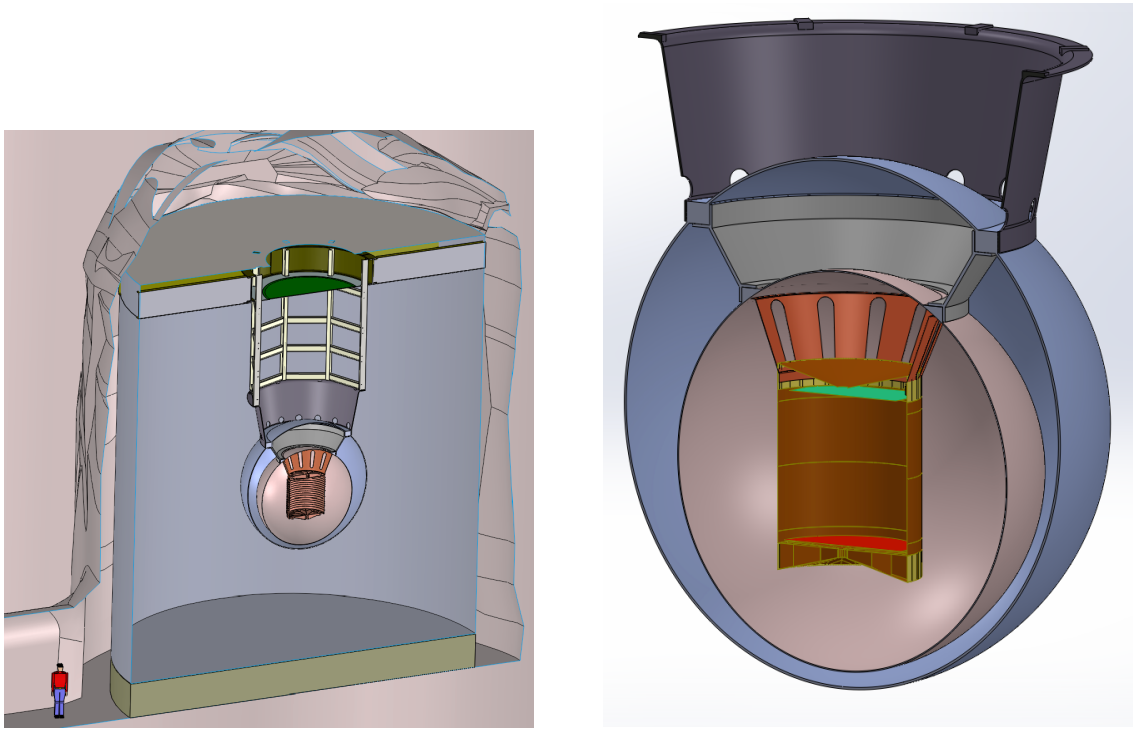

(a) **(b)**

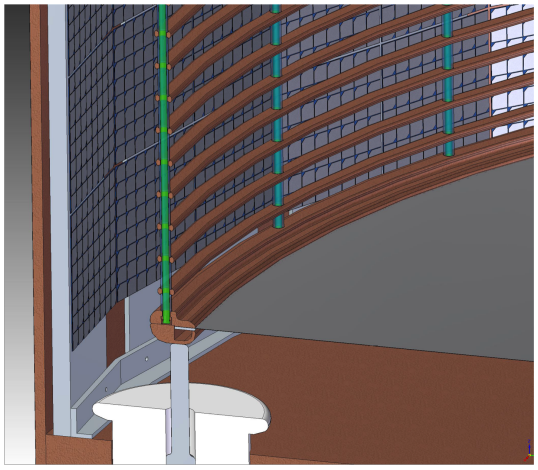

(c)

Figure 1.5: (a-c) Artist's view of the conceptual design of the nEXO experiment in SNOLAB. The red and green planes in **(b)** indicate the anode and cathode plane respectively. The detector (brown cylinder) is embedded in a cryostat (grey sphere). This is surrounded by an evacuated sphere (blue) isolating the cryostat thermally from periphery. The complete setup **(a)** is embedded in a big water tank which serves as veto against external background [44]. **(c)** shows the zoom into the TPC that will be made of copper (brown). The plane indicates the charge collection tiles. The grey panels on the lateral surface show the SiPM modules which are located behind the field shaping rings (brown).

1.2.2 Working Principle

When a $0\nu\beta\beta$ decay candidate event occurs inside the TPC, both emitted electrons propagate through the surrounding xenon. Along their path they ionise and excite xenon atoms leaving a number of N_i xenon ions Xe^+ and N_ex excited xenon atoms $\mathrm{Xe}^\star$ behind. The energy E_0 deposited by the electrons is transferred to both processes and can be written as [45]:

$$E_0 = N_\mathrm{i} E_\mathrm{i} + N_\mathrm{ex} E_\mathrm{ex} + N_\mathrm{i}\epsilon \tag{1.10}$$

where E_i and E_ex corresponds to the mean energy for ionising and exciting a xenon atom, respectively. ϵ denotes the kinetic energy of the electrons after ionisation. The xenon ions Xe^+ convert to excited atoms $\mathrm{Xe}^\star$ in a multi-stage process. These form excited dimers $\mathrm{Xe}_2^\star$ which decay to the ground state by emitting UV-scintillation light with a peak wavelength of 178 nm [46]. Since both processes lead to excited dimers $\mathrm{Xe}_2^\star$, the resulting scintillation light is independent of the initial process. For gaseous xenon (GXe) the peak wavelength of the scintillation light is 175 nm [46]. The mean energy to produce a scintillation photon is given by [45]:

$$W_\mathrm{ph} = \frac{E_0}{N_\mathrm{ph}} \leq \frac{W_\mathrm{i}}{1 + \frac{N_\mathrm{ex}}{N_\mathrm{i}}} \tag{1.11}$$

where $W_\mathrm{i} = {}^{E_0}/_{N_\mathrm{i}}$ denotes the average energy to produce a xenon ion. The value of W_ph is minimal and equals the last term in the absence of an electric field and for a vanishing recombination probability. The value increases for any photon reduction process like quenching or impurities in the xenon. Furthermore, W_ph depends on the type of particle that deposits energy in xenon. For β-particles W_ph is 21.6 eV while for α-particles W_ph is 17.9 eV [45]. Using the equation above, it is possible to deduce the deposited energy E_0 by measuring the number of scintillation photons N_ph. For example, in the case of a candidate $0\nu\beta\beta$ decay event, there will be around 115 000 photons which are emitted isotropically. Both the number of scintillation photons and the number of charge carriers fluctuate. Since both fluctuations are complementary and anti-correlated the fluctuation of the sum signal decreases. Thereby, the energy resolution increases drastically by combining both the signal from photons and from charge carriers [45].

As seen so far, the scintillation light will be detected with SiPMs covering a large fraction of the lateral surface of the TPC. The photons hitting a SiPM will be detected with a certain probability, called photon detection efficiency (PDE) (see section 1.3.1), producing an electric signal. The strength and the time stamp of this signal will be processed inside the TPC. The scintillation signal is detected almost instantaneously and determines the time stamp of the event. By knowing the PDE of the SiPM one can deduce the total amount of emitted photons.

The charge carriers are separated by an external electric field. The xenon ions drift slowly towards the cathode while the electrons drift towards the anode where the induced charge will be detected via charge readout tiles. Since the electrodes are pixelated one can determine the (x, y)-coordinates of the charge and thus the (x, y)-coordinates of the primary event. The z-coordinate can be derived via the time difference between the light signal and the charge signal.

The exact position of an event can help to classify the event. Most of the background events occur near the walls of the TPC due to extrinsic background or due to impurities in the walls.

Keeping this in mind these events are excluded for a search for the $0\nu\beta\beta$ decay. Using only events in the fiducial volume reduces the background drastically. This way the sensitivity to a possible $0\nu\beta\beta$ decay is increased. Another signature by which background can be excluded is the so called event multiplicity. Events which deposit charge in one spatial centre are called single site event (SS event) and other events with more than one spatial centre are called multi site event (MS event). $2\nu\beta\beta$ decay events and candidate $0\nu\beta\beta$ decay events are SS events since the paths of both electrons are not spatially resolved due to their small ranges of about 2 mm. High energy photon background from multiple Compton scattering for example will be detected as MS event and will be excluded for a $0\nu\beta\beta$ decay analysis. Another method to reduce background is by comparing the ratio of scintillation light to charge which makes it possible to identify the particle producing both signals. Cutting all events which do not originate from electrons one can exclude background even more stringent. Taking all these signatures into account, nEXO will not only be a pure calorimeter but it will use different techniques to reduce background and thus increase the sensitivity to a possible $0\nu\beta\beta$ decay. The projected energy resolution of nEXO is $\mathrm{Res}(Q) < 1\,\%$ [44].

1.2.3 Physics Goal

Every event passing the cuts presented in the previous section is taken into account. The resulting energy histogram will contain dominantly $2\nu\beta\beta$ decay events and some remaining background. With complex background estimations on the several background components one can model the spectrum and use this model to fit the measured spectrum in the region of interest (ROI) around the Q-value. This fit finally sheds light onto the question whether or not the $0\nu\beta\beta$ decay was observed. In both cases one can calculate the half life $\left(T_{1/2}\right)_{0\nu\beta\beta}$ or its lower limit. This result corresponds to an effective Majorana mass $m_{\beta\beta}$ or an upper limit, respectively. An example from EXO-200, is shown in figure 1.6.

With the improvements introduced in the previous section, the nEXO experiment will enhance the sensitivity on the half-life to about 10^{28} yr after 10 yr of data taking and even further with Ba-tagging compared to the projected final sensitivity of $5.7 \cdot 10^{25}$ yr of EXO-200 [44]. The sensitivity on the Majorana mass will be 5 - 15 meV after 10 yr without Ba-tagging depending on the applied NME [44]. Therefore, it will be possible to cover the complete inverted hierarchy. If nEXO is able to use Barium tagging in a Phase-II (for further information see [47]) the experiment would be virtually background free. The only remaining background component would be the intrinsic background of $2\nu\beta\beta$ decay which can only be identified via the deposited energy. The targeted sensitivities of nEXO and of EXO-200 are shown in figure 1.7

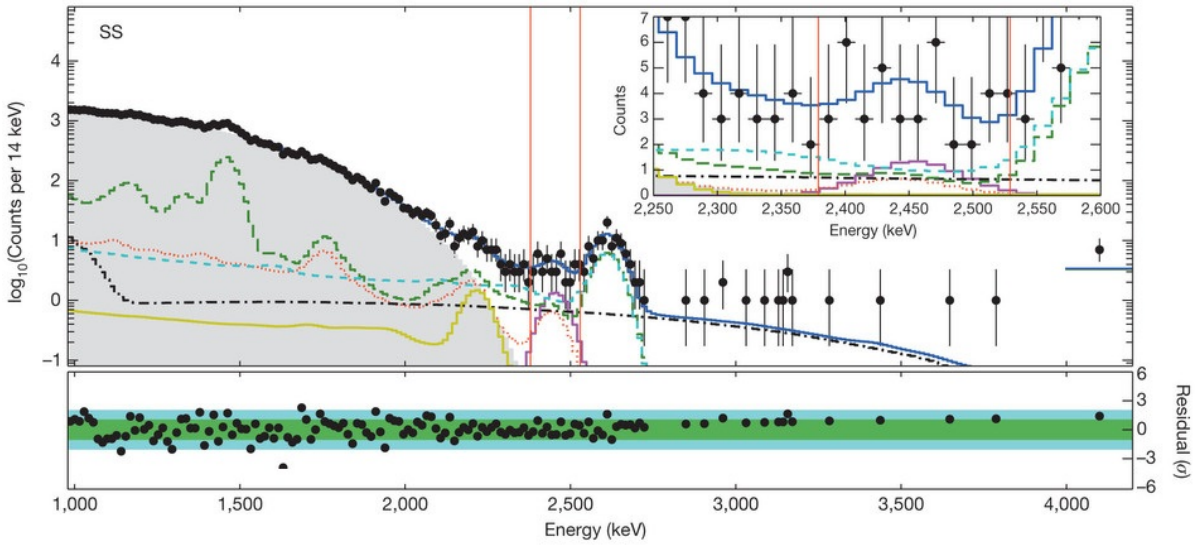

Figure 1.6: Energy spectrum of SS event events measured by EXO-200. The inset shows the spectrum around the ROI. Data points are shown in black. The different background model components and $2\nu\beta\beta$ decay model components are shown in dotted style and with grey area respectively. $0\nu\beta\beta$ decay events are shown in purple. The best fit is shown in blue and the residual is shown in the lower panel. This fit result is consistent with zero $0\nu\beta\beta$ decay events at $1.2\,\sigma$. Plot taken from [33].

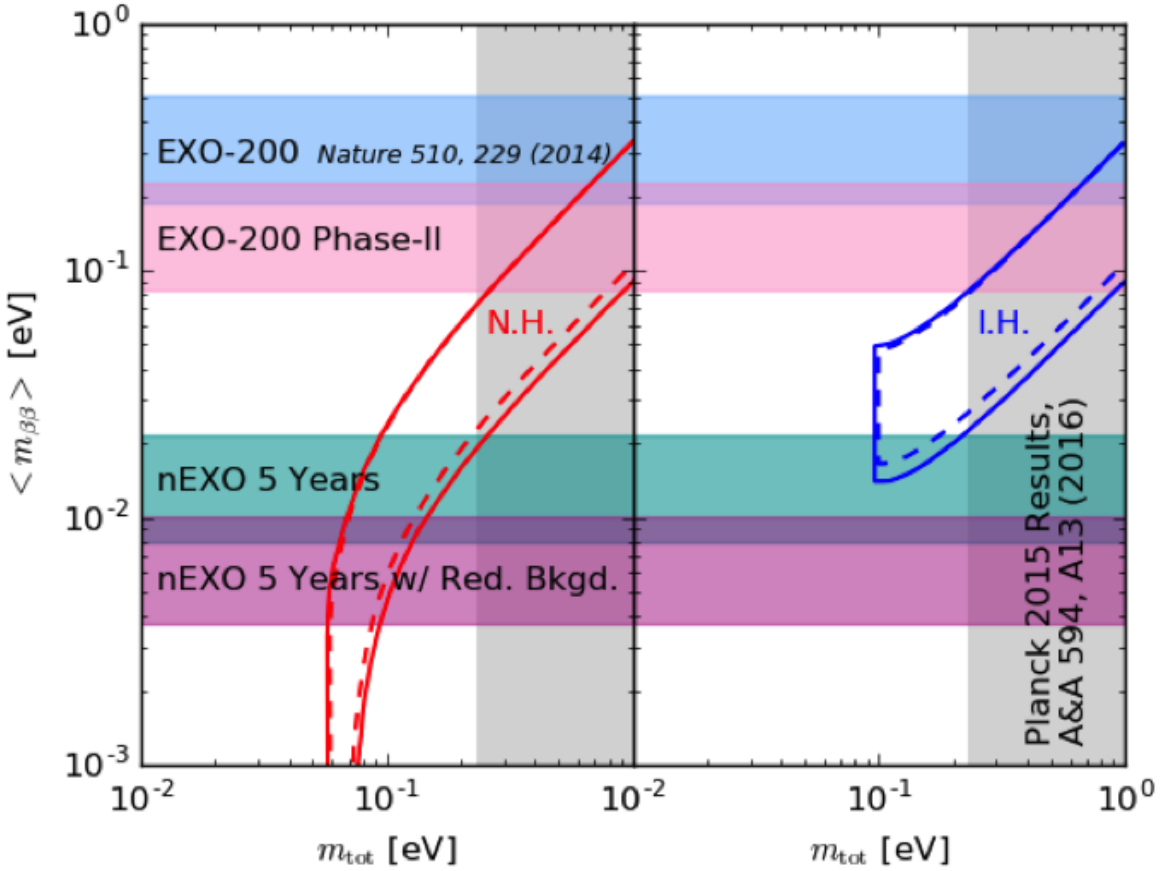

Figure 1.7: The targeted sensitivities on the Majorana mass of nEXO after 5 yr of data taking are shown. The grey area is excluded by cosmological measurements from Planck stating $\sum m_\nu < 0.23\,\text{eV}$ [48]. The red band (left) denotes the normal hierarchy whereas the blue band denotes the inverted one (right). nEXO will cover the inverted hierarchy completely with (purple) and without (green) Barium tagging. For the purpose of comparison, the current (*Nature 2014*) and the final (*Phase-II*) sensitivities of EXO-200 are shown.

1.3 Silicon Photomultipliers

1.3.1 Functionality of Silicon Photomultipliers

PN and PIN Photodiodes are semiconductor devices that convert light into current making it possible to detect photons. They consist of a p-n-junction in reverse bias mode. In order to reduce photon loss due to reflection the uppermost layer is an anti-reflective coating of SiO_2 or Si_3N_4 that matches the refraction index of silicon to the one of air. By doping an intrinsic semiconductor, most often pure silicon, with acceptor impurities a p-type semiconductor is created. It has a larger hole concentration than electron concentration. n-type semiconductors are doped with donor impurities resulting in a larger concentration of electrons than holes. The interface of a p-type and an n-type semiconductor is called p-n-junction. By operating the p-n-junction in reverse bias the depletion region is expanded and thus the electric field increases. Photons with sufficient energy greater than the bandgap of the semiconductor (about 1.1 eV for Si [49]) can be absorbed in the diode due to the photoelectric effect. In this case the electron is excited from the valence band to the conduction band producing an electron-hole pair. The interaction depths depends on the energy of the striking photon and can be in the p-, n- or depletion region. Electron-hole pairs far away from the depletion region recombine after a short amount of time and cannot contribute to a signal. However, pairs within the diffusion length of the depletion region or within this region are separated by the electric field and usually do not recombine. These charge carriers cause a so called drift current on the electrodes. The signal is proportional to the intensity of the incoming light.

A PIN-photodiode works in the same way as a PN-photodiode, its topology is shown in figure 1.8. The additional element is an intrinsic layer between the p-n layers, i, that is not doped. This leads to a much thicker depletion region resulting in a more efficient collection of charge carriers and thus in a higher quantum efficiency (QE).

Since neither of the devices uses internal amplification, the number of generated photoelectrons per incident photon is unity or less because of losses due to reflections or absorption in

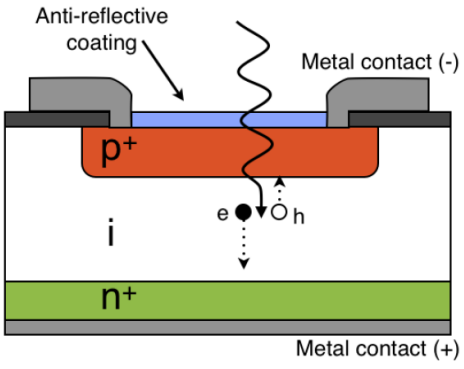

Figure 1.8: Doping profile and topology of a PIN-photodiode with the associated electric field shown on the right hand side. The bias voltage is provided by metal contacts on top of the device. The separation of a produced electron-hole pair is indicated. Adapted from [50].

inappropriate regions. Therefore, PN and PIN photodiodes can only be used with relatively high fluxes starting at a signal of about 200 photoelectrons [49].

Avalanche Photo Diodes work by the same detection principle like PN-photodiodes. The main difference is the higher reverse bias that leads to a stronger electric field in the depletion region. A photoelectron is accelerated in the electric field and gains enough kinetic energy to produce secondary electron-hole pairs in collisions with atoms due to impact ionisation. Holes do not gain enough energy to initiate secondary electron-hole pairs. This process occurs repeatedly resulting in a multiplication of the initial photocurrent as can be seen in figure 1.9a. The process responsible for the amplification of the current is called avalanche effect. By adjusting the reverse bias of the Avalanche Photo Diode (APD) one can adjust the gain of the device. However, exceeding the so-called breakdown voltage would lead to a higher production rate of electron-hole pairs than the rate of their extraction from the high-field region and thus to a self-sustained, exponential increase of the photocurrent which is shown in figure 1.9b. This performance is harmful the device and has to be prevented by adjusting the reverse bias carefully [50].

The most frequently used APD is the so-called "reach-through" structure. It consists of an absorption region and a multiplication region. The external electric field in the intrinsic absorption region separates the electron and hole from each other. The electrons are drifted towards the multiplication region where a high electric field for the avalanche process is provided. This structure provides a save performance where the multiplication of holes is kept at a minimum. The gain of each photoelectron is in the range of 50 - 200 and the resulting photocurrent is proportional to the intensity of the incoming light. Because of the internal amplification of photoelectrons, APDs are sensitive to intensities starting at about 10 photoelectrons [49].

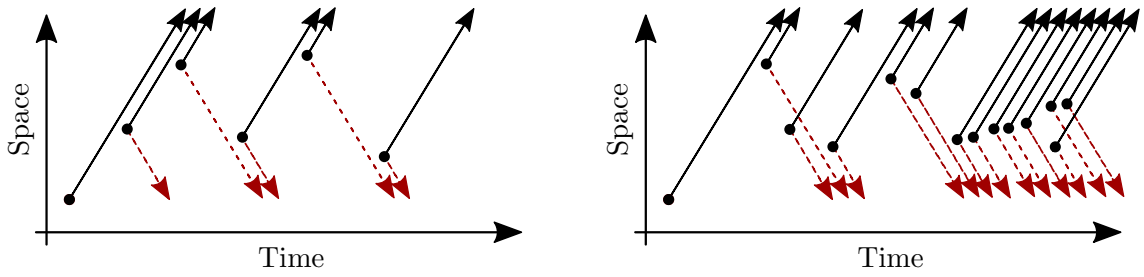

(a) **(b)**

Figure 1.9: Avalanche multiplication process shown in space-time diagrams. The primary photoelectron is on the left, the associated hole is not shown. Solid arrows depict electron trajectories and dashed ones hole trajectories. **(a)** shows a sub-critical avalanche process with a de-facto constant gain whereas **(b)** shows a critical avalanche corresponding to a voltage above the breakdown voltage. The current grows at a exponential rate. Adapted from [51].

Single Photon Avalanche Photodiodes are novel configurations of an APDs. These devices are sometimes referred to as Geiger-Mode Avalanche Photodiodes (GM-APDs). The topology with its electric field is shown in figure 1.10 as it was proposed by Haitz [52, 53] and McIntyre [54, 55]. The main difference to APDs is a bias voltage exceeding the breakdown voltage by a so called overvoltage of:

$$\Delta U = |U_{\text{Bias}} - U_{\text{Break}}| \tag{1.12}$$

This mode of operation is called "Geiger-mode" and its mechanism is shown qualitatively in figure 1.11. A feature of this mode is, when triggered, an ionisation rate larger than the extraction rate resulting in an exponential growth of photocurrent. A larger overvoltage leads to a faster growth of the exponential current. The growth is limited by the diode's internal resistance R_{D} resulting in a discharge governed by a time constant of $\tau = R_{\text{D}}C_{\text{D}} = \mathcal{O}(1\,\text{ns})$ where C_{D} denotes the pre-avalanche capacitance of the diode. The voltage drops and hence the electric field decreases in the high field region yielding a slower growth rate of electron-hole pairs. The process evolves until the voltage drops to the breakdown voltage where a steady state of ionisation rate and extraction rate is reached. An external resistor R_{Q} in series of up to $10\,\text{M}\Omega$ is used to decrease the voltage below the breakdown voltage and hence quench the avalanche. This method is used most often and is called passive quenching, whereas active quenching uses active electronics instead. The diode is recharged with a time constant of $\tau = R_{\text{Q}}C_{\text{D}} = \mathcal{O}(100\,\text{ns})$ and is restored again to detect photons. The gain G is given by [56]:

$$G = \frac{Q}{e} = \frac{C_{\text{D}} \cdot \Delta U}{e} \simeq 10^6 \tag{1.13}$$

The large gain enables the detection of single photons with Single Photon Avalanche Photodiodes (SPADs). The signal no longer is a current linear to the number of impinging photons but rather a current pulse independent of the number of photons. The binary signal of whether one or multiple photons were detected or not is transformed to an analogue current signal. Since the signal has always the same amplitude a SPAD lacks the ability to distinguish how many photons are detected [49].

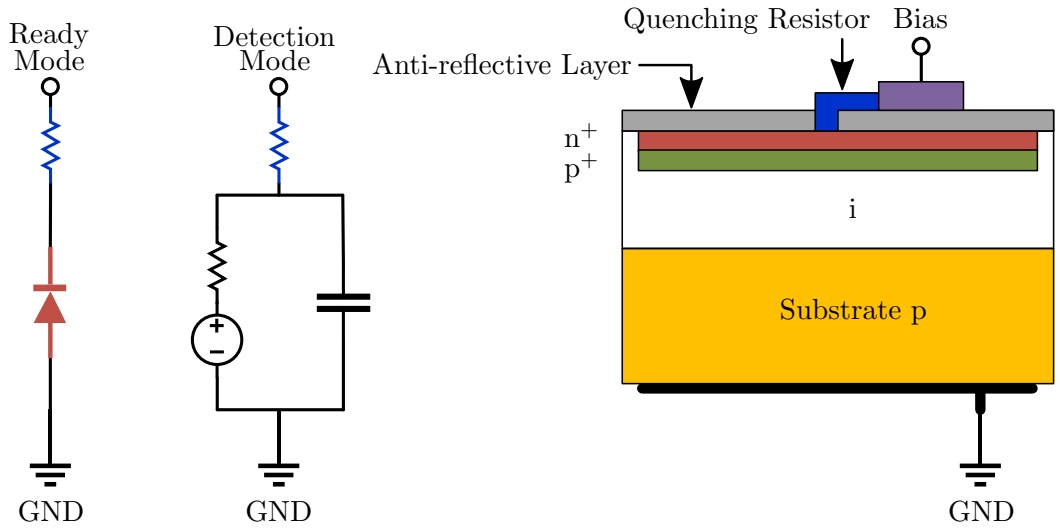

Figure 1.10: Topology of a SPAD (right) with the associated electric circuit (left). The bias voltage is applied via a quenching resistor. Absorption of photons dominantly takes place in the intrinsic layer. The photoelectron is drifted in a relatively low electric field to the junction with p^+ and n^+ doped silicon where the avalanche is triggered by a large electric field. The anti-reflective coating reduces reflection of photons due to mismatching refractive indices of silicon and air. The electric circuit is shown for the mode without and during an avalanche. Adapted from [50, 57].

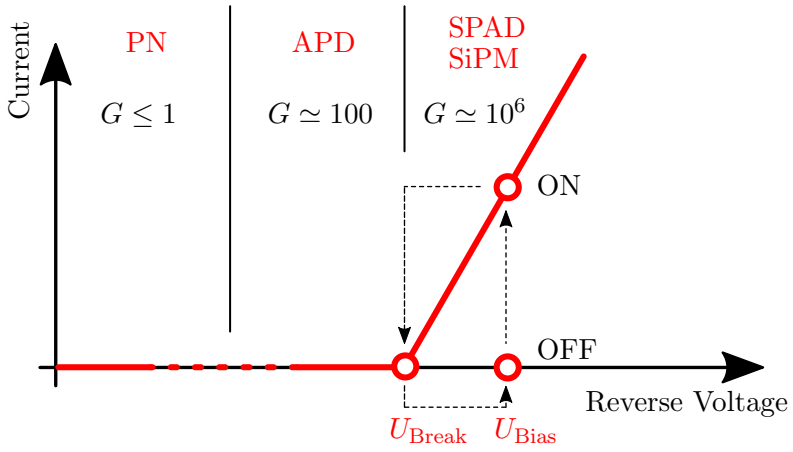

Figure 1.11: Schematic current-voltage and gain-voltage dependencies and integration of the different photodiodes into these dependencies. The mechanisms of a SPAD are shown qualitatively. Adapted from [50, 57].

A Silicon Photomultiplier typically consists of 100 - 90 000 single SPADs that are connected in parallel on an overall area of $1 \times 1\,\mathrm{mm}^2$ to $10 \times 10\,\mathrm{mm}^2$. Each SPAD in a SiPM is hereafter called pixel and has a pixel pitch in the order of 10 - 100 µm.

The complete doping profile is p^+-i-p-n^+, as shown in figure 1.12 together with the equivalent circuit of a SiPM. Depending on the intended application, the doping profile can be inverted to maximise the sensitivity on a given wavelength. To reduce optical optical crosstalk (CT) the pixels can be separated by optically opaque trenches. The bias voltage is applied via the quenching resistor which is most often made of polysilicon. Both resistors and electrical circuits for bias reduce the sensitive area of a SiPM to photons. The fraction of the sensitive area is called geometric efficiency or fill factor and is an important parameter of SiPMs.

Although each pixel operates as a binary detector, a SiPM is an analogue device. A signal corresponds to the sum of the signals of all triggered pixels. Since every pixel has a standardised signal photon counting is possible. However, if two photons impinge on the same pixel at the same time, the signal will appear the same as if only one photons had hit the pixel. Furthermore, the number of detected photons cannot exceed the number of pixels. Both effects become an issue when working with high intensities where saturation effects can contribute to the signal. The dependency of the number of fired pixel N_{fired} on the number of impinging photons N_γ is commonly described by [49]:

$$N_{\mathrm{fired}} = N_{\mathrm{tot}} \cdot \left(1 - \exp\left(-\frac{N_\gamma \cdot PDE}{N_{\mathrm{tot}}}\right)\right) , \tag{1.14}$$

where N_{tot} denotes the number of pixels on a SiPM and PDE its photon detection efficiency (see section 5.1). The non-linear performance of a SiPM is shown graphically in figure 1.13.

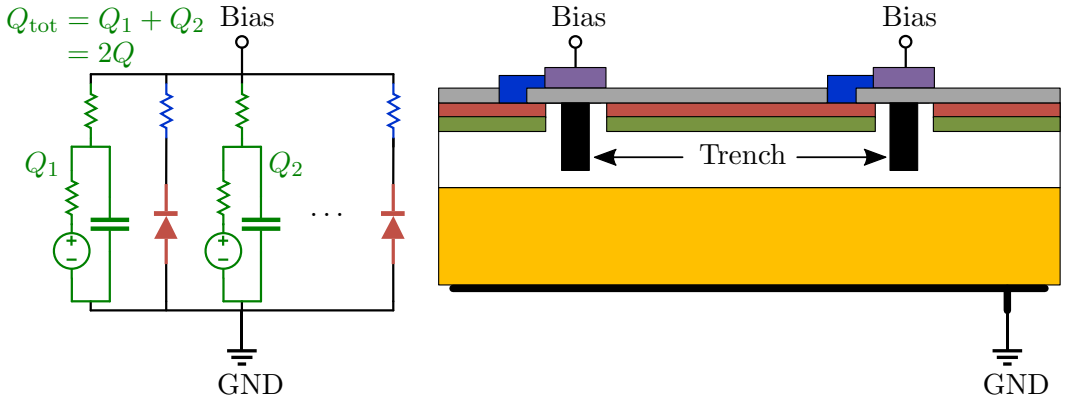

Figure 1.12: Topology of a SiPM (right) with the associated electric circuit (left). The structure of a single pixel corresponds to the structure of a SPAD as was shown in figure 1.10. The pixels in a SiPM can be separated by trenches to reduce optical CT. The electric circuit for one pixel corresponds to the one of a SPAD as well. Shown is a exemplary circuit where two pixels fire and thus release a charge Q_1 and Q_2, respectively. The resulting total charge that is measured corresponds to the sum of both charges. Adapted from [50, 57].

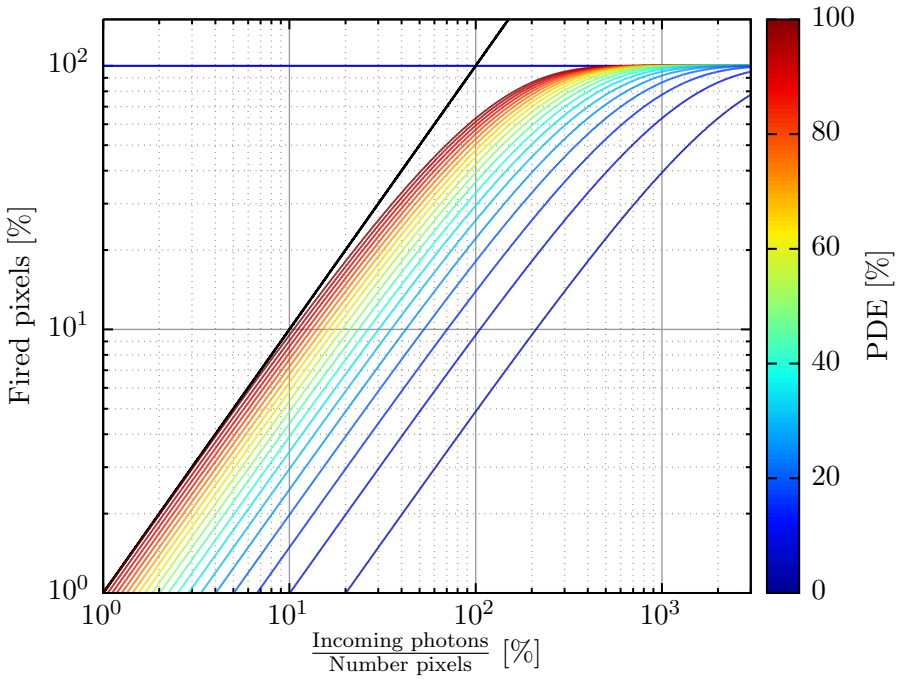

Figure 1.13: The dependency of the percentage of fired pixels on the fraction of incoming photons and number of pixels. 100 % of fired pixels is shown in blue and the bisection in black. The non-linear dependency is shown for multiple values of PDE denoted by the colour.

1.3.2 Comparison of presented Technologies

The technologies presented in the previous section as well as the technology of Photomultiplier Tubes (PMTs) (for a short introduction see section 2.2.1) show different advantages and are suited for different applications. A comparison is given in table 1.3.

1.3.3 Requirements for the nEXO Experiment

The low background feature of the nEXO experiment as well as the necessity to estimate the scintillation light of an event with an adequate accuracy pose several requirements on the applied light detector system that will cover an overall area of about $4\,\mathrm{m}^2$.

Since silicon can be produced with high radiopureness, this gives reason to expect a high radiopurity of about $10\,\mu\mathrm{Bq\,kg}^{-1}$. The design of the whole detector demands a sub-dominant contribution from SiPMs to the background budget. These motives forbid PMTs as light detectors in nEXO. The wire bonds used with the SiPMs holdings are not expected to be problematic because of their low mass. The carrier boards, however, could cause problems in terms of radiopurity. Approaches using quartz or sapphire boards are under inverstigation to overcome these issues. Problems may also arise from out-gassing which limits the LXe purity and thus the electron lifetime necessary for the charge drift in the TPC. Another aspect to consider is the number of feedthroughs that can increase radioactive background. Therefore, the SiPMs will be arranged in arrays of $\geq 10\,\mathrm{cm}^2$ to reduce the number of feedthroughs required.

Table 1.3: Comparison of different technologies to detect light. Entries marked with an asterisk (*) are due to the sensitivity of the external electronics to magnetic fields and not of the detectors themselves. Taken from [49, 58, 59].

	PIN	APD	SiPM	PMT
Minimum Flux	200	10	1	1
Gain	1	10^2	10^6	10^6
Bias	Low	High	Low	High
Temperature Sensitivity	Low	High	High	Low
Readout	Complex	Complex	Simple	Simple
Design	Compact	Compact	Compact	Bulky
Large area?	No	No	Yes	Yes
Sensitivity to magnetic Fields?	Yes*	Yes*	No	Yes
Noise	Low	Medium	High	Low
Rise time	Medium	Slow	Fast	Fast

Table 1.4: Summary of the requirements on SiPMs suitable for the nEXO experiment. Some of the given parameters are discussed in more detail in the text. The entry with one asterisk (*) indicates the SiPMs' contribution to the overall background. Taken from [63].

Parameter	Value
Photon Detection Efficiency	$\geq 15\,\%$
Radiopurity*	$< 1\,\%$
Dark Count Rate	$\geq 50\,\mathrm{Hz\,mm^{-2}}$
Correlated Avalanche Probability	$\leq 20\,\%$
Active Area per Module	$\geq 1\,\mathrm{cm^2}$
Capacitance	$< 50\,\mathrm{pF\,mm^{-2}}$
Gain Fluctuations + Electronics Noise	< 0.1 p.e.
Single Photon Timing Resolution (σ)	$< 1\,\mathrm{ns}$

Arrays of up to $20 \times 20\,\mathrm{cm^2}$ are subject of investigation but since the noise increases with the capacitance the possible area of an array is limited. In order to achieve adequate arrays, the capacitance should not exceed $50\,\mathrm{pF\,mm^{-2}}$ [60].

Besides the requirements posed on the deployed materials, there are criteria for the detector performance itself. An important one is the stated aim to detect 10 % of the scintillation light of an event to be able to estimate the entire amount of scintillation light adequately. This leads to a minimum PDE of the SiPMs of 15 % at a wavelength of 178 nm. Due to the large mismatch of the refraction indeces of silicon ($n \sim 0.8 + 1.9i$ [61]) and xenon ($n = 1.7$ [62]), about 50 % of the photons are reflected. These photons can be detected by other SiPMs in the vessel. The dark count rate (DCR) is not supposed to exceed a rate of about $50\,\mathrm{Hz\,mm^{-2}}$ at LXe temperatures in order to not affect the measurements in a negative manner. The probability of a correlated avalanche per primary avalanche resulting from CT or from afterpulsing (AP) should not exceed 20 %. Otherwise the energy resolution would suffer from this feature. Furthermore, a good time resolution of about 1 ns is targeted which would be useful for better pulse shape discrimination, but this parameter is not as crucial as other requirements for the detectors.

Although the EXO-200 experiment uses APDs to detect the scintillation light the nEXO experiment will use SiPMs instead. nEXO will benefit from the SiPMs' properties such as larger gain and higher signal-to-noise ratio in comparison with APDs while having lower mass. This fundamental change of the light detection system shows multiple advantages with regard to the requirements of nEXO and will increase the energy resolution significantly. All requirements imposed on the SiPMs are taken from [63] and are summed up in table 1.4.

Chapter 2

Experimental Setup and Data Acquisition

Contents

This chapter addresses the components used for measurements in this thesis. The complete setup is introduced and the relevance of its parts is discussed. The functionality of the reference detector is shortly discussed. The SiPMs used within this thesis are presented including their specific attributes. The functionality of the preamplification board which amplifies the small SiPM's signals is discussed.

2.1 Components

The measurements presented in this thesis were taken in a vacuum chamber at cryogenic temperatures surrounded by an insulation vacuum chamber. The latter one is important to achieve a stable low temperature. A picture of the complete setup is shown in figure 2.1. The setup consists of two separate chambers. These are the outer chamber, hereafter called insulation vacuum, and the inner chamber containing the physics setup, hereafter called xenon cell. All important components of the setup are labelled in the figure:

- Insulation Vacuum
- Xenon Cell
- Vacuum System
- Gas Inlet System
- Temperature Control
- Data Acquisition

The items listed above are discussed within this chapter in appropriate detail. A CAD-drawing containing most of the components is shown in figure 2.2.

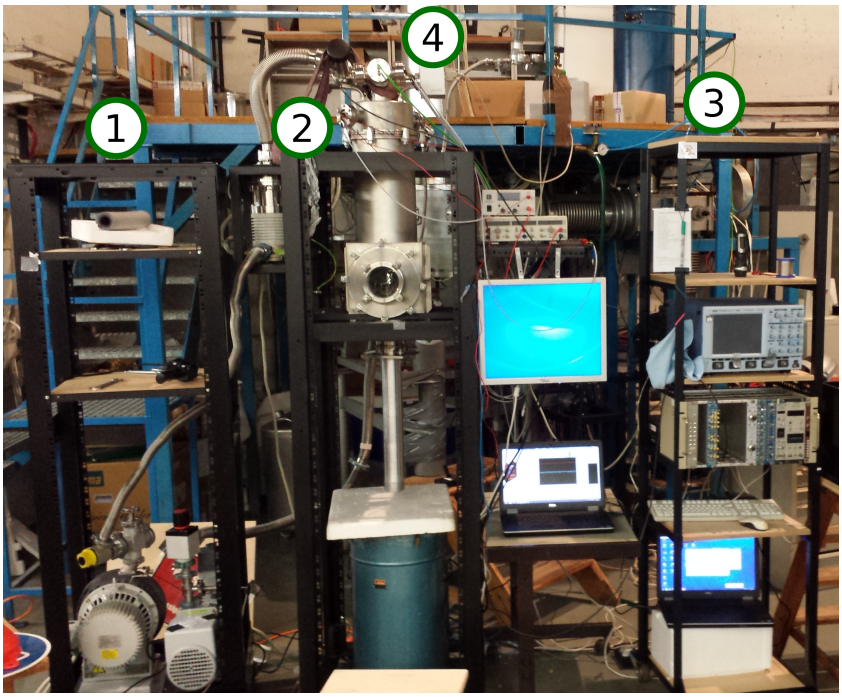

Figure 2.1: Picture of the complete setup. It consists of a rack holding the pumps (1) and a rack holding the insulation vacuum (2) in which the xenon cell is placed. Another rack contains the electronics equipment (3). The gas inlet system (4) is located behind the insulation vacuum (2). More information on the components is given in the corresponding paragraphs.

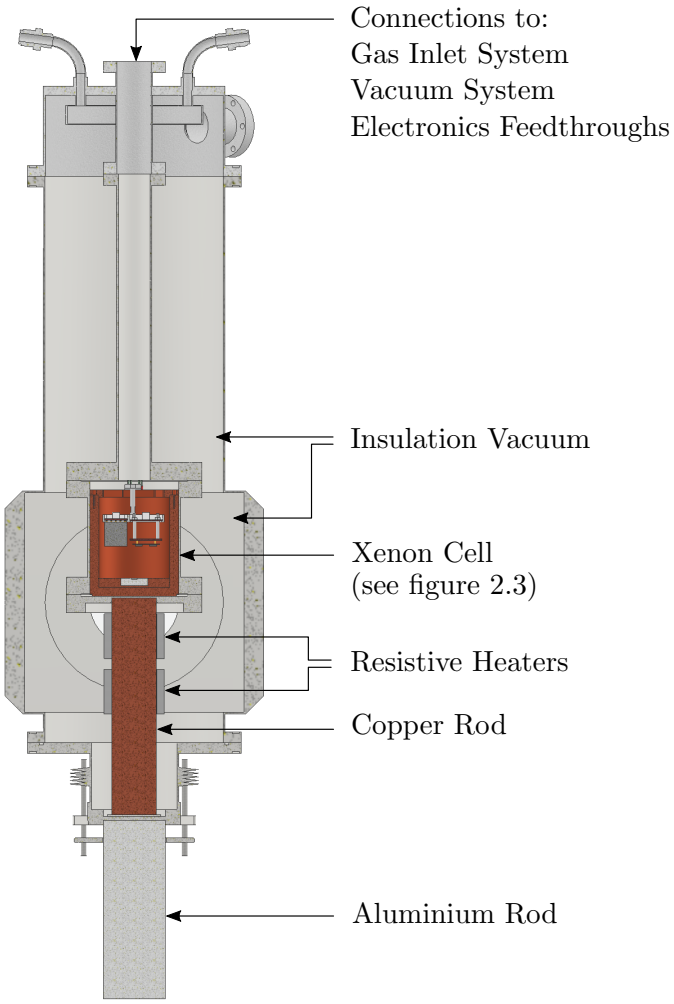

Figure 2.2: CAD of the entire setup. The most important components are marked. More details on selected components are given in the text.

Xenon Cell The physical setup is placed in the xenon cell. It contains a massive cup of copper to enhance vertical thermal balance inside of the xenon cell. Its design is shown in figure 2.3. The temperature inside the xenon cell is monitored via three sensors on the outside wall of the copper cup and one sensor on the printed circuit board (PCB) holding the SiPM. Within the copper cup at the bottom there is a radioactive α-source consisting of ^{239}Pu (5.15 MeV, 41 %), ^{241}Am (5.48 MeV, 47 %) and ^{244}Cm (5.80 MeV, 12 %). The source has a diameter of 5 mm and is embedded into an aluminium holder. The α-particles have a mean range of 2.2 cm in GXe at 1 atm [64]. Along its trajectory the α-particle emits in total about 130 000 scintillation photons[1] with a wavelength of 175 nm. Both the reference detector and the SiPM are mounted on a Polytetrafluoroethylene (PTFE) structure facing the bottom of the copper cup to detect the scintillation photons. Details on the actual detectors are given in section 2.2. Teflon is used because of its non-conducting properties, its excellent outgassing properties as well as its chemical inertness in xenon environments. The Teflon structure is connected to the top of the copper cup via spacers so that the height of the Teflon structure above the α-source can be modified by using spacers of different length.

Coaxial cables with PTFE-insulation connect the detectors to the electrical feedthroughs on the top of the vessel. Detector biases and signals are sent to periphery through MHV-feedthroughs and BNC-feedthroughs, respectively. Cables for temperature sensors and for operational amplifiers are connected via multipin-feedthroughs.

Since the reflection coefficients of copper and aluminium are unknown, the whole xenon cell is simulated within the research group with a GEANT4 based simulation to examine the influence of the geometry on measurements. This simulation has shown that the unknown reflection coefficients and the asymmetric setup can be accounted for with correction factors coming from the simulation.

[1] The total number cannot be given exactly since W_{ph} differs within literature [65, 66]. By using a reference detector this issue can be overcome.

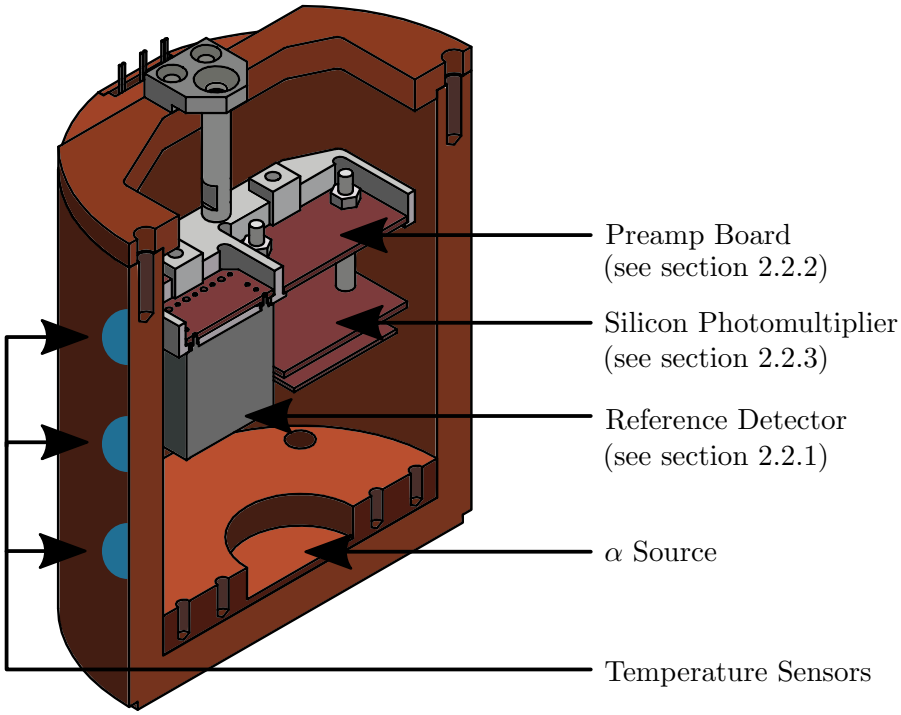

Figure 2.3: The copper cup contains the physical components. The reference detector, the SiPM with corresponding preamplification board and the α-source are indicated by arrows. More details on the components are given in the text and in the corresponding sections referred to in the description. The positions of the temperature sensors are marked in blue.

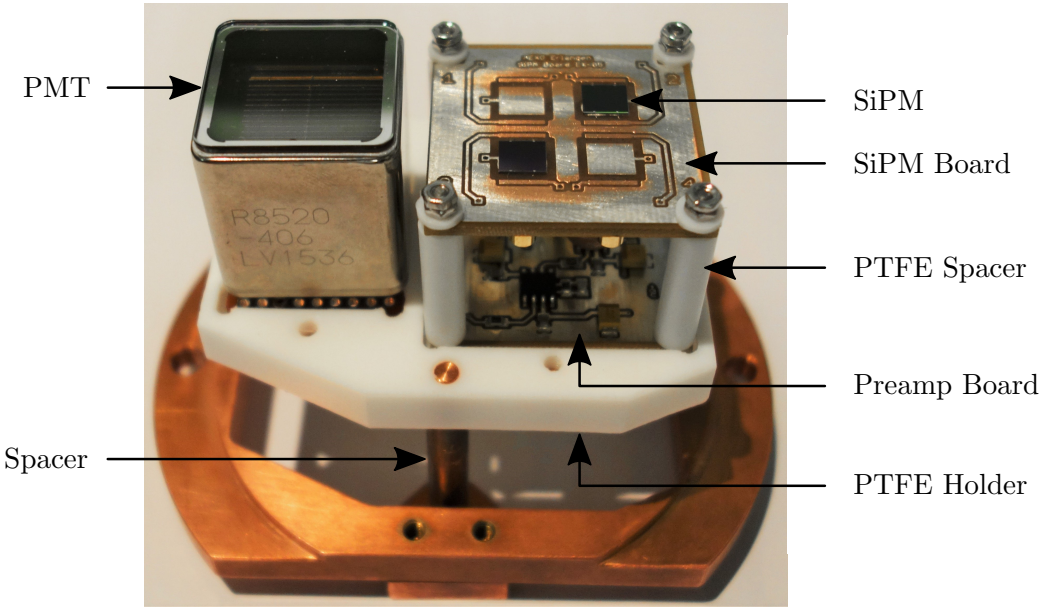

Figure 2.4: Teflon structure holding the reference detector (PMT) on the left and the assembly of SiPM board and preamplification board on the right. The height of the complete structure can be altered by spacers and the relative height of reference detector and SiPM is adjustable with PTFE spacers in the SiPM assembly. A temperature sensor is placed on the PCB holding the SiPM in order to monitor its temperature precisely.

The Insulation Vacuum To avoid corrosion of the xenon cell and to simplify the temperature control in the xenon cell it is surrounded by an outer chamber. The latter is evacuated with a *RV5* vacuum pump from Edwards to about $7 \cdot 10^{-3}$ mbar to avoid heat exchange through thermal conduction and convection. Thermal radiation is suppressed via super insulation foils. A CAD-drawing of the complete vacuum chamber is shown in figure 2.2.

Vacuum System and Gas Inlet System The xenon cell is to be filled with GXe or LXe. Therefore, it is first evacuated by a *GVSP30* scroll pump from Edwards and a turbo pump *TPU 180H* from Pfeiffer Balzers to a pressure of about $5 \cdot 10^{-5}$ mbar to reduce a large extent of water as well as other impurities from the xenon cell. Both pumps work oil-free. As soon as the setup is cooled down, the vacuum system is sealed and the xenon cell is filled with GXe through the gas inlet system. Afterwards the gas inlet system is sealed as well. The GXe is released into air after a completed physics run.

Temperature Control The xenon cell is cooled indirectly with liquid nitrogen (LN). An aluminium rod is immersed into a LN reservoir. A copper rod in the insulation vacuum connects the xenon cell thermally with the aluminium rod. The thermal conductivity between these components is improved by indium. Using this cooling system the temperature drops to $-100\,°C$ in about 4 h. To keep the temperature stable the copper rod can be heated via several resistors with a maximum heating power of 80 W. Four temperature sensors monitor the temperatures

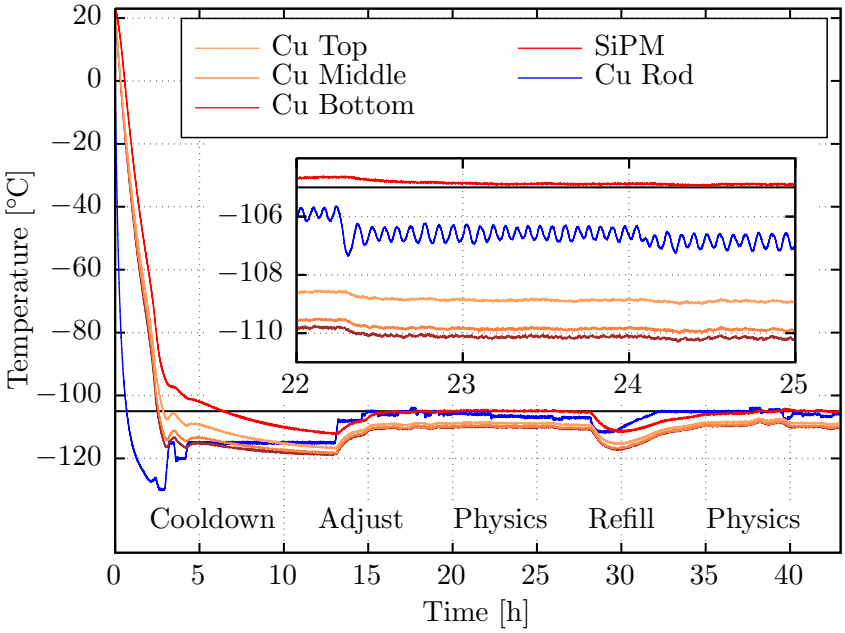

Figure 2.5: Temperature course at several sites in the setup. Different actions are denoted in the figure. The inset shows a zoom to the temperature course during a physics run. There the temperature at the SiPM board fluctuates by about 0.05 °C.

throughout the xenon cell. Another sensor is mounted on the copper rod. The position of the sensors is shown in figure 2.3. The temperature is automatically regulated by triggering on one of the temperature sensors, most often on the one on the aluminium rod. The temperature fluctuates by about 0.05 °C at the SiPM board during physics runs.

Data Acquisition Signals from the reference detector and from the SiPM are sent via shielded cables and floating-shield BNC-feedthroughs to the periphery. There, the signals are displayed and saved with either an oscilloscope of the type *WAVERUNNER® 6100A* from LeCroy [67] or with a digitizer *DRS4* from PSI [68]. The oscilloscope was used in the majority of the measurements conducted. The settings used are shown in table 2.1

Table 2.1: Oscilloscope settings used for the measurements conducted.

Parameter	w/o α-source		w/ α-source	
	SiPM	PMT	SiPM	PMT
time window [µs]	10	0.5	2 / 5	2 / 5
time sampling [GS/s]	2.5	2.5	2.5	2.5
voltage window [mV]	40	80	80 / 160 / 400	1600 / 4000
voltage resolution [mV]	0.16	0.32	0.32 / 0.64 / 1.6	6.25 / 15.7
bandwidth limit [MHz]	200	200	200	200

2.2 Detectors

2.2.1 Reference Detector

The reference detector is a PMT. These kind of detectors show low noise and high gain while at the same time having the ability to detect single photons. Their functionality has been established for decades. These advantages promote the use of a PMT as reference detector.

A standard PMT is constructed with an evacuated tube containing a photocathode, a system of several dynodes and an anode. Incoming photons can extract electrons via the intrinsic photoelectric effect on the photocathode plane. The probability to trigger an electron is called QE. A triggered electron is accelerated to the first dynode where the electron induces secondary emission resulting in a multiplication of the incoming electron signal. The probability to collect the triggered electron at the first dynode is called collection efficiency (CE) whereas the probability to multiply this electron is given by P_{mult}. The emitted electrons are accelerated to another dynode and are multiplied again. A PMT contains several dynode stages resulting in a multiplication of the primary triggered electron of:

$$G = p^n \approx 10^5 \; - \; 10^6 \tag{2.1}$$

p describes the multiplication factor at each of the n stages. To accelerate the electrons between the dynodes a voltage divider is used. The amplified signal can be detected at the anode and enables to detect low fluxes down to single photons.

The detector used in this thesis is a PMT *R8520-406 SEL* from Hamamatsu [69] with an active area of $20.5 \times 20.5\,\text{mm}^2$. These device is specifically designed to be used at low temperatures and for UV-light. It is shown in figure 2.4. The 10 dynode stages are arranged as a scheme called *metal channels*. The PMT has a QE of 32.1 % at a wavelength of 175 nm of the incoming photon. The product of $(\text{CE} \cdot P_{\text{mult}})$ is specified to be approximately 70 %. Given these parameters, the PMT has a detection efficiency (DE) of:

$$\text{DE} = \text{QE} \cdot \text{CE} \cdot P_{\text{mult}} \simeq 22.5\,\% \tag{2.2}$$

The PMT is operated at 800 V where it has a typical gain of 10^6. The manufacturer indicates a signal delay of (12.4 ± 0.8) ns.

2.2.2 Preamplification Board

To amplify the small signals from a SiPM, a preamplification board denoted by EX-03 with an area of $35 \times 35\,\mathrm{mm}^2$ is used. The circuit layout and the physical design are created with EAGLE [70] and are shown in figure 2.6. The board is made of FR4 and is operated at cryogenic temperatures inside the xenon cell close to the SiPM. The close proximity to the SiPM board avoids additional noise that would be caused by long cables. All connections are realised with MMCX connectors from SAMTEC [71] to shielded RF-178 coaxial cables. The cables which are directed to different feedthroughs are rubber-free and use FEP jackets. This feature is important since rubber disintegrates in xenon and thus contaminates the detection medium.

The bias voltage for the SiPM is provided by a power supply of the type *shq 122M* from iseg via the preamplification board. The resistance of $10\,\mathrm{k}\Omega$ on the input side protects the SiPM against large current. The capacitance on the input side provides a fast current source to catalyse the recharge of a fired pixel. In this case a current pulse had been sent to the preamplification board where its DC component is cut off with a capacity in series. Afterwards high AC frequencies are suppressed by a capacity in parallel. The remaining signal is amplified by a two stage transimpedance amplification scheme. This scheme is a current-to-voltage converter realised with two operational amplifiers ADA4895-1 each of which is operated at $5\,\mathrm{V}$ and $-5\,\mathrm{V}$ from a power supply *E3631A* from Hewlett Packard. Electrolytic capacitors are used to ensure a fast responding current source after signals. Both operational amplifiers have a load resistance of $R_{\mathrm{load}} = 100\,\Omega$ and a feedback resistance of $R_{\mathrm{back}} = 1\,\mathrm{k}\Omega$. The feedback capacitor improves the stability of the amplification. Thus the electric scheme results in a amplification of :

$$G_{\mathrm{ampl}} = \frac{R_{\mathrm{back}}}{R_{\mathrm{load}}} \cdot \frac{R_{\mathrm{back}}}{R_{\mathrm{load}}} \simeq 100 \tag{2.3}$$

Finally the impedance of the amplified signal is matched to $50\,\Omega$ and put out from the preamplification board.

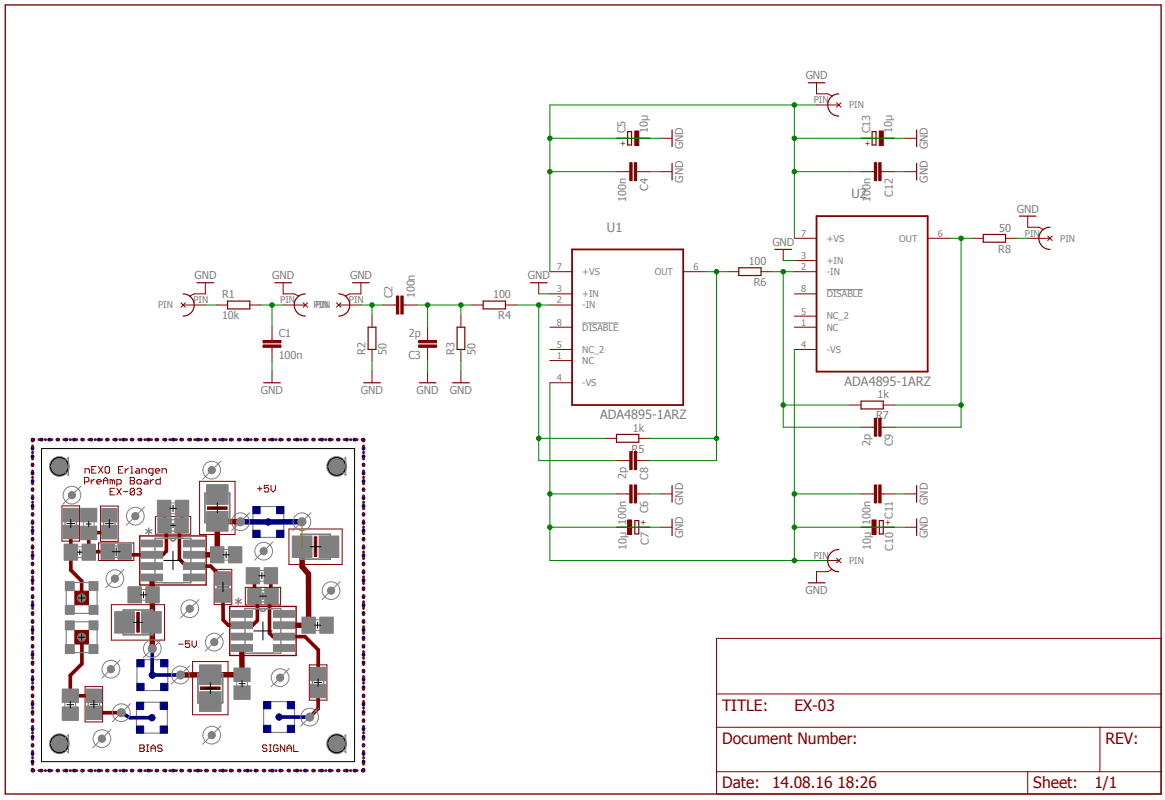

Figure 2.6: Circuit diagram of the preamplification board which is used to amplify the signals from the SiPM. Traces and conjunctions are shown in green and electronic components in red. The functionality of the circuit is explained in the text. The inset shows the physical design of the preamplification board. Traces on the top layer are shown in red and traces on the bottom layer in blue respectively. The solder joints of the electronic components are shown in grey as well as the vias connecting the top and bottom layer. The latter is on GND potential. In the corners there are drilling holes to mount the board in the xenon cell.

2.2.3 Silicon Photomultipliers

The SiPMs from FBK [72] characterised in this thesis are of the types *VUV-HD 2016 STD* and *VUV-HD 2016 LF* provided by collaborators from Stanford (USA) within the nEXO collaboration. The latter devices are better suited for operation at cryogenic temperatures since the STD devices exhibit large leakage currents at that temperatures. Every detector contains an array of 2×2 SiPMs with an area of nearly $3 \times 3\,\mathrm{mm}^2$ each, resulting in a detector size of $5.56 \times 5.96\,\mathrm{mm}^2$. The pixel pitch is $25\,\mu\mathrm{m}$ and the SiPMs have a geometric fill factor of 73 %. A VUV-HD 2016 LF SiPM is shown in figure 2.7. The SiPMs are attached via conductive glue to a PCB denoted by EX-05 where the signal is modulated on the GND potential and is transmitted to the preamplification board. A negative bias voltage is applied to each unit of the SiPM by wire bonds that are connected to pads on the PCB carrying the same bias[2]. The bias voltage is provided by a cable from the preamplification board. For redundancy reasons all units are bonded with two wires. The wires are bonded in an ultrasonic wedge/wedge bonding process.

[2]Thanks to Gerhard Tischlinger from Fraunhofer ICS for glueing and wire bonding the detectors.

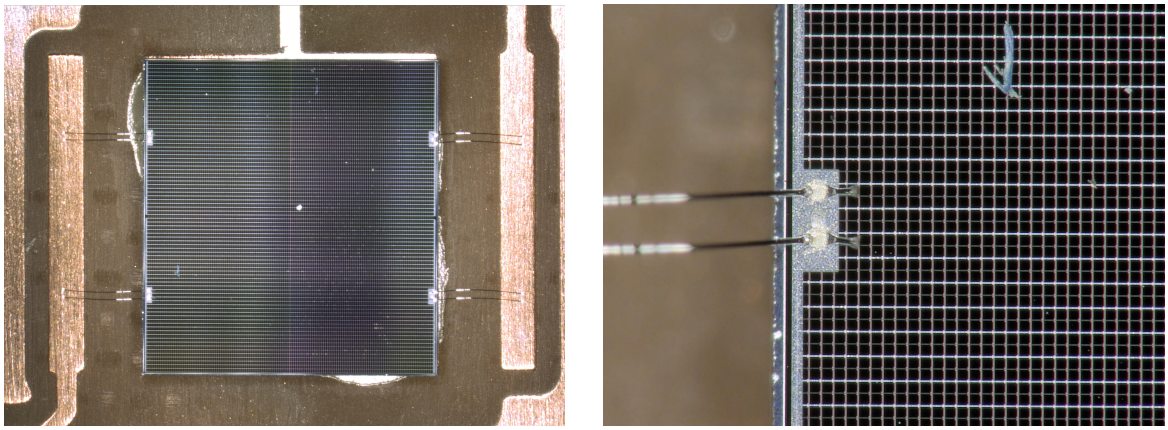

(a) **(b)**

Figure 2.7: (a) Microscopic image showing a SiPM of the type *VUV-HD 2016 LF* with a size of about $6 \times 6\,\mathrm{mm}^2$. It is glued conductively to the PCB where the output of the detector is located. The bias voltage is applied to each unit by wire bonds leaving all from pads with the same bias. **(b)** shows a zoom on a part of the lower left unit of the SiPM. The pad has a size of 120 - 280 µm. The bias voltage is applied to each pixel (black) via the silver conductor. The blue structure is an external contamination on top of the detector. More information on the detectors and the manufacturing of these is given in the text.

Chapter 3

Data Processing and Analysis

Contents

In order to perform analyses of measurements, a program was implemented based on C++ and ROOT. The analysis software consists of four mostly independent modules. The first one is data processing where measurements are read in and are stored in a way to re-use them for multiple analyses. The focus here is to provide data with an uniform structure for the upcoming analysis independent of the device used to conduct the measurement. Another focus is to optimize the speed of an analysis by storing the data binary in a ROOT TTree.

The second module contains the analysis of the single waveforms. There are three algorithms available to perform the pulse analysis as well as several auxiliary methods. The resulting parameters of the pulses within the waveforms are stored in another ROOT TTree for further analysis.

The parameters of the pulses are processed within the next module. Herein, histograms and scatter plots, among others, are produced to extract physical parameters of the SiPM. Quantities like the gain or the optical crosstalk probability are deduced within this module. This module is reviewed shortly in this chapter and is discussed in more detail in the next chapter.

The final module calculates quantities combining results from analyses of several measurements like, for example, the breakdown voltage. As this module dominantly contains methods resulting in physical parameters it is not discussed in this chapter but its results will be presented in the next chapter. The flow diagram of the complete analysis software is shown in figure 3.1.

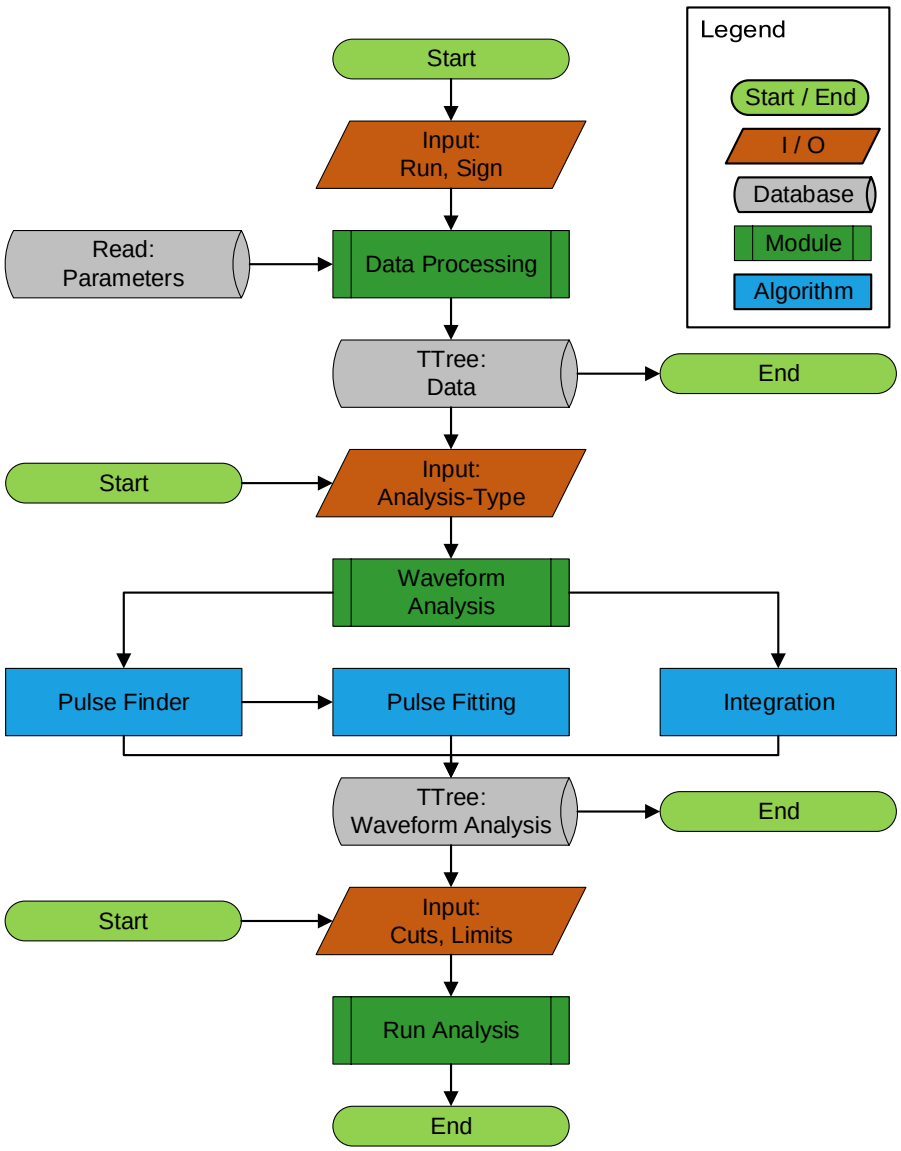

Figure 3.1: Flow diagram of the complete analysis software. It is designed to consist of several mostly independent modules. This feature makes it possible to continue an analysis at a later stage. Nevertheless it is possible to conduct a complete analysis in one run.

3.1 Data Processing

The first step of the analysis is to process the data. All waveforms and additional information about the measurement are stored in a TTree for further analysis. To perform the reading, the path of the folder containing the data or the path of a file containing a list of folders with data has to be handed over to the program. The second choice was implemented to perform combined analyses of different measurements in order to be able to examine the dependencies on the overvoltage, for example. Furthermore, the program can read measurements from either the oscilloscope or the digitizer, so this information has to be given as well. Another input is the signal polarity of the pulses. This information is necessary since the later algorithms are designed to analyse positive pulses. If the pulses of the measurement are negative, the complete waveform is inverted to make them positive. A set of original waveforms is shown in figure 3.2.

The next step is to load additional information about the measurement from a central file, containing information like bias voltage, temperature or pressure during the measurement. This information is saved in a TTree and can be reused afterwards if necessary.

Regardless of the apparatus used to collect data, all files of a certain run are processed. After opening a single file, the number of waveforms within that file and their particular lengths, meaning the number of values forming the waveform, are processed. The next step is to read in the timestamp of each trigger relative to the first trigger in a particular file. The accuracy of this information is 1 ns while the temporal accuracy between separate files is only 1 s. Thus, calculating time differences of triggers between different files is not possible. Afterwards, the time and voltage values of each waveform are read from the file and are inverted depending on the polarity. Having fed this data into the program, the waveform, the difference between the timestamp of the trigger and the one of the previous waveform as well as the length of the waveform are stored in a TTree which is again saved onto disk.

Although data is stored twice using this procedure, its big advantage is that data is stored uniformly, not depending on the apparatus used to collect the data. More importantly, this module is only needed once when reading the data for the first time. This approach increases the speed of the complete analysis drastically when performing the analysis multiple times. The flow diagram of the initial data processing is shown in figure 3.3.

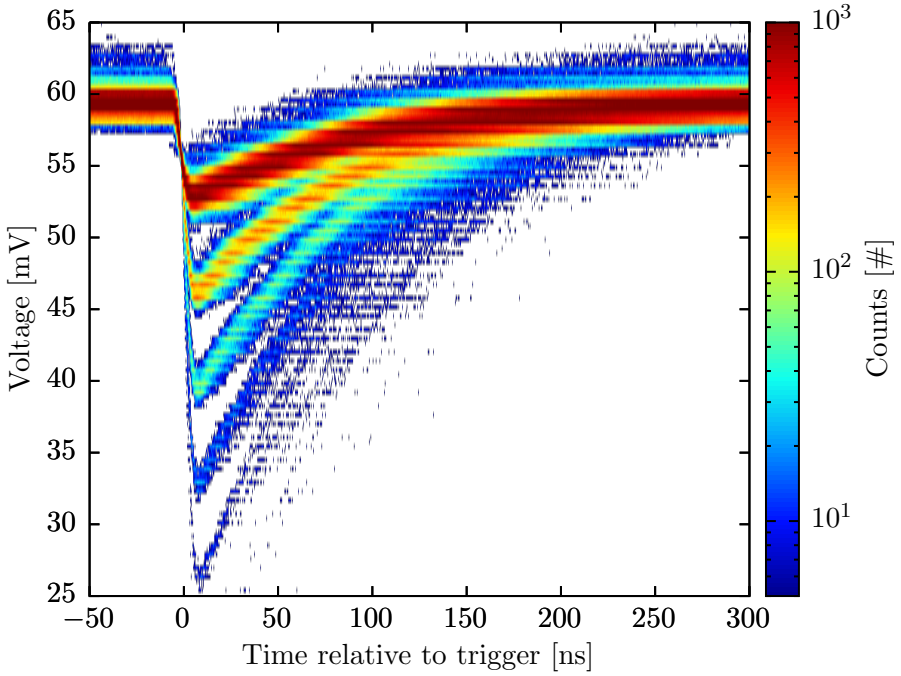

Figure 3.2: Illustration of triggered pulses in one set of data. The waveforms in this measurement have a length of 10 µs. The colour denotes the abundance of a single time-voltage pair. For clarity only waveforms containing only the triggered pulses are shown here. Waveforms containing multiple pulses were omitted. The discrete nature of the SiPM's response is visible, as the pulse heights are quantised. Each discrete pulse height corresponds to a certain number of photoelectron equivalents (p.e.s).

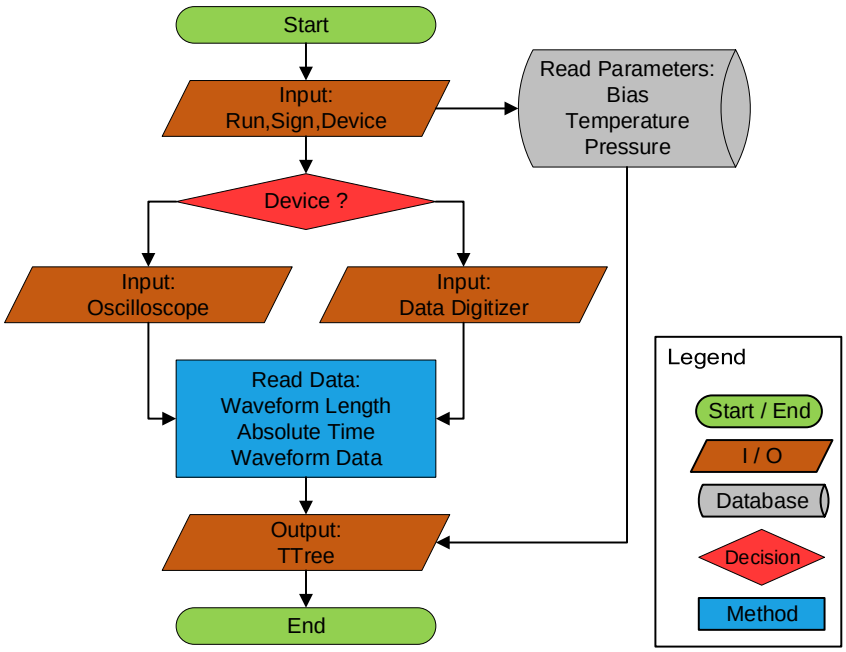

Figure 3.3: Flow diagram of the module containing the initial data processing. It is implemented to easily add new devices of data taking.

3.2 Waveform Analysis

This module comprises different techniques to analyse a given waveform. Each one is well-suited for different tasks. To analyse a waveform, it is loaded from the ROOT TTree together with its absolute trigger time. There is the possibility to choose one of three implemented smoothing algorithms. These are forward and symmetric boxcar smoothing as well as Gaussian smoothing. Further on, it is possible to restrict the complete analysis to a time interval. If this option is not used, the complete waveform is considered in the analysis. Figure 3.4 shows the flow chart of the waveform analysis. In the following subsections the individual algorithms of the waveform analysis are discussed.

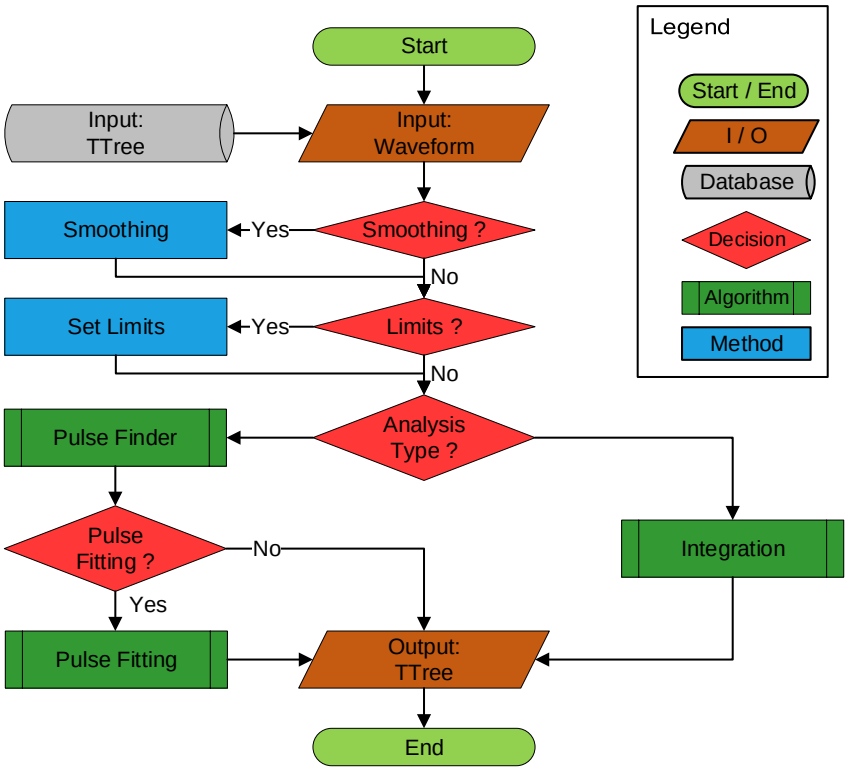

Figure 3.4: Flow diagram of the module containing the waveform analysis. Auxiliary methods like smoothing or a time-wise limited analysis are implemented. One can chose between three techniques to perform the waveform analysis which are discussed in the text in more detail.

3.2.1 Pulse Integration

The integral of a pulse is proportional to the charge released in that pulse. It will be shown in section 4.1.1 that thereby the gain can be calculated. Therefore, the integral is calculated numerically by an algorithm that sums all N_{int} voltage values $U(t)$ within a given time interval $[t_0 : t_1]$ multiplied by the inverse of the sampling rate S. This factor equals the time between consecutive voltage values. The baseline of the pulse is calculated by averaging the N_{base} voltage values from the begin of the waveform to the lower limit t_0 of the interval specified. This method is illustrated in figure 3.5. The equation for the integral is:

$$I = S^{-1} \cdot \sum_{t=t_0}^{t_1} \left(U(t) - \frac{1}{N_{\text{base}}} \cdot \sum_{t'=0}^{t_0} U\left(t'\right) \right) \tag{3.1}$$

$$= S^{-1} \cdot \left(\sum_{t=t_0}^{t_1} U(t) - \frac{N_{\text{int}}}{N_{\text{base}}} \cdot \sum_{t=0}^{t_0} U(t) \right) \tag{3.2}$$

The calculation is simplified with the second equation by not subtracting the baseline for each single voltage value individually but rather subtracting it N_{int} times after calculating the integral.

An advantage of this algorithm is its ability to consider multiple pulses that are in close proximity. On the other hand, the pulses are not recognised separately but rather the sum of all pulses. Thus, multiple pulses might get misinterpreted as one larger pulse. Furthermore, this method does not return a timestamp of the pulse. Therefore, this method is used dominantly for measurements with scintillation light where many photons trigger signals not simultaneously but within a short interval. For measurements at dark condition where the timing and the height of each pulse are of special interest the method is not used for the given reasons.

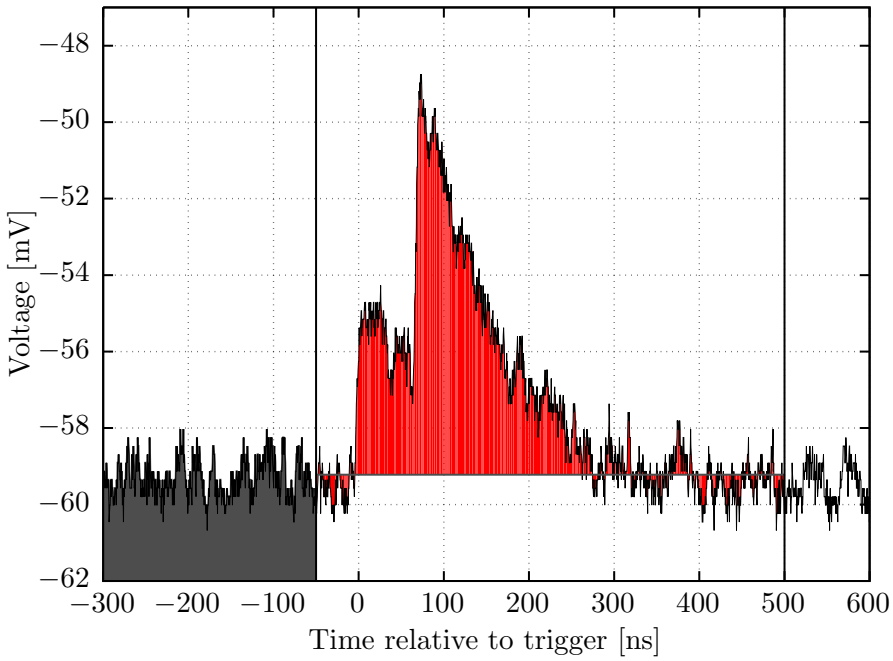

Figure 3.5: Waveform with two pulses. The deposited charge is calculated by summing the voltage values within the chosen limits and subtracting the mean baseline before that limit. The resulting charge is shown as the red area whereas the charge contributing to the calculation of the baseline is shown as the grey area. The limits of the charge calculation are indicated as vertical lines.

3.2.2 Pulse Height

Instead of the integral of a pulse, its height can be used to determine physical properties of a SiPM as well. The peaks in a waveform are found by a multi-stage algorithm. The first part is a peak finder provided by ROOT and afterwards the actual peak in the data is found. The peak finder uses the ROOT class TSpectrum to find peaks using customized settings. The performance of this peak finder is described in more detail in [73]. During the peak finding the waveform is smoothed to reduce the sensitivity to noise. Smoothing however, reduces the possibility to separate adjacent pulses, so a well balanced setting has to be found. After smoothing, peaks with a larger time lap of about 50 ns can still be separated whereas closer peaks are likely not to be resolved individually. In the next step, all pulses smaller than 2 mV above the baseline in the smoothed data are rejected. The remaining peaks are sorted chronologically. The process is shown in figure 3.6.

After having found a certain number of peaks in the smoothed waveform the next step is to find the related peak in the original data. This is necessary since the smoothing blurs the pulse. The actual peak is searched in a time window of 40 ns right before the smoothed peak. The time window is chosen to be asymmetric because of the smoothing. All time stamps whose voltage

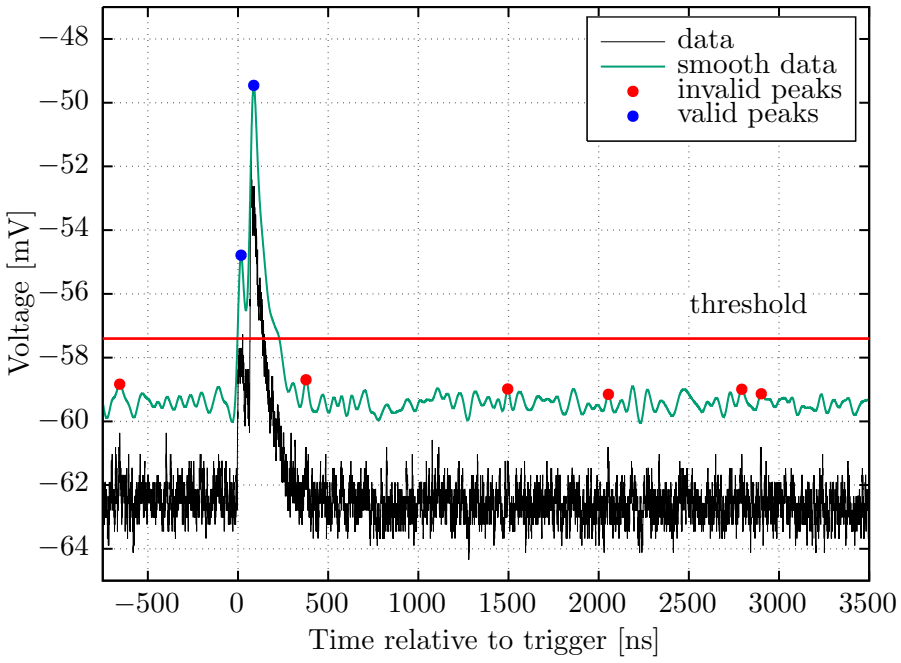

Figure 3.6: Original and smoothed waveform containing two pulses. For clarity reasons the original waveform is shifted vertically. The method from TSpectrum identifies several possible peaks within the smoothed waveform. Only those with an amplitude exceeding the threshold of 2 mV with respect to the baseline of the smooth waveform are considered valid peaks, whereas the other ones are discarded. The peak finder algorithm has correctly identified the two real peaks that are marked with blue circles.

values are larger than the adjacent ones up to a range of 2 ns are possible peak candidates. This criterion enables the algorithm to find local maxima. Noise fluctuations and noise peaks right after the real peak, that form a plateau, may be identified incorrectly as peaks since they may have larger values than the real peak. To exclude these peak candidates there is another parameter that is reviewed. It is the sum of the numerical differentiation of the voltage values within the previous 8 ns that is calculated for every peak candidate at t_0:

$$\sum_{t=(t_0-8)}^{t_0} U'(t) = \sum_{t=(t_0-8)}^{t_0} U(t+1) - U(t-1) \tag{3.3}$$

The denominator $2t$ in the numerical differentiation is omitted because it is a constant factor. Using the numerical differentiation, it is possible to consider the shape of a pulse. The voltage values right before the real peak have a rather large slope due to the rising edge of the pulse. Therefore, the peak is identified as the peak candidate by having the largest sum of slopes right before it.

The last step is to calculate the height of the found peak which is shown in figure 3.7 as an example. In order to do so, the baseline before the peak is calculated by averaging all N_{base} voltage values between 12 - 20 ns before the peak. The time interval is shifted from the peak by 12 ns in order to exclude the rising edge from the calculation. Finally, the pulse height A equals the difference between pulse value at the peak $U(t_0)$ and the baseline:

$$A(t_0) = U(t_0) - \frac{1}{N_{\text{base}}} \sum_{t=(t_0-20)}^{(t_0-12)} U(t) \tag{3.4}$$

This algorithm has the advantage that it is able to identify individual peaks in a waveform compared to the algorithm calculating the integral. This ability is necessary for advanced analyses as the determination of the recovery time of a pixel. Two features turn out to limit the accuracy. One is the method that is used to calculate the baseline. Pulses heights of pulses occurring on the falling edge of a preceding pulse are mis-calculated by subtracting the mean baseline before the peak since the falling edge of the preceding pulse results in a non-constant baseline underneath the subsequent pulse. To constrain the impact of this feature, the interval for calculating the baseline is kept quite small. A large interval would result in a larger distortion of the baseline since a larger fraction of the falling edge of the preceding pulse would be considered in the calculation of the baseline. Furthermore, the accuracy of separating multiple peaks with the peak finder algorithm is limited by the trade-off between smoothing and vulnerability to noise peaks. Given the selected parameters, adjacent peaks with a time difference of at least 50 ns can be separated reliably.

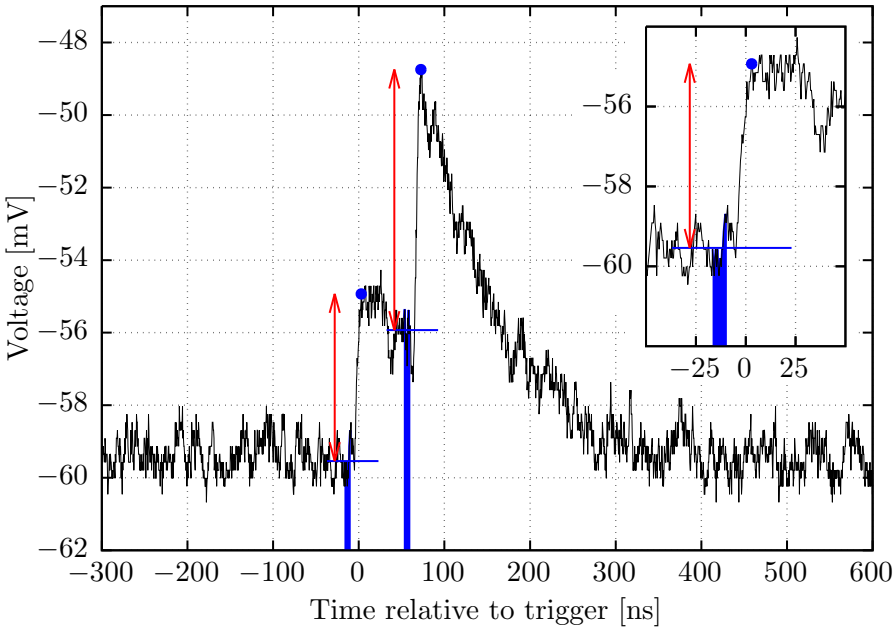

Figure 3.7: The same waveform as in figure 3.5 with both identified peaks. The peak height is calculated by averaging the baseline before the peak, which is shown in blue. The resulting pulse height is the difference between peak height and the baseline and is indicated by the red arrows. The algorithm is discussed in detail in the text.

3.2.3 Pulse Fitting

To overcome the issues of both former algorithms there is a third one that fits the pulses. This algorithm is based on the peak finder algorithm and performs a χ^2-fit on all found peaks[1]. The fit function is adapted from [74] and consists of a constant baseline B and a number of exponentially modified Gaussian distributions:

$$f\left(t, B, N, \sigma, \tau, \sum_i^N \mu_i, A_i\right) = B + \sum_i^N \frac{A_i}{2} \cdot \exp\left(\frac{1}{2}\left(\frac{\sigma}{\tau}\right)^2 - \frac{t-\mu}{\tau}\right) \cdot \operatorname{erfc}\left(\frac{1}{\sqrt{2}}\left(\frac{\sigma}{\tau} - \frac{t-\mu}{\sigma}\right)\right) \tag{3.5}$$

where N is the number of pulses fitted together and (μ_i, A_i) are the peak time and amplitude of the pulses, respectively. To enhance the stability of the fitting procedure, the rise time σ and the fall time τ are equal for all pulses fitted together. Furthermore, the maximum number of pulses fitted together is limited to $N = 4$. The initial parameters are the peak position and height from the peak finder algorithm and the baseline, that results from a fit with a constant function to the data between $[-750\,\text{ns} : -150\,\text{ns}]$ relative to the trigger. The fit is limited to a region of $[-20\,\text{ns} : 200\,\text{ns}]$ around the expected peak position. A priori every pulse is fitted separately. In the case the fit limits include the succeeding peak both pulses are fitted together. This process is iterated until the maximum number of pulses fitted together is reached or until the fit limit does not include a further peak. Afterwards, the peak positions in the fit are limited to a reasonable region, meaning within the total fit interval and between the adjacent peaks.

The entire fit procedure is executed twice. The first time, the baseline is fixed and the rise time and fall time are allowed to float within given intervals. The initial values of $\sigma = 2.0\,\text{ns}$ and $\tau = 80.0\,\text{ns}$ are used in a fit to each individual pulse. The previously shown waveform is now shown in figure 3.8 including the resulting fits. The most probable values for both parameters σ and τ are determined by fits of Gaussian functions to the resulting distributions of the whole data set. Both parameters are used for the second run of the fit procedure and are fixed to these values. Examples of the resulting distributions are shown in figure 3.9. By fixing both parameters, the shape of the pulses is fixed. In the second run of the procedure, the baseline is a free fit parameter as well as the peak position and height. All pulses in the complete set of data are fitted again. This two-parted procedure is chosen to enhance the fit stability as well as the accuracy of the second run.

Up to now, only those peaks are fitted, that have been found by the peak finder. As discussed already, there are deficiencies in finding multiple pulses that are close to each other. In order to work around that problem, there is an additional algorithm that uses the χ^2_{red} of the fit of the second run as an indicator of the accuracy of the fit. Every fitted pulse with a χ^2_{red} exceeding a fixed $\left(\chi^2_{\text{red}}\right)_{\text{min}} = 0.6$ is examined in this algorithm. The idea is to add pulses preliminary to the fit and only keep them permanently if the new χ^2_{red} improves by more than 2 % compared to the old one. Otherwise, the added pulse is rejected and the next initial pulse is examined. Pulses can only be added if the maximum number of pulses in the waveform and pulses that are fitted together is not exceeded. If this is not the case, the start parameters of the preliminarily added pulse are calculated by determining the position of the largest deviation

[1] This algorithm was partially adapted from collaboration partners at TRIUMF, VN, CA.

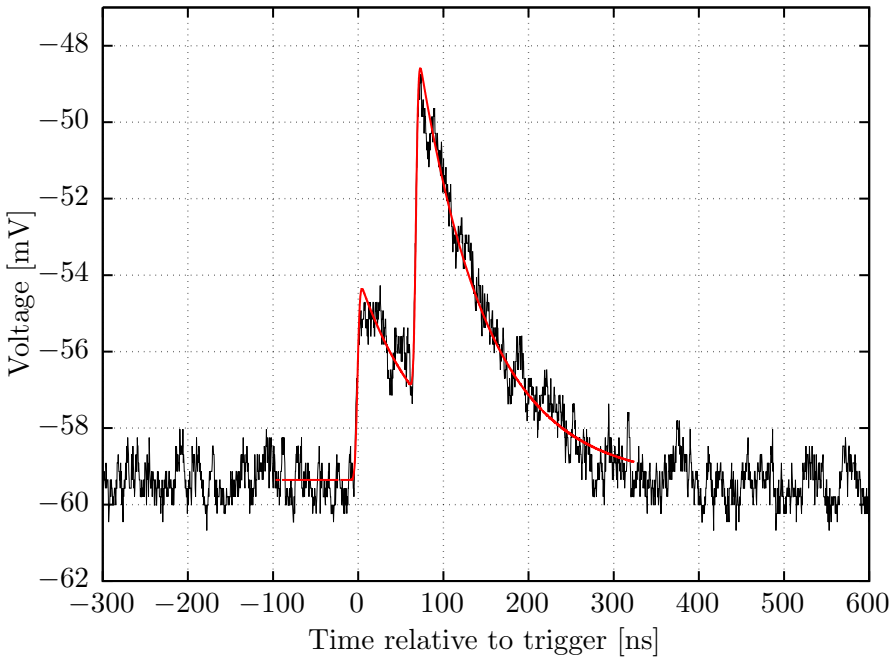

Figure 3.8: Both identified pulses within the waveform already shown in figure 3.5 and in figure 3.7 are fitted. The resulting pulses are shown in red. Since they are close to each other, they are fitted together. Details on the fit procedure are given in the text.

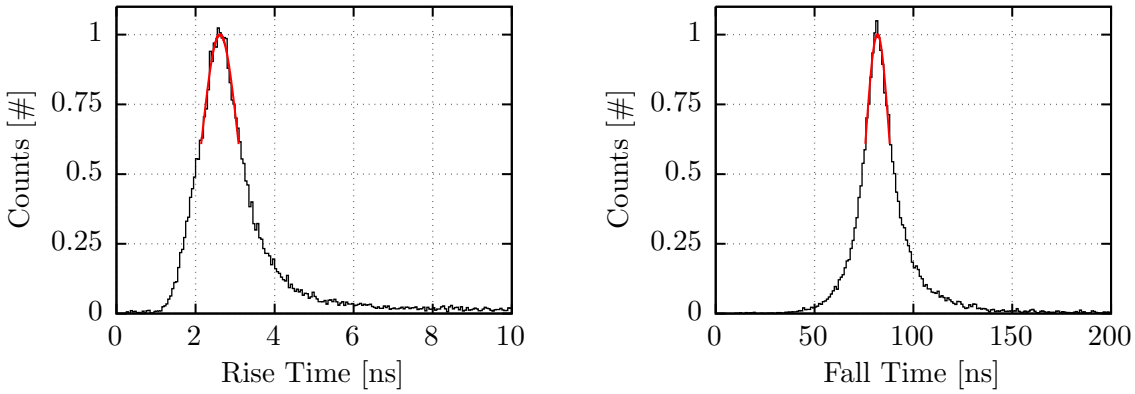

Figure 3.9: Distributions of the rise time **(a)** and the fall time **(b)** of a set of data. The most probable values of rise and fall time are extracted via fits to the distributions, respectively. They are repeatedly fitted with Gaussian functions within $1\,\sigma$ of the mean value. Although the distribution is not Gaussian, the function resembles the data well around the peak. The resulting most probable values are fixed in the second run of the fitting algorithm.

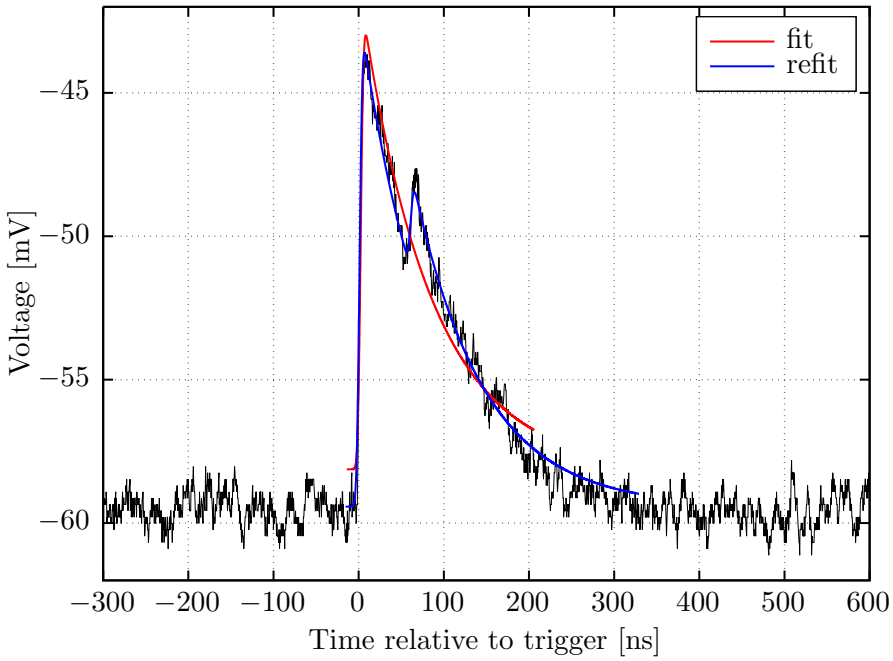

Figure 3.10: The peak finding algorithm and thus the primary fitting algorithm (red) recognises incorrectly only one peak. Using the refitting algorithm (blue) which is described in detail in the text, both pulses are fitted correctly. This algorithm enhances the discrimination of near pulses.

between data and initially fitted pulse. The associated time and amplitude are used as start parameters for the upcoming fit. If the added pulse is closer than $(\Delta t)_{\text{min}} = 3.0\,\text{ns}$ to the initial pulse it is discarded to ensure a stable procedure. Otherwise a fit is conducted containing the new combination of pulses. Both $\left(\chi^2_{\text{red}}\right)_{\text{min}}$ and $(\Delta t)_{\text{min}}$ can be fine-tuned further to make the algorithm sensitive to pulses that are in closer proximity. If the fit is successful and the resulting χ^2_{red} has improved sufficiently, the preliminary pulse is added permanently. This algorithm is repeated for each initial pulse until one of the abortion criteria applies. An example of how the refitting algorithm improves the analysis is shown in figure 3.10. Finally, all pulses within a waveform are sorted chronologically for further analysis.

3.3 Further Analysis

After having analysed each waveform and having stored the associated parameters in a TTree, in this module the results are combined to deduce physical parameters from the set of data. Therefore, the TTree containing the results of the waveform analysis is loaded. The pulse heights and the corresponding timestamps of all pulses found for one set of data are shown in figure 3.11. This part of the analysis can be performed multiple times without having to re-analyse the waveforms again since the associated TTree is not modified. Details on the particular methods within this module are given in the following chapter, where the results of the single methods are presented.

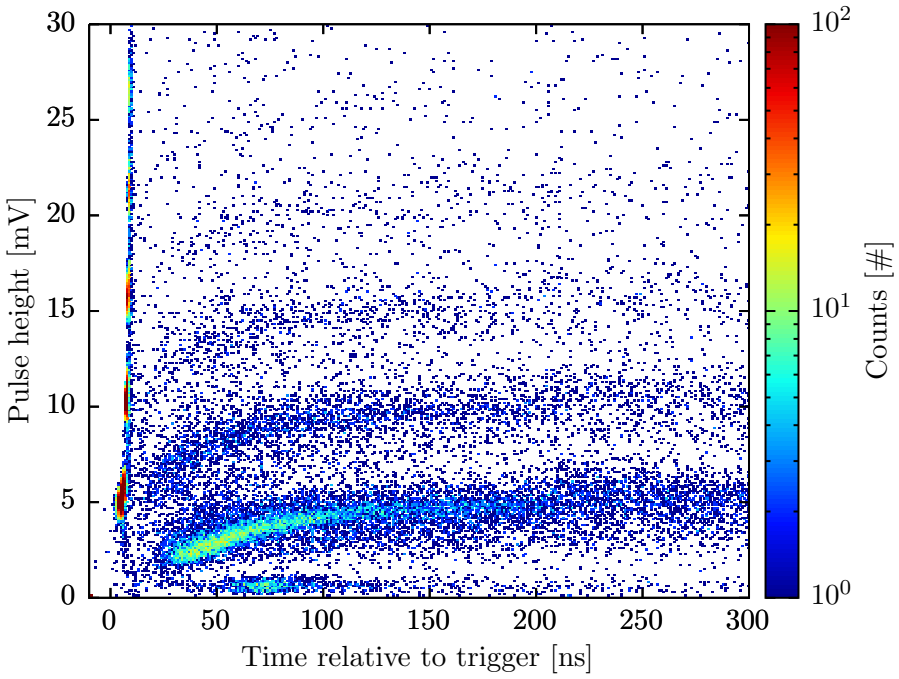

Figure 3.11: The pulse height is shown as a function of the pulse time for all pulses found for the set of data taken at a bias voltage of $-35\,\mathrm{V}$. The time of a pulse is given relative to the trigger time of the associated waveform. The colour denotes the abundance. For clarity, only pulses within $[-10\,\mathrm{ns} : 350\,\mathrm{ns}]$ are shown. The abundance of pulses right after the trigger is maximal. Additional pulses occur later in the waveform and are partially due to afterpulsing. The repetition of the pattern towards higher pulse heights is due to optical crosstalk. Pulses occurring within about 100 ns of a preceding pulse can have a diminished pulse height since the associated pixel has not fully recovered yet. The various effects and the physical information resulting from such a plot will be explained in detail in chapter 4.

Chapter 4

Characterisation of a SiPM in the Absence of Light

Contents

This chapter addresses the characterisation of a Silicon Photomultiplier (SiPM) of the type VUV-HD 2016 LF by FBK in the absence of light. At the same time, the respective characteristics are introduced. The characterisation is based on several measurements conducted at different bias voltages. The analysis of the measurements is based on the pulse fitting algorithm discussed in the previous chapter. The further analysis proceeds with several algorithms, each suiting the examination of particular characteristics of SiPMs.

At first, basic characteristics that are partially necessary for further investigations are reviewed, including the gain at a certain bias voltage and subsequently the breakdown voltage. Furthermore, the dark count rate, the recovery time of the pixels and the rise and fall times of the pulses as well as their dependencies on the overvoltage are examined. The second section includes the investigation of correlated avalanches, including optical crosstalk and afterpulsing. Where appropriate, the results obtained are compared to the limits posed by the nEXO experiment.

The complementary characterisation of the photon detection efficiency (PDE) could not be accomplished with this device since it was inoperative after the measurements presented here at dark condition. The reason for this are not known. Therefore, in the next chapter, the PDE is examined for another device.

4.1 Basic Characteristics

4.1.1 Gain

The gain of a Silicon Photomultiplier (SiPM) is defined as the amplification factor of a primary electron. As already seen in equation (1.13) the gain can be calculated by:

$$G = \frac{Q}{e} = \frac{C_\mathrm{D} \cdot \Delta U}{e} \sim \Delta U \tag{4.1}$$

This formula indicates a linear dependency of the overvoltage $\Delta U = |U_\mathrm{Bias} - U_\mathrm{Break}|$. Variations of the gain originate dominantly from the noise of the external amplification and readout system and from gain fluctuations among the pixels. Experimentally, the gain can be determined by two methods. One possibility is to calculate the released charge Q via a time integration of a given pulse:

$$G = \frac{Q}{e} = \frac{\int I\,(t)\ \mathrm{d}t}{e} = \frac{\int V_\mathrm{out}\,(t)\ \mathrm{d}t}{R_\mathrm{load} \cdot G_\mathrm{ampl} \cdot e} \tag{4.2}$$

where $\int V_\mathrm{out}\,(t)\ \mathrm{d}t$ is the area under a given pulse after amplification with a certain factor G_ampl. R_load denotes the input resistance of the amplifier. Another possibility is to only use the peak height of a given pulse. The latter method does not yield the real gain but rather a pulse height after external amplification that is proportional to the real gain. Nevertheless, in some cases this method allows for suppression of unwanted features that may compromise an analysis. In conclusion, the methods applied in this thesis are chosen to fit the demands of a given analysis.

To determine the gain, the mean pulse height corresponding one avalanche has to be identified. Therefore, all pulse heights associated with prompt pulses are combined in a histogram, which is called pulse height spectrum. A pulse height spectrum with six peaks is shown in figure 4.1 as an example for a measurement at $U_\mathrm{Bias} = -35\,\mathrm{V}$. Each discrete peak corresponds to an integral multiple of one photoelectron equivalent (p.e.), confirming the quantised nature of the SiPM's response (see also figure 3.2). The peaks are blurred due to electronics noise and intrinsic gain fluctuations between pixels whereas the former aspect is dominant. Each individual peak is fitted with a Gaussian distribution within $2\,\sigma$ of the mean value. Afterwards, a linear function is fitted to sets of mean pulse heights and corresponding number of p.e. at a certain bias voltage. The slope of the fit corresponds to the gain at that bias voltage. This procedure is performed for all measurements at dark condition to obtain the gain at the associated bias voltage. The plot containing all linear fits and the associated data is shown in figure 4.2.

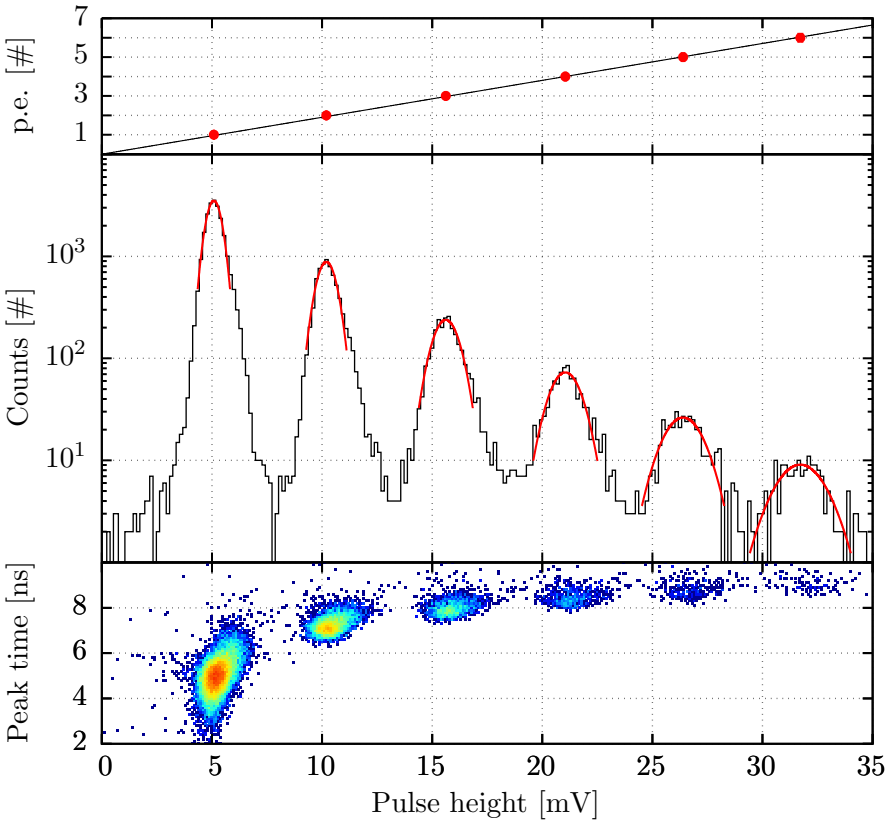

Figure 4.1: The centre figure shows the pulse height spectrum of one set of data. Only prompt pulses, meaning the triggered pulses, are considered in this plot. The correlation between pulse height and pulse time is shown in the bottom figure. The colours denote the abundance and are on a logarithmic scale. The plot indicates that with increasing pulse height the pulses occur slightly later. The resulting pulse height spectrum clearly indicates the distinct resolution of different photoelectron equivalent. Each peak is fitted with a Gaussian function around $2\,\sigma$ of the corresponding mean value. The resulting peak positions are shown in the top figure against the corresponding photoelectron equivalent confirming the expected linear dependency.

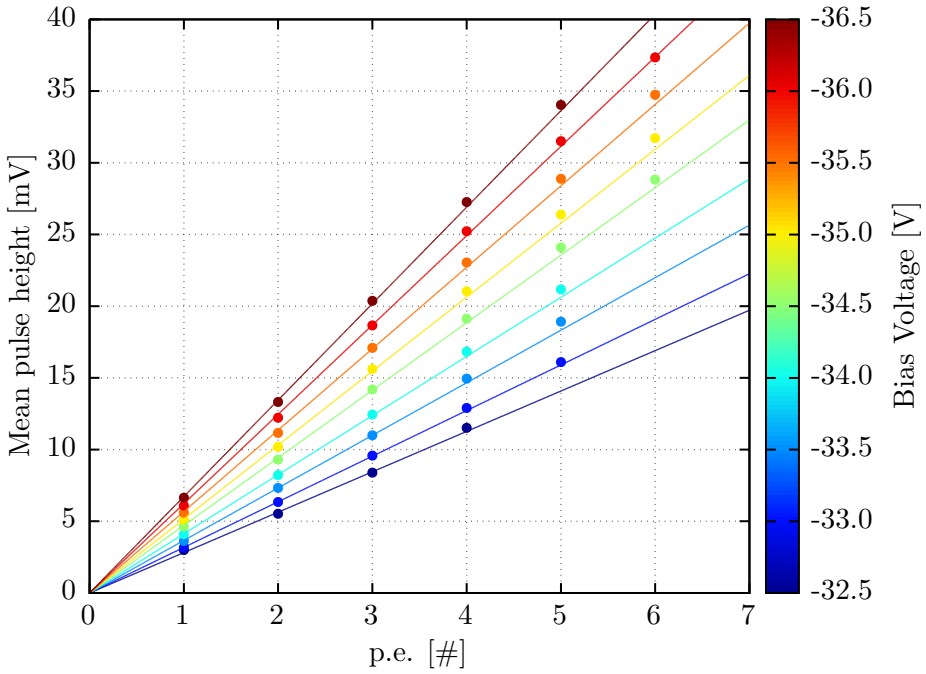

Figure 4.2: Linear dependency between the mean pulse heights and the photoelectron equivalent at several bias voltages denoted by colour. A linear fit to the data yields the gain, i.e. the slope of the fit at a certain bias voltage. The errors of the mean pulse heights have been considered in the fit, but they are not shown in the plot for clarity.

4.1.2 Breakdown Voltage

With the gain obtained for different bias voltages presented in the previous section, it is possible to deduce the breakdown voltage U_{Break} of the SiPM. Since it is defined as the voltage where a pixel is capable of exponential avalanches, equation (4.1) is suitable to determine the breakdown voltage. The equation can be rewritten as follows in order to show the dependency more clearly:

$$G\left(U_{\text{Bias}}\right) = \frac{C_{\text{D}}}{e} \cdot \left(U_{\text{Bias}} - U_{\text{Break}}\right) \tag{4.3}$$

The associated plot is shown in figure 4.3. The fit yields a breakdown voltage of:

$$U_{\text{Break}} = (-29.84 \pm 0.06)\,\text{V} \tag{4.4}$$

Given the small uncertainty of the breakdown voltage, the resulting uncertainties on the overvoltages are analogously small are thus omitted hereafter.

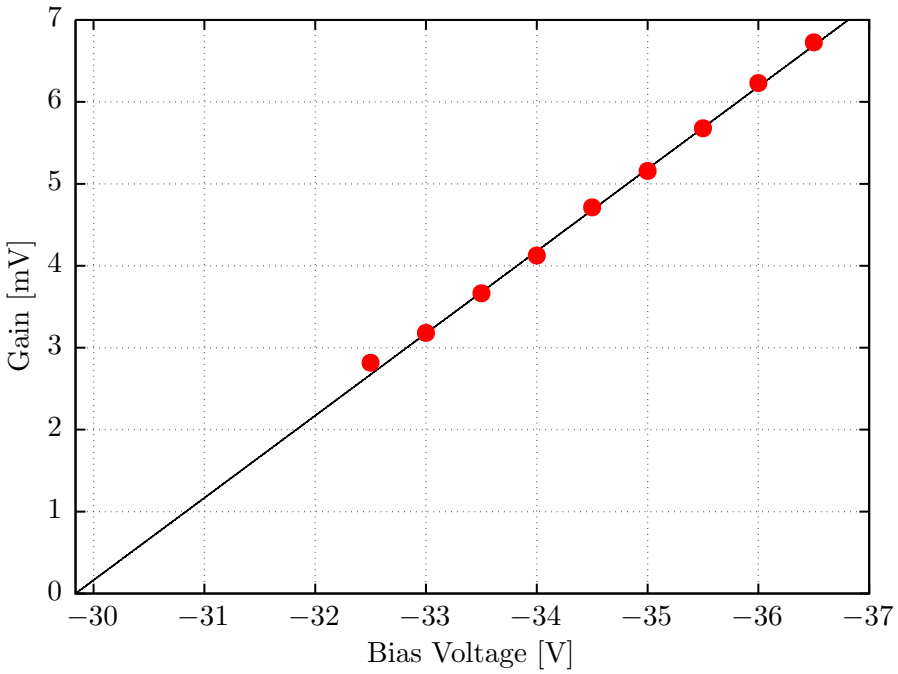

Figure 4.3: Dependency of the gain on the bias voltage. The gain was obtained in the previous paragraph. As discussed in the text, a linear dependency is expected. A linear fit function yields the breakdown voltage as the zero point.

4.1.3 Dark Count Rate

The signal rate of a SiPM in absence of light is called dark count rate (DCR). It poses a lower limit on the detectable flux. Signals arise due to thermal excitation of electrons in the active part of the SiPM where they are raised to the conduction band. Since the avalanche process is equivalent to that triggered by an external photon, both signals cannot be distinguished. There are two major mechanisms contributing to the DCR. The dominant one is thermal excitation whose rate is independent of the overvoltage because the intrinsic layer is fully depleted. However, the rate increases highly with the number of defects or impurities within the silicon. The probability of thermal excitation and thus the DCR can be reduced significantly by cooling. The second mechanism contributing to DCR is electron emission. Assisted by the high electric field in the multiplication region, electrons can tunnel through the band gap to the conduction band. This minor effect can be reduced by a decreased bias voltage. On the other hand, this reduces the gain and the photon detection efficiency. At constant temperature the probability to trigger an avalanche shows a linear dependency of the overvoltage. Therefore, by combining the rate of thermal excitation and the trigger probability, the DCR is linearly dependent on the overvoltage:

$$\mathrm{DCR} \sim \Delta U \tag{4.5}$$

From an experimental point of view there are several possibilities to measure the DCR. A relatively easy method is to count the number of pulses exceeding a certain threshold per second. When using this method, the dead time of the counting system has to be appropriately small to not expect additional DCR pulses within the dead time. A more sophisticated technique makes use of the Poissonian nature of DCR. The probability to detect n thermal pulses within a time interval Δt is given by:

$$P_\mu(n) = \frac{\mu^n \mathrm{e}^{-\mu}}{n!} \tag{4.6}$$

where μ denotes the average number of thermal pulses in Δt. The concept of how the time differences Δt are measured is shown in figure 4.4. Prompt pulses are required to belong to single avalanches whereas the subsequent pulses can belong to any number of avalanches. This selection ensures optical crosstalk-free prompt pulses and does not put any constraints on the subsequent pulses. A detailed discussion of both effects and the motivation for the selection criteria is given in section 4.2. The average number of thermal pulses can furthermore be expressed by a mean thermal noise rate R_D with:

$$\mu = R_\mathrm{D} \cdot \Delta t \tag{4.7}$$

Using this expression the probability to detect exactly zero signals in this time interval is given by:

$$P_\mu(0) = \mathrm{e}^{-\mu} = \mathrm{e}^{-R_\mathrm{D}\cdot\Delta t} = 1 - \int_0^{\Delta t} \rho_\mathrm{D}\left(\Delta t'\right)\, \mathrm{d}\Delta t' \tag{4.8}$$

The thermal noise probability density $\rho_\mathrm{D}(\Delta t)$ has been introduced in the last step. The following ansatz solves the equation:

$$\rho_\mathrm{D}(\Delta t) = R_\mathrm{D} \cdot \mathrm{e}^{-R_\mathrm{D}\cdot\Delta t} \tag{4.9}$$

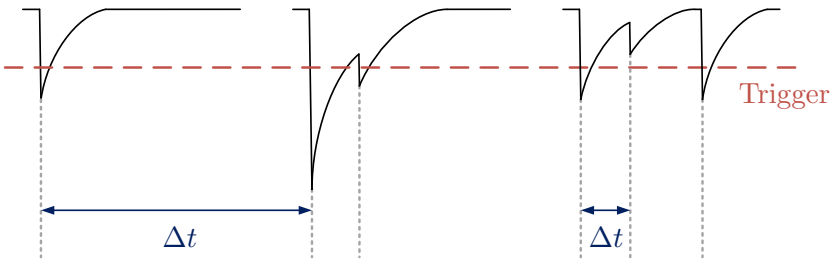

Figure 4.4: The time difference Δt of subsequent pulses is measured via the shown scheme. The red line indicates the trigger threshold of the measurement. Only time differences beginning at prompt pulses are taken into account. Thus only the first and possible second pulses in a waveform are considered and any additional pulses are omitted. Furthermore, the prompt pulse is required to correspond to a single avalanche. This approach will become important when calculating afterpulsing (see section 4.2.2).

This equation implies an exponential distribution of the time differences between subsequent thermal events. However, subsequent pulses can occur due to an effect called afterpulsing, too, as will be shown in section 4.2.2. In order to account for no afterpulsing event occurring upto time Δt, the equation is multiplied by the associated probability $P_{\overline{\mathrm{A}}}(\Delta t)$:

$$\rho_{\mathrm{tot}}(\Delta t) = P_{\overline{\mathrm{A}}}(\Delta t) \cdot \rho_{\mathrm{D}}(\Delta t) = P_{\overline{\mathrm{A}}}(\Delta t) \cdot R_{\mathrm{D}} \cdot \mathrm{e}^{-R_{\mathrm{D}} \cdot \Delta t} \tag{4.10}$$

Fitting this distribution yields the thermal noise rate R_{D} from which the DCR can be concluded [50, 75]. Two example distributions are shown in figure 4.5.

The thermal noise rate is converted to the DCR by scaling with the area of the SiPM. The area of the device used is about $6 \times 6\,\mathrm{mm}^2$ (see section 2.2.3). The DCR scaled by the area is an important parameter for the nEXO experiment and is supposed to not exceed $50\,\mathrm{Hz\,mm}^{-2}$ (see section 1.3.3). The resulting values of the DCR for all overvoltages that were measured are shown in figure 4.6. The observed trend indicates a linear dependency of the overvoltage. The absolute values are substantially better than the limit posed.

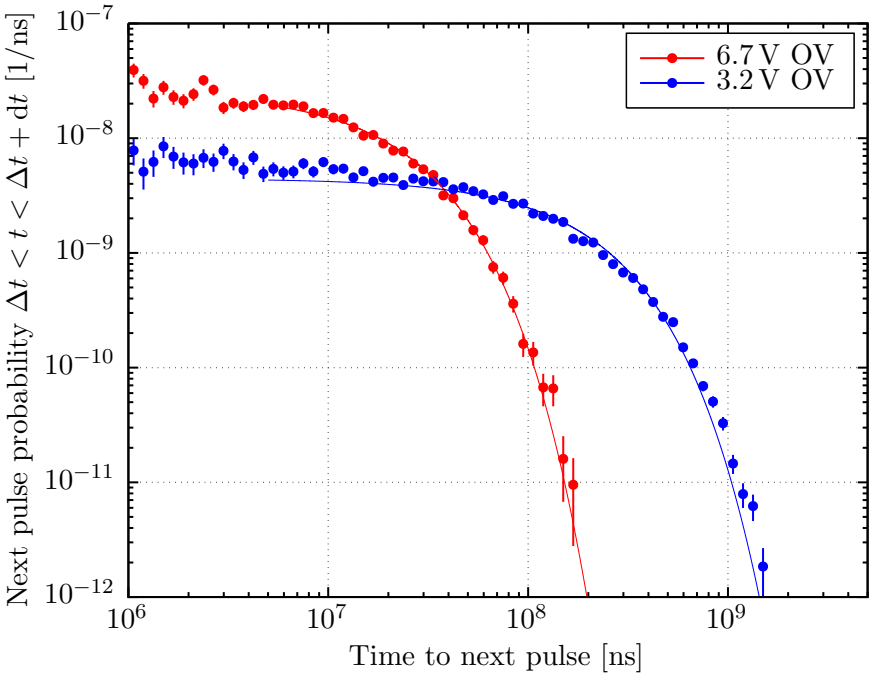

Figure 4.5: Distribution of the probability for next pulse to occur between Δt and $\Delta t + \mathrm{d}t$, $\mathrm{d}t$ being the width of the corresponding bin. The probability is calculated by measuring the time differences following every prompt pulse and thus does not add up to unity in this representation. The error bars are calculated assuming Poissonian uncertainties. The distributions are shown for different overvoltages to show their dependency qualitatively. It can be seen that a higher overvoltage leads to a higher DCR. A fit with equation (4.10) yields the thermal noise rate R_D at a certain bias voltage.

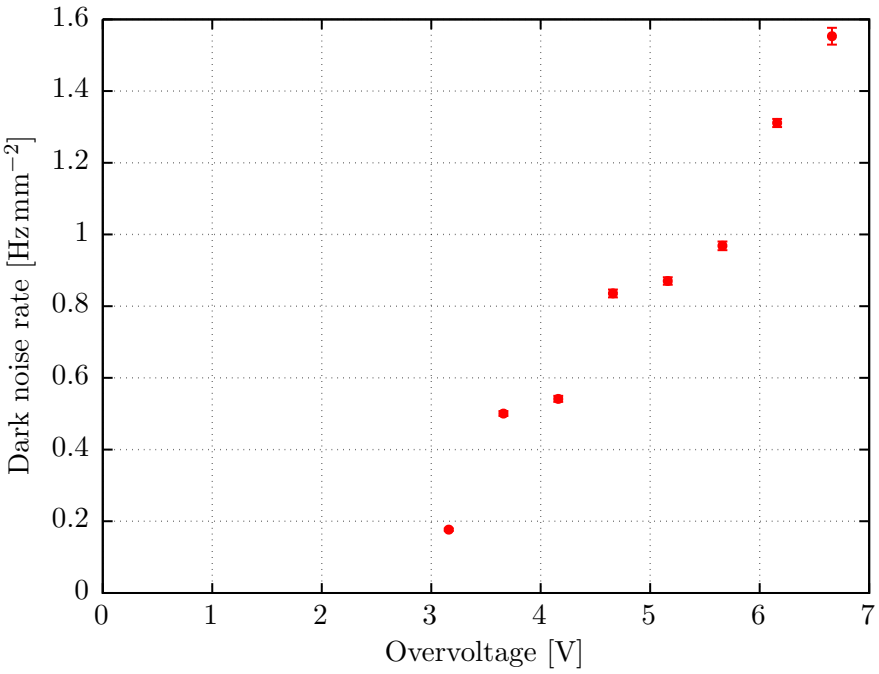

Figure 4.6: Resulting DCR per mm^2 for different overvoltages. The error bars originate from the fit presented in figure 4.5, but are relatively small. The trend indicates a linear dependency and the values are far below the limit the nEXO experiment posed on this parameter, which is 50 Hz mm^{-2}.

4.1.4 Recovery Time

After an avalanche takes place in a pixel of a SiPM, the voltage in that pixel drops to the breakdown voltage. The time needed to recharge the pixel is called recovery time and its time constant τ_R is governed by the product of the pixel capacitance C_D and the quenching resistance R_Q (see section 1.3.1):

$$U_{over}(t) = U_{over,0}\left(1 - e^{-t/\tau_R}\right) \tag{4.11}$$

Since the effective overvoltage $U_{over}(t)$ is diminished in comparison to the nominal overvoltage $U_{over,0}$ during the recovery, the effective gain in that specific pixel is as well. The recovery time constant is determined experimentally by analysing the pulse heights as a function of the time differences between one pulse and its predecessor. The selection and measuring concept were introduced in figure 4.4 and were adopted for this analysis. Figure 4.7 shows an example of the resulting data normalised to a single parent avalanche at that bias voltage. The resulting recovery time constants are shown in figure 4.8 for the overvoltages that were evaluated. The values indicate a slight decrease of the recovery time with increasing overvoltage.

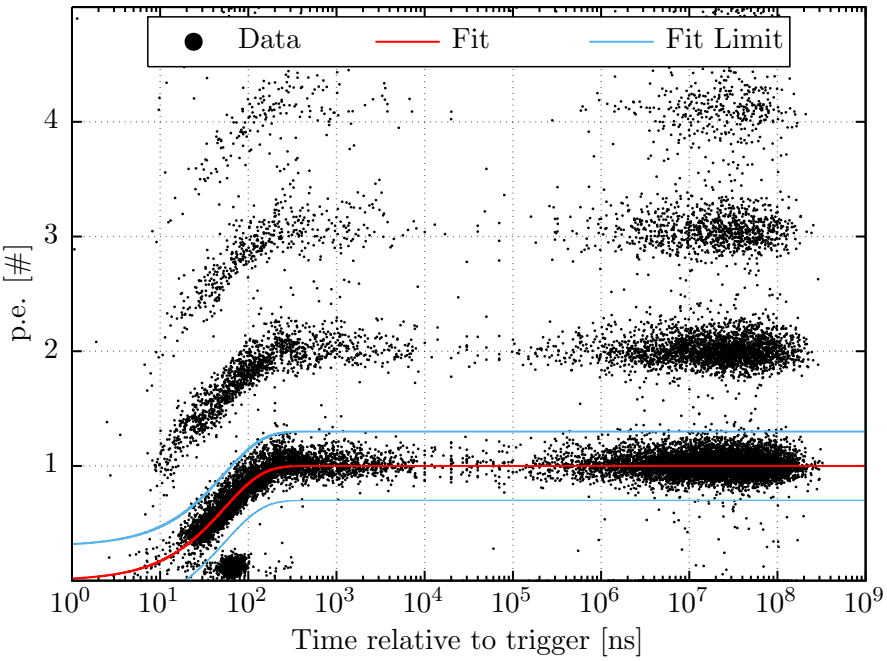

Figure 4.7: The pulse heights are shown as a function of the time since a previous prompt pulse. The previous pulse is required to belong to a single avalanche. The pulse heights are converted to photoelectron equivalent using the gain obtained in section 4.1.1. The repetition of the pattern obtained is due to optical crosstalk as will be discussed in section 4.2. The lower pattern is fitted several times within the given limits. The best fit results are obtained for fit limits that arise from shifting the former fit vertically by 0.3 p.e..

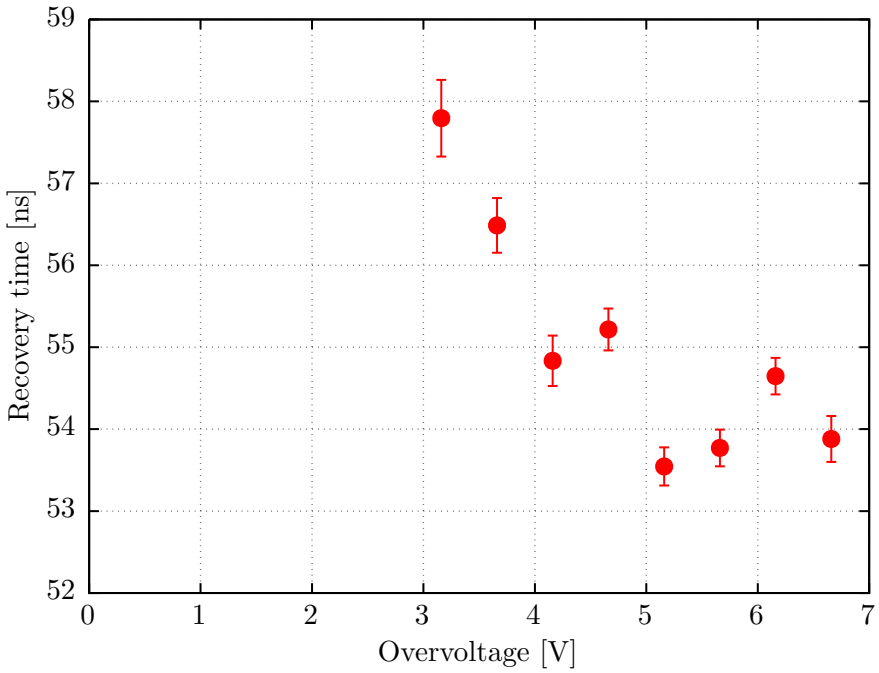

Figure 4.8: Recovery time constants resulting from the fit performed in figure 4.7 as a function of the overvoltage. The errors correspond to the errors obtained in the fit. The values indicate a slight decrease of the recovery time constant with increasing overvoltage. The error of the first value is significantly larger because of small statistics in the specific set of data for this kind of analysis. This problem originates from the relatively small pulses at that overvoltage compared to the noise.

4.1.5 Rise and Fall Time

A pulse is characterised by a rise time σ and a fall time τ governing the discharge and the recharge of a pixel, respectively. The former is proportional to $\sigma \propto R_\mathrm{D} C_\mathrm{D}$ and the latter to $\tau \propto R_\mathrm{Q} C_\mathrm{D}$ as shown in section 1.3.1. The function used for fitting the pulses that was introduced in equation (3.5) contains both parameters. As discussed in section 3.2, the fitting algorithm is performed twice. The first run is dedicated to determining both rise and fall time and fixing the most probable values for the second run. An example of the resulting distributions was shown in figure 3.9. The most probable values are determined by fitting a Gaussian distribution to the distribution of both rise and fall time. More information is given in the stated section. Figure 4.9 shows the dependencies of both parameters on the overvoltage. While the rise time increases roughly linearly with increasing overvoltage, the fall time decreases in the same way. Although these results are not stringently motivated physically they support the two-stage procedure of the fitting algorithm. Since the resulting parameters are not independent of the overvoltage, they have to be determined for every single measurement.

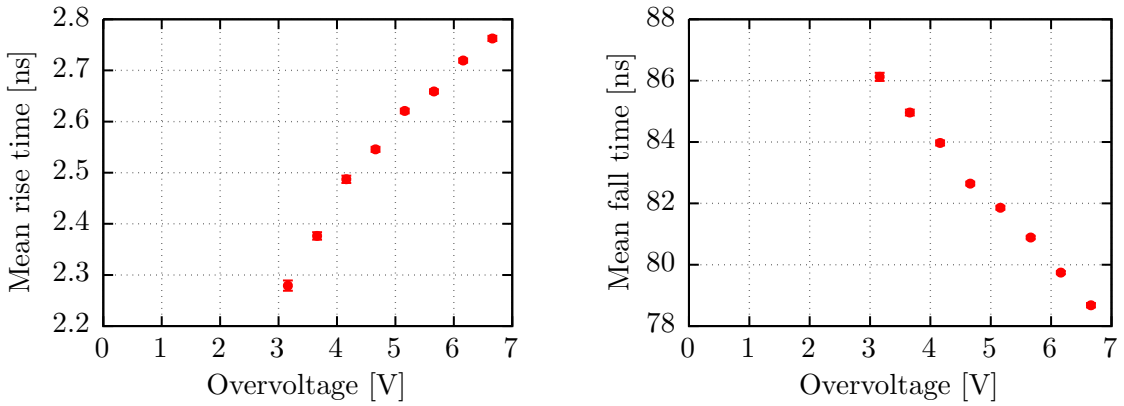

Figure 4.9: Dependency of the rise time **(a)** and of the fall time **(b)** on the overvoltage. Error bars are deduced from fits to the associated distributions as were shown in figure 3.9. Both resulting trends indicate a roughly linear dependency but with contrary signs.

4.2 Correlated Avalanches

As seen in section 4.1.3, thermal excitation of electrons can cause avalanches despite the absence of light. Given the order of magnitude of the DCR it is highly unlikely that multiple independent avalanches occur within several nanoseconds. Therefore, avalanches that are caused by another preceding one are called correlated. Two major effects cause correlated avalanches. On the one hand, there is prompt and delayed optical crosstalk (CT) and on the other hand, there is afterpulsing (AP). Both effects will be discussed within this section. An example of a parent pulse suffering both effects is shown in figure 4.10. The distribution of amplitudes of parent pulses and subsequent pulses is shown in figure 4.11 as a function of the time since the pixel was triggered. Using this distribution the aspects of both effects can be illustrated.

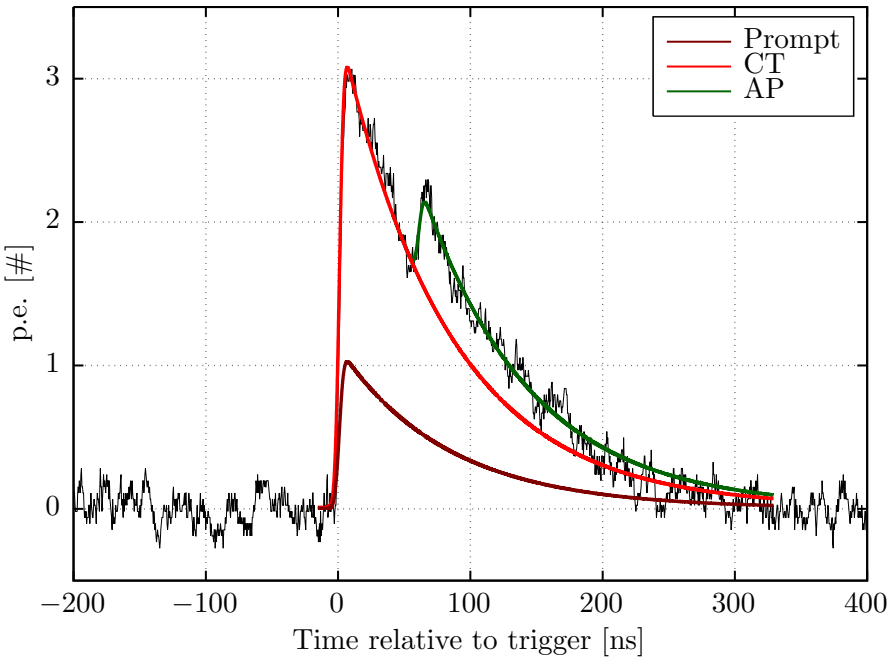

Figure 4.10: The waveform introduced in figure 3.10 suffering both prompt CT and AP. The parent pulse (brown) is caused by thermal excitation and triggers two more avalanches due to prompt CT (red) which results in a pulse equivalent of 3 p.e.. A delayed avalanche is triggered in one of the previously triggered pixels due to AP (green), causing a pulse with a smaller amplitude because the pixel had not completely been recharged up to that point.

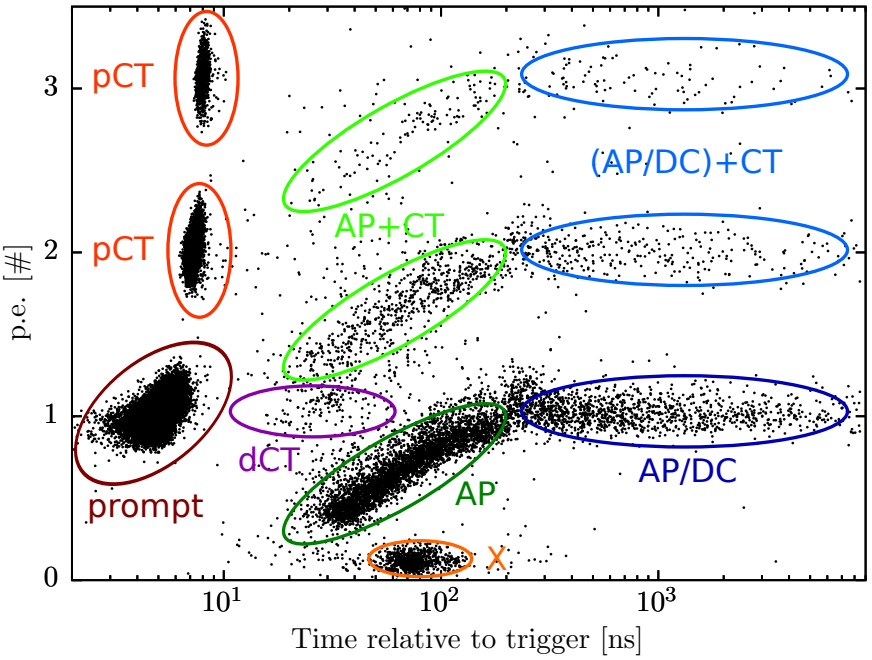

Figure 4.11: Distribution of photoelectron equivalent for parent and subsequent pulses as a function of the time since the pixel was triggered. Prompt pulses (brown) dominantly lie within 10 ns and are 1 p.e.. Prompt pulses suffering prompt CT (red) are measured as pulses with multiple p.e.. Avalanches due to delayed CT (purple) are identified separately and are thus measured as additional pulses with 1 p.e.. Parent pulses suffering AP are measured as a parent pulse and a delayed pulse (green) which typically has a lower amplitude than the parent pulse since the pixel has not fully recovered yet (see section 4.1.4). Since these delayed pulses can suffer CT as well, the band structure is repeated (light green). Pulses occurring with larger delay to the parent pulse can originate from AP or thermal excitation (blue) and can suffer CT as well (light blue). The origin of these delayed pulses can only be determined on a statistical basis. The pulses marked with X do not correspond to any physical effect and their origin has to be investigated further.

4.2.1 Optical Crosstalk

Electrons that possess sufficient energy to enter the conduction band are called hot carriers and are able to produce photons during an avalanche. On average, about $2.9 \cdot 10^{-5}$ photons with an energy exceeding the bandgap of silicon of 1.1 eV are produced per electron that contributes to an avalanche, resulting in about 30 photons in a typical avalanche [76]. These photons may be absorbed (a) within the pixel and disappear in the avalanche, (b) in an inactive part of the SiPM or (c) in a neighbouring pixel and may trigger additional avalanches. This process is called optical crosstalk (CT). In particular, photons near the infrared spectral range have a longer attenuation length and are thus more likely to be absorbed in a neighbouring pixel. It was shown that CT events are triggered dominantly in directly adjacent pixels [77]. To reduce this undesired effect some manufactures implement trenches filled with optically opaque materials between the pixels [78]. This technique does not eliminate CT completely but rather reduces its probability to occur [79]. On the other hand, by introducing trenches the geometrical efficiency and thus the photon detection efficiency decreases.

Since most of the photons causing a CT avalanche are absorbed directly in the avalanche region of a neighbouring pixel, the resulting signal will be quasi instantaneous and is superimposed on the initial avalanche. Therefore, this process is called prompt CT. On the other hand, photons can be absorbed in the intrinsic layer of the SiPM, producing a photoelectron that drifts to the avalanche region and triggering a delayed avalanche. This process is known as delayed CT. Since the contribution of the latter process is negligible with the devices used, it will not be investigated further. For simplicity, hereafter, CT will denote only prompt CT.

The signature of an avalanche triggered by a photon or by thermal excitation of an electron is identical to one due to CT. Thus, pulses containing an initially triggered avalanche and one resulting from CT will be detected as two avalanches. Since the avalanche due to CT may cause additional avalanches, the final pulse may contain further avalanches. Since there is no consistent definition of the probability for CT, the two most common ones are applied within this thesis. Either way, the probability of multiple uncorrelated thermally induced avalanches within a few nanoseconds is extremely small[1] so that higher-order pulses can fully be accounted for as CT pulses.

One way to define the CT probability P_{CT} is to investigate the probability of an avalanche initiating additional avalanches in different pixels, independent of the number of additional avalanches. In order to do so, the pulse height spectrum of prompt pulses at dark condition is examined. Given the above definition, P_{CT} is determined by calculating the probability P_1 of a prompt pulse to belong to a single avalanche. The deviation from one is thus the probability P_{CT} for CT:

$$P_{\mathrm{CT}} = 1 - P_1 = 1 - \frac{N_1}{N_{\mathrm{tot}}} \tag{4.12}$$

Experimentally, the number of prompt pulses N_1 that are smaller than 1.5 p.e. is compared to the total number of prompt pulses N_{tot} detected to obtain P_1. The method is illustrated in figure 4.12.

[1] A first-order estimation of the probability of two uncorrelated avalanches within $\Delta t = 10\,\mathrm{ns}$ is about $P_2 \simeq \dot{N}_2/\dot{N}_1 = \dot{N}_1 \cdot \Delta t = 10^{-6}$, where $\dot{N}_1$ and $\dot{N}_2$ denote the rate of one and two uncorrelated avalanches. The approximation conservatively assumes a DCR of 100 Hz

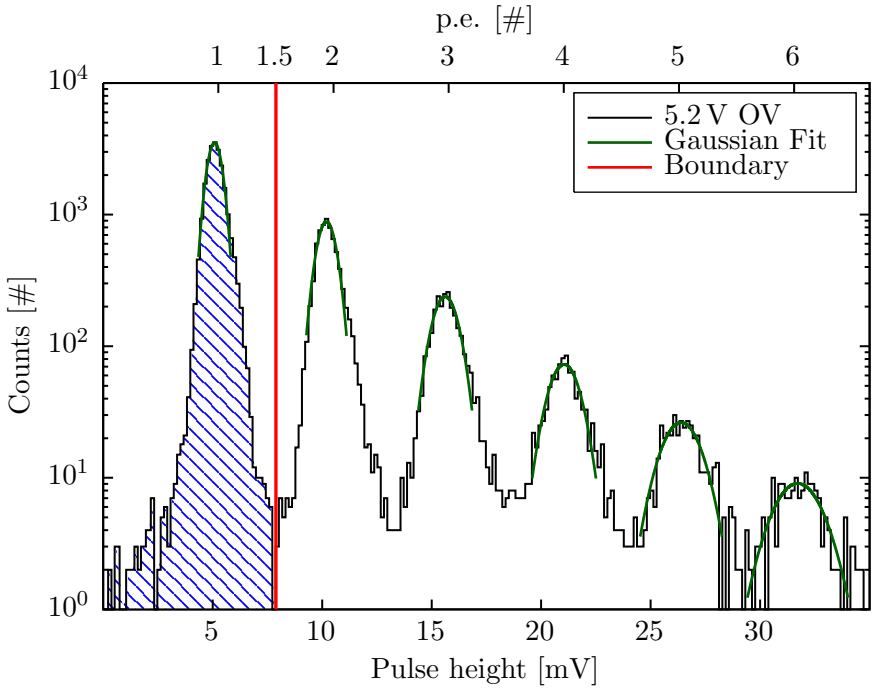

Figure 4.12: Pulse height spectrum of prompt pulses. Both methods discussed in the text to calculate P_{CT} are illustrated. For both methods, the mean pulse height corresponding to a single avalanche is calculated by a linear fit (see section 4.1.1) and is shown on the top axis. The boundary (red) for the first method corresponds to 1.5 p.e. by which pulses are discriminated as belonging to 1 p.e. (blue) or not.

Another way to define the probability P_{CT} for CT is to determine the probability of an avalanche to initiate exactly one additional avalanche. The main difference to the previous method is the weighting of pulses depending on their pulse height since, for example, a pulse equivalent of 3 p.e. suffered CT twice. This method also uses the pulse height spectrum of prompt pulses at dark condition. Unlike the other method, the pulses are now rescaled by the gain at which the photoelectron equivalent is obtained (see section 4.1.1). Hence, the resulting pulse height spectrum is rescaled as is shown in figure 4.12. The mean value of the rescaled distribution equals the mean number of photoelectron equivalents within a prompt pulse. Its deviation from one yields the probability P_{CT} for CT:

$$P_{\mathrm{CT}} = \frac{N_{\mathrm{tot}}^{-1} \cdot \sum_{i=0}^{N_{\mathrm{tot}}} A_i\,[\mathrm{mV}]}{G} - 1 = N_{\mathrm{tot}}^{-1} \cdot \sum_{i=0}^{N} A_i\,[\mathrm{p.e.}] - 1 \tag{4.13}$$

where N_{tot} denotes the total number of prompt pulses and A_i [mV] and A_i [p.e.] the pulse height before and after rescaling, respectively.

The number of created photons in an avalanche is proportional to the number of charge carriers in the avalanche, which makes it also dependent on the overvoltage (see section 4.1.1). At the same time, the probability to trigger an avalanche when absorbing a photon, e.g. in

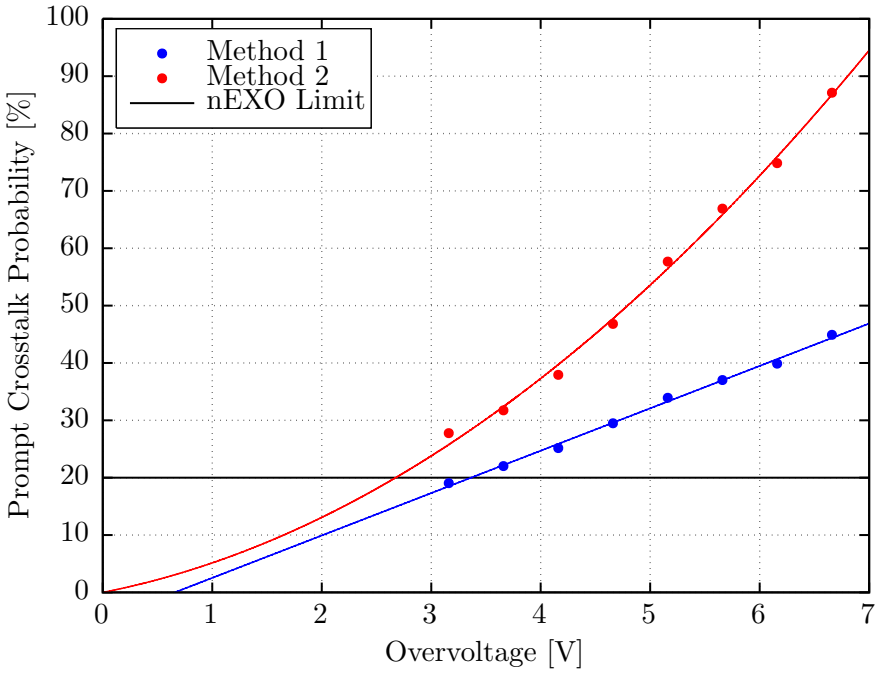

Figure 4.13: The resulting probabilities for CT as a function of the overvoltage. Both methods discussed in the text are shown. The values resulting from the first method indicate a linear dependency and exceed the limit of the nEXO experiment above an overvoltage of 3.4 V. The second method yields a quadratic dependency of the overvoltage and the probability for CT exceeds the nEXO limit above an overvoltage of 2.7 V.

a neighbouring pixel, is proportional to the overvoltage, resulting in a quadratic dependency of the CT probability on the overvoltage [77], which is shown in figure 4.13. On the other hand, the first method empirically yields a linear dependency as is shown in figure 4.13, since pulses suffering CT are only accounted for once, regardless of the number of avalanches due to CT. This dependency was observed by several publications, like for example [63], alike. For overvoltages larger than 3.4 V or 2.7 V, depending on the method chosen, P_{CT} exceeds the limit of 20 % correlated avalanche probability posed by the nEXO experiment. This, however, does not include the afterpulsing probability yet.

Figure 4.14 compares the CT probability P_{CT} obtained for this device with those of other devices as a function of the overvoltage. Shown are devices from various manufacturers of SiPMs that were examined for the nEXO experiment. The figure is split to distinguish values obtained by the both methods discussed previously. As can be seen in the figure, the CT probability is rather large compared with the former device (FBK 2010) and compared with devices like the VUV3 by Hamamatsu or the PM3350 by KETEK. Older devices, like the MEG by Hamamatsu or the PM3375 by KETEK without trenches, have larger probabilities for CT compared to the device tested. Therefore, in order to satisfy the limits posed by nEXO, the SiPM has to be operated at a relatively low overvoltage where, on the downside, the photon detection efficiency and the gain is low as well.

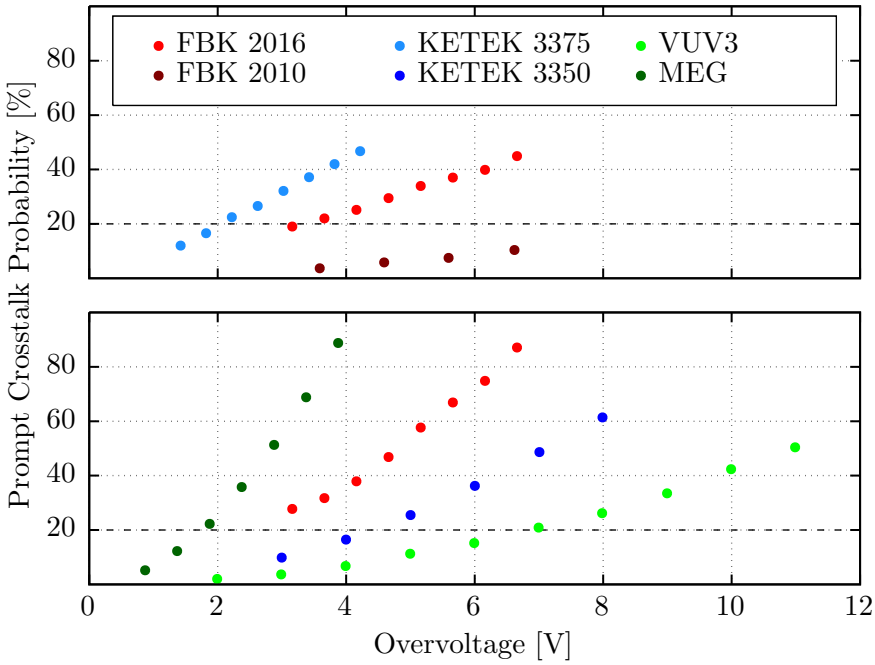

Figure 4.14: The CT probabilities P_{CT} as a function of the overvoltage for different devices. The top figure compares the probabilities obtained with the first method discussed in the text for this device (FBK 2016) with the ones of a KETEK 3375 [80] as well as of a FBK 2010 [63] SiPM. The bottom figure compares the CT probabilities obtained with the second method for this device with the ones of a MEG [75], a VUV3 [75] as well as of a KETEK 3350 SiPM. The latter measurements were conducted at TRIUMF, VN, CA, by Michael Wagenpfeil in May, 2016. The limit posed by the nEXO experiment on the probability for correlated avalanches of 20 % is shown in both figures.

4.2.2 Afterpulsing

Besides optical crosstalk, there is another effect of correlated avalanches which is called afterpulsing (AP). It occurs when charge carriers of an avalanche are trapped in deep level defects in the silicon. These charge carriers are eventually released according to an exponential time distribution with a specific life time τ_A depending on the type of defect. The released charge carrier may trigger an avalanche that is delayed in time compared to the parent avalanche. Since the signature of this avalanche is identical to an uncorrelated one due to thermal excitation, it cannot be distinguished on a single pulse basis. AP is rather identified on a statistical basis since the probability of delayed avalanches is increased by AP compared to the probability of DCR.

Therefore, in order to measure AP the time distribution of subsequent pulses is investigated as suggested in [63, 81, 82] and introduced in figure 4.4. The parent pulses are required to correspond to single avalanches, i.e. all pulses that suffer CT are omitted, to be able to measure the probability of AP of a single avalanche. Furthermore, parent pulses are required to be in a window of $[-10\,\mathrm{ns} : 20\,\mathrm{ns}]$ around the trigger in order to properly account for the dead time of the oscilloscope (8 µs) after each waveform. Parent pulses are also required to be the first pulse in that certain waveform, whereby no pulse can occur during the previous 1 µs, to ensure that these pulses are not caused by AP themselves. On the other hand, subsequent pulses can be of any amplitude in order to not reject subsequent pulses suffering from CT as shown in figure 4.11. Pulses that have a relatively small delay of less than about 100 ns have a diminished amplitude since the pixel has not recovered to the nominal overvoltage yet. The resulting time distribution is shown in figure 4.15 for an overvoltage of 5.2 V.

The probability density $\rho_\mathrm{A}(t)$ for an avalanche due to AP can be deduced analogously to the one for DCR. The only difference is that the probability to trigger an avalanche depends linearly on the overvoltage and thus on the recovery of the pixel. Therefore, combining both equation (4.9) and equation (4.11), the probability density for an AP is given by:

$$\rho_\mathrm{A}(t) = \left(1 - \mathrm{e}^{-t/\tau_\mathrm{R}}\right) \cdot R_\mathrm{A} \cdot \mathrm{e}^{-R_\mathrm{A} \cdot t} \tag{4.14}$$

where τ_R denotes the recovery time constant which was determined in section 4.1.4 and where $R_\mathrm{A} = \tau_\mathrm{A}^{-1}$ denotes the inverse trapping life time. When, for simplicity, assuming only one AP time constant, the total probability density $\rho_\mathrm{tot}(t)$ for a subsequent avalanche that occurs after a time t combines both AP and pulses from thermal excitation. Both probability densities are mutually exclusive, meaning a pulse from thermal excitation or AP occurs after a time t while at the same time no AP or thermally generated pulse occurred between 0 and t. This ansatz leads to:

$$\rho_\mathrm{tot}(t) = \underbrace{\left[1 - \int_0^t \rho_\mathrm{A}\left(t'\right)\,\mathrm{d}t'\right]}_{P_{\overline{\mathrm{A}}}(t)} \cdot \rho_\mathrm{D}(t) + \underbrace{\left[1 - \int_0^t \rho_\mathrm{D}\left(t'\right)\,\mathrm{d}t'\right]}_{P_{\overline{\mathrm{D}}}(t)} \cdot \rho_\mathrm{A}(t) \tag{4.15}$$

The terms in brackets can be rewritten by introducing the probabilities to not observe a thermally generated pulse $P_{\overline{\mathrm{D}}}(t)$ (see equation (4.8)) or one due to AP $P_{\overline{\mathrm{A}}}(t)$ by that time.

In reality, instead of only one type of defect in the silicon there can be n_A different types, resulting in multiple trapping life times τ_{A_i}. This behaviour was observed for many different SiPMs with up to four different kinds of defects [63]. Thus, the final equation is given by:

$$\rho_\mathrm{tot}(t) = \rho_\mathrm{D}(t) \cdot \prod_{i=0}^{i<n_\mathrm{A}} P_{\overline{\mathrm{A}_i}}(t) + P_{\overline{\mathrm{D}}}(t) \cdot \sum_{i=0}^{i<n_\mathrm{A}} \left[\rho_{\mathrm{A}_i}(t) \cdot \prod_{j=0}^{\substack{j\neq i \\ j<n_\mathrm{A}}} P_{\overline{\mathrm{A}_j}}(t) \right] \tag{4.16}$$

where the product in the first term garantuees that there are no avalanches caused by any AP component occuring between 0 and t. The sum in the second term combines the probability densities of any AP component while at the same time ensuring that the avalanche does not belong to another AP component. Both the pulse finder and the fitting algorithm can miss pulses that are very close to each other or pulses whose amplitudes are very small. Therefore, equation (4.16) is fitted only for time differences larger than 15 ns after the parent pulse. In order to properly account for this feature as well as the oscilloscope's dead time, the function is expanded adequatly as is described in [63][2].

As seen in figure 4.15, the distribution is best adapted by the fit when introducing $n_\mathrm{A} = 3$ time constants. This corresponds to three different types of defects in the silicon with characteristic trapping life times τ_{A_i}. The dependencies of the life times on the overvoltage are shown in figure 4.16. All trends indicate a slight decrease of the life time with increasing overvoltage. Additional types of defects may exist with lower life times than about 10 ns. In order to be able to resolve such short life times, the accuracy of the fitting algorithm has to be increased further.

Using the life times, the probability for a parent avalanche to suffer AP in a given time interval can be calculated. This is done by integrating equation (4.14) in the particular interval. The resulting AP probabilities are shown in figure 4.17, where the overall probability as well as the one for AP within the first 1 µs is depicted. The latter probability is of particular interest for the nEXO experiment. However, both probabilities do not differ strongly since AP occurs dominantly within the first 1 µs. As expected, the probability of an avalanche to suffer AP increases with increasing overvoltage. The obtained values are in contradiction to the ones stated by the manufacturer [83]. On the one hand, this behaviour can be due to real AP and therefore should be reproducible by collaborators or, on the other hand, result from a not fully understood performance of the analysis software. Either way, the observed behaviour has to be investigated further to deduce its origin which exceeds the scope of this thesis.

[2]This algorithm was partially adapted from collaboration partners at TRIUMF, VN, CA.

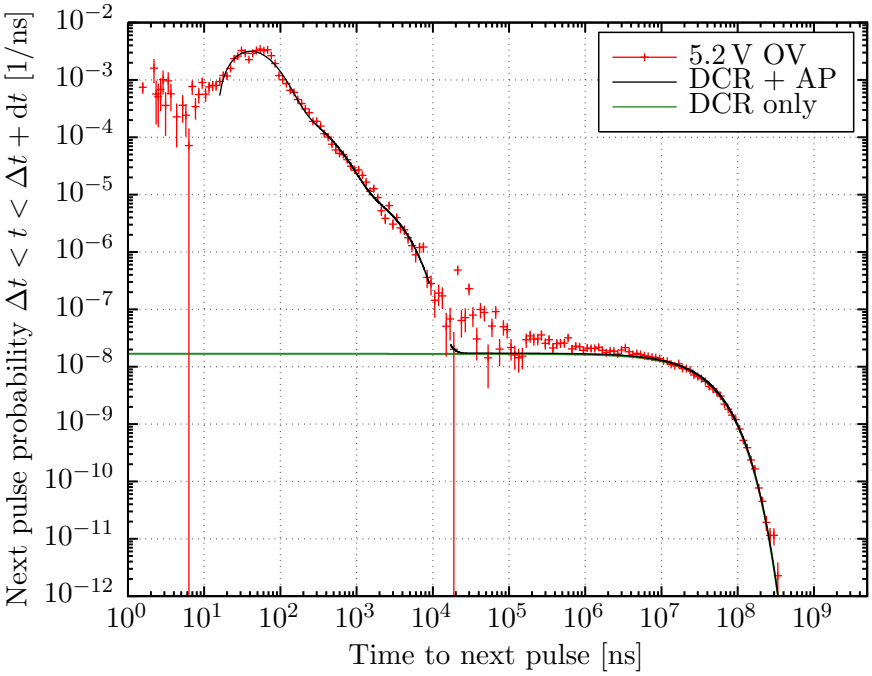

Figure 4.15: Time distribution of the probability for the next pulse to occur between Δt and $\Delta t + \mathrm{d}t$, $\mathrm{d}t$ being the width of the corresponding bin. The error bars are calculated assuming Poissonian uncertainties. The time distribution is measured as indicated in the schematic in figure 4.4. Only subsequent pulses of prompt parent pulses corresponding to a single avalanche are taken into account in order to be able to deduce the AP probability. More details on the selection of the pulses is given in the text. The right tail corresponds to DCR events whereas the left part is dominated by events due to AP. A fit using equation (4.16) is performed for values larger than 15 ns, as for smaller values the accuracy of the fitting algorithm is poor. The gap at 9 - 17 µs is due to the oscilloscope's dead time. The best fit result is obtained by including $n_{\mathrm{A}} = 3$ AP time constants. For comparison, the contribution that is solely due to DCR is shown as well.

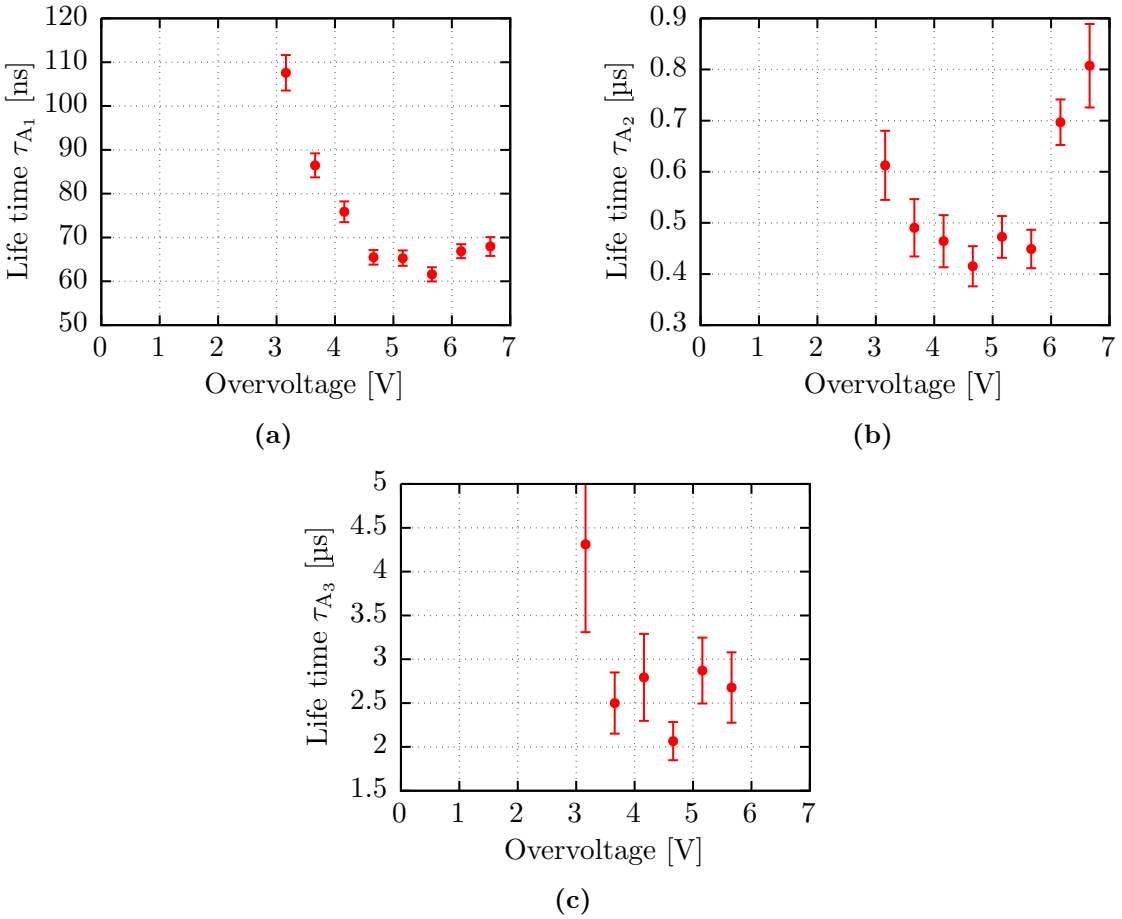

Figure 4.16: Life times of AP trapping centres as function of the overvoltage. Note the different time scales. The errorbars only account for statistical errors resulting from the fits using equation (4.16), whereas additional systematics are not included. Therefore, the errorbars are likely to be underestimated. For overvoltages above 6 V, the values deviate from the descending trend. A possible explanation is that the larger the overvoltage, the more correlated pulses occur on average, whose distinction may be challenging for the analysis algorithm. The associated values for τ_{A_3} lie outside the bounds and are omitted for clarity.

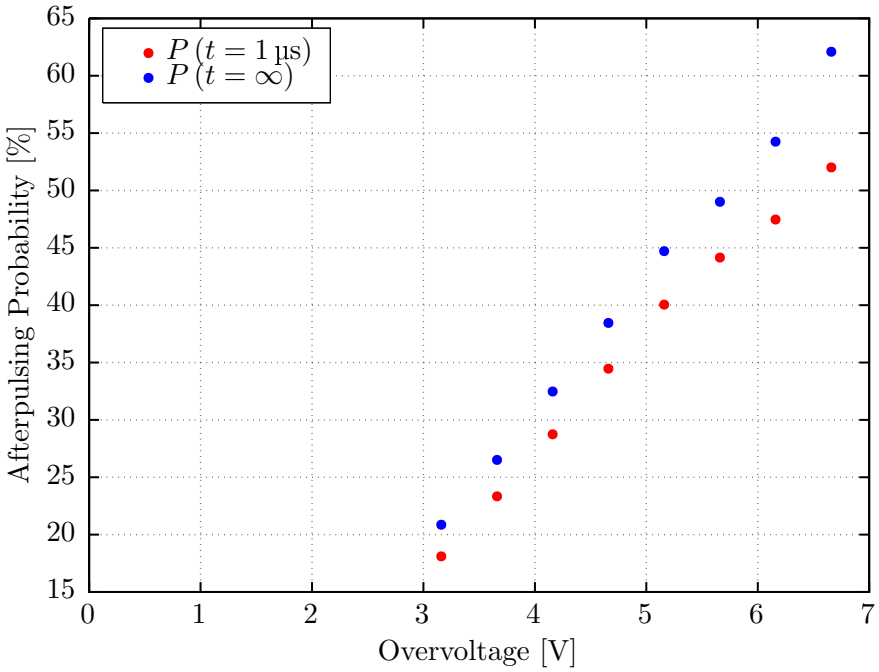

Figure 4.17: The AP probability as a function of the overvoltage. Both the overall probability for AP as well as the AP probability within the first 1 µs are shown. The obtained trend is discussed in the text.

Chapter 5

Characterisation of a SiPM with Xenon Scintillation Light

Contents

This chapter adresses the examination of the photon detection efficiency (PDE) where a Silicon Photomultiplier (SiPM) of the type VUV-HD 2016 STD by FBK serves as an example. First, the concept of PDE is motivated and linked to other characteristics of a SiPM. Afterwards, the experimental approach is introduced as well as its realisation in a GEANT4 based simulation [84] in order to validate and to support the experimental approach. The PDE is measured with the scintillation light of gaseous xenon (GXe) in combination with a Photomultiplier Tube (PMT), that serves as reference detector. Several features of the setup are examined by both simulation and measurement.

The examination of the PDE could not be accomplished quantitatively but is rather performed on a qualitative basis. The limitations preventing a quantitative analysis are discussed. For one, the contamination of the GXe increased with time. In addition to that, the gain of the tested device could not be derived due to a significant noise contribution that was accompanied by a large leakage current.

5.1 Photon Detection Efficiency

5.1.1 Theoretical Considerations

A fundamental characteristic of Silicon Photomultipliers (SiPMs) is their efficiency to detect photons. Although, independent of the value of the photon detection efficiency (PDE), the number of impinging photons can be deduced from the PDE. The uncertainties of this extrapolation decrease for higher values of the PDE. Hence, a high PDE is of importance for experiments working with low light intensities.

The PDE combines several components indicating the total probability to detect an impinging photon, or from the experimental point of view the number of detected photons N_{det} in relation to the total number of impinging photons N_{tot}:

$$PDE = \frac{N_{\mathrm{det}}}{N_{\mathrm{tot}}} \tag{5.1}$$

From a theoretical point of view, the PDE comprises (a) the efficiency to absorb an impinging photon in the active part of a pixel and to create an electron-hole pair, called quantum efficiency (QE). Furthermore, it includes (b) the probability to subsequently trigger an avalanche, called trigger probability P_{trig}, and (c) the fill factor FF which is the ratio of photosensitive area to total area.

$$PDE\left(\lambda, \Delta U\right) = QE\left(\lambda\right) \cdot P_{\mathrm{trig}}\left(\Delta U\right) \cdot FF \tag{5.2}$$

The QE comprises the reflectivity R at the border of air or surrounding material and silicon. Because the losses due to reflection between air and silicon can be large, the anti-reflective coating used in most SiPM is crucial. In addition to the probability for no reflections at the border, the probability to be absorbed in the active part of the SiPM has to be considered. This photon attenuation is given by the Beer-Lambert-Law:

$$I\left(\lambda, z\right) = I_0\left(\lambda\right) \cdot \mathrm{e}^{-\alpha(\lambda) z} \tag{5.3}$$

where $I\left(\lambda, z\right)$ and $I_0\left(\lambda\right)$ denote the intensities in the multi photon consideration at the depth z and before penetration, respectively. α is the characteristic absorption coefficient. Combining both, the QE is given by:

$$QE\left(\lambda\right) = \left(1 - R\right)\left(1 - \mathrm{e}^{-\alpha(\lambda) L_{\mathrm{d}}}\right) \tag{5.4}$$

where the first term governs the transmittance at the border and the second term the probability of a photon with a wavelength λ to be absorbed in the depleted part of the SiPM with a thickness L_{d}. Using this equation, the PDE can be optimised at a certain wavelength by ensuring $\alpha\left(\lambda\right) L_{\mathrm{d}} \gg 1$ in order to maximise the absorption. For relatively small wavelengths in particular, like the scintillation light of xenon, the top layer, including the anti-reflective coating, should be kept small in order to reduce absorption losses in the inactive parts of the SiPM.

The probability P_{trig} of an electron-hole pair to trigger an avalanche combines both probabilities of the electron and the hole to trigger the avalanche. The resulting total probability is thus given by [57]:

$$P_{\text{trig}}(\Delta U) = P^{\text{e}}_{\text{trig}} + P^{\text{h}}_{\text{trig}} - P^{\text{e}}_{\text{trig}} \cdot P^{\text{h}}_{\text{trig}} \tag{5.5}$$

where the last term accounts for the case of an avalanche triggered by both the electron and the hole. The probabilities to initiate an avalanche are dependent on the type of charge carrier and on the overvoltage [85]:

$$P^{\text{e}}_{\text{trig}}(\Delta U) = P^{\text{e,max}}_{\text{trig}}\left(1 - \text{e}^{-k\cdot\Delta U}\right) \qquad P^{\text{h}}_{\text{trig}}(\Delta U) = m \cdot \Delta U \tag{5.6}$$

where k and m are material-dependent coefficients. The probability for electrons saturates for large overvoltages, whereas the one for holes increases linearly. Given the larger ionisation rate of electrons, $P^{\text{e,max}}_{\text{trig}} > P^{\text{h,max}}_{\text{trig}}$ holds [57]. Furthermore, the trigger probabilities for electrons and holes strongly depend on the position where the electron-hole pair is created (see [57]). Therefore, besides a preferably high overvoltage, the design of a SiPM should be optimised in a way that the absorption of photons of a specific wavelength occurs dominantly on the p^+ side of the avalanche region where $P^{\text{e}}_{\text{trig}}$ is at maximum.

5.1.2 Experimental Procedure

Based on equation (5.1), the PDE is determined with the setup that was introduced in chapter 2. The source emits α-particles that propagate through gaseous xenon (GXe). On their trajectory, the α-particles deposit energy resulting in the isotropic emission of photons with a wavelength of 175 nm (see section 1.2.2). These photons may impinge on the SiPM and may be detected. As shown above, the ratio of these numbers yields the PDE.

Since the number of impinging photons on the SiPM is not known, there is a Photomultiplier Tube (PMT) as a reference detector with a known detection efficiency (DE) (see section 2.2.1). Both detectors are operated simultaneously and the acquisition of waveforms is triggered by the PMT. This is done because of its larger active area. Virtually every α-particle causes photon events on the PMT, which is not true for the SiPM. Since correlated avalanches are negligible for PMTs, the number of avalanches $N^{\text{PMT}}_{\text{det}}$ equals the number of detected photons $N^{\text{PMT}}_{\gamma} = N^{\text{PMT}}_{\text{det}}$. By determining this number, the number of impinging photons $N^{\text{PMT}}_{\text{tot}}$ is deduced:

$$N^{\text{PMT}}_{\text{tot}} = \frac{N^{\text{PMT}}_{\gamma}}{DE} \tag{5.7}$$

The number of impinging photons normalised to the total area A_{PMT} yields the flux Φ^{PMT} on the PMT. A first-order assumption is an equal flux on both detectors, i.e. $\Phi^{\text{PMT}} = \Phi^{\text{SiPM}}$. This subsequently yields the number of impinging photons $N^{\text{SiPM}}_{\text{tot}}$ on the SiPM as:

$$N^{\text{SiPM}}_{\text{tot}} = N^{\text{PMT}}_{\text{tot}} \cdot \frac{A_{\text{SiPM}}}{A_{\text{PMT}}} \tag{5.8}$$

The number of detected avalanches $N^{\text{SiPM}}_{\text{det}}$ on the SiPM is measured by rescaling the charge deposited in a pulse by the gain. In this analysis, the charge of a pulse is better suited than the

pulse height, since many avalanches superimpose within a short time. Besides the avalanches caused by photons, avalanches due to optical crosstalk (CT) and afterpulsing (AP) have to be taken into account, whereas the contribution due to thermal noise is typically negligible at cryogenic temperatures. Thus, the resulting signal may be distorted by these effects as is shown in figure 4.10. Not considering these effects, the resulting PDE will be overestimated. By determining the influences of these effects by measurements in the absence of light, as was discussed in chapter 4, these effects are taken into account. Thus, the number of detected photons N_γ^{SiPM} is obtained by rescaling the number of avalanches by the mean charge influence by both CT and AP on a single avalanche P_{CA}:

$$N_\gamma^{\mathrm{SiPM}} = \frac{N_{\mathrm{det}}^{\mathrm{SiPM}}}{1 + P_{\mathrm{CA}}} \tag{5.9}$$

5.1.3 Simulation

In order to understand the processes that occur in the setup in more detail, a GEANT4 based simulation in combination with the NEST Add-On [86] was developed within in the group [84]. It describes the Xenon Cell, where the source emits α-particles, that lose energy on their trajectories through the surrounding GXe or LXe. The emitted energy is partially converted to photons in the UV range. The photons are emitted isotropically and may reach the detectors where they are counted. The impinging photons are counted regardless of their direction, i.e. reflections on the detectors' surfaces are not taken into account. The main focus of the simulation is set on examining the impact of several parameters like for example the positions and heights of the PMT and the SiPM, the pressure, corresponding to a certain density, as well as the reflectivity coefficients of both the Cu wall and the Al holder of the source. Furthermore, the influence of the extended source (see chapter 2) as well as the range of the α-particles is investigated, which cannot be neglected for GXe in particular.

Considering these factors, the simulation disproves the former assumption of equal fluxes on both detectors. Using the simulation, a correction factor R can be calculated that accounts for the flux ratio on both detectors:

$$R = \left(\frac{\Phi^{\mathrm{SiPM}}}{\Phi^{\mathrm{PMT}}} \right)_{\mathrm{Sim}} \tag{5.10}$$

Since the reflectivity coefficients of our Cu and Al surfaces are not known, R is calculated by averaging the values of R_{ij} corresponding to different pairs of reflectivity coefficients of Cu and Al. It is re-calculated for each pressure and positioning. The determination of R is discussed in detail in [84]. Using R, the initial assumption of equal fluxes can be rewritten as:

$$\Phi^{\mathrm{SiPM}} = R \cdot \Phi^{\mathrm{PMT}} \tag{5.11}$$

Simulations suggest a correction factor for the specific setup of $R = 0.91 \pm 0.30$ for a pressure of 0.8 bar, $R = 0.86 \pm 0.20$ for a pressure of 1.0 bar and $R = 0.84 \pm 0.20$ for a pressure of 1.25 bar.

Another aspect, that mainly occurs in GXe, results from the extended range of the α-particles, which is in the order of cm (see chapter 2). If an α-particle propagates towards the SiPM, more

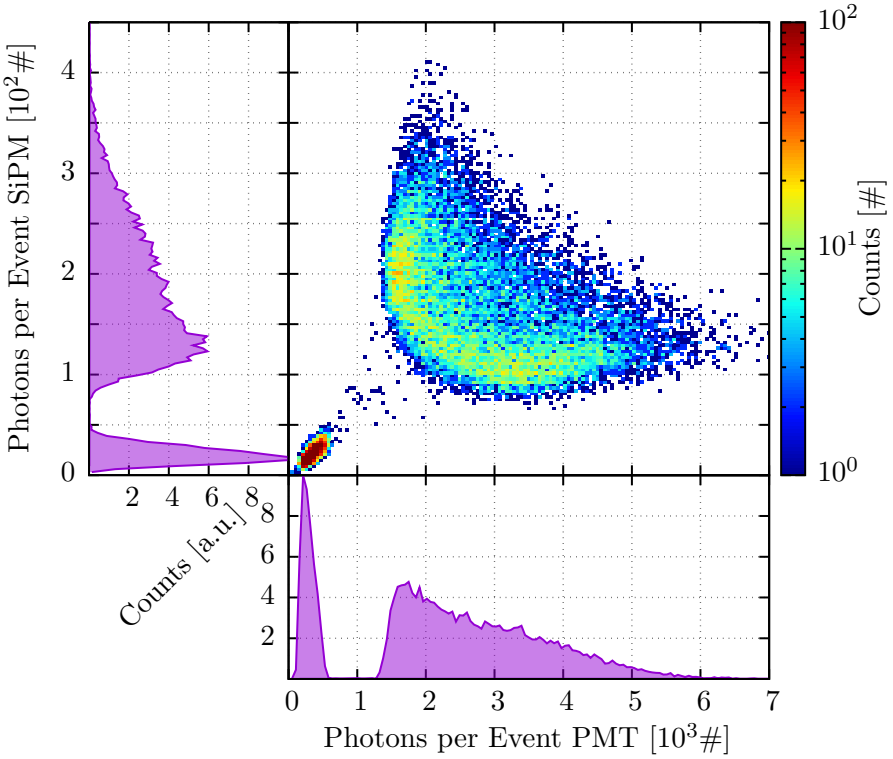

Figure 5.1: The main panel shows the number of photons per event on the SiPM in dependency of the number on the PMT. The abundance is denoted by colour and the different features are discussed in the text. The bottom and the left panel show projections of the data in the main panel to each axis. For clarity, both distributions are normalised to a peak value of 10. The number of photons on the PMT is significantly larger than the one on the SiPM, because of the larger area of the detector. The data was provided by Reimund Bayerlein and contains 25 000 α-events in GXe at a pressure of 1.0 bar and at reflectivity coefficients of 0.0 for both Cu and Al.

photons will impinge on the SiPM, than in the case where the α-particle propagates towards the PMT, and vice versa. This correlation of the distribution of the number of impinging photons is reproduced by the simulation as is shown in figure 5.1 for reflectivity coefficients of 0.0 and for a density corresponding to a pressure of 1.0 bar. Furthermore, the projections to each axis are shown. The cluster at low photon numbers on both the SiPM and the PMT is caused by α-particles propagating towards the Al holder. Since these α-particles are absorbed in the holder before depositing the majority of their energy, a lower total number of photons is emitted and impinges on the detectors. Due to the extension of the source, the length of the trajectories of the α-particles, and subsequently the total number of emitted photons depend on the origin of the particles and, therefore, varies slightly.

The PDE measurements were conducted at pressures of 0.8 bar, 1.0 bar and 1.25 bar. Therefore, the simulation was performed at the densities corresponding to these pressures as well. Due to a higher density of xenon atoms at higher pressure, the range of α-particles decreases

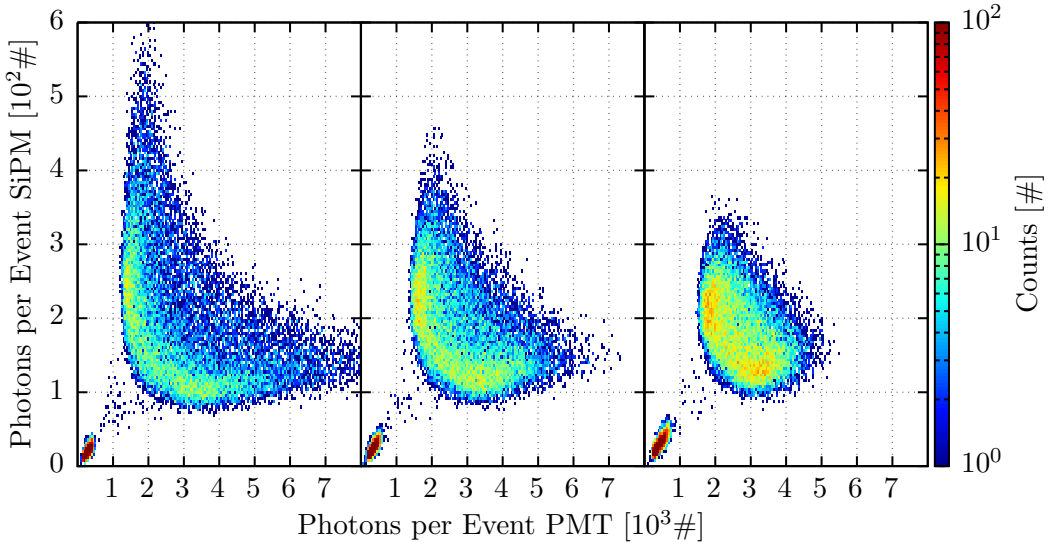

Figure 5.2: Each panel shows the number of photons per event on the SiPM in dependency of the number on the PMT. The abundance is denoted by colour. The data was provided by Reimund Bayerlein and each plot contains 25 000 α-events in GXe at pressures of 0.8 bar (left), 1.0 bar (middle) and 1.25 bar (right). The reflectivity coefficients are 0.0 for both Cu and Al. The distributions show a more distinct correlation for lower densities corresponding to lower pressures, that result from the lower range of the α-particles.

with increasing density. Thus, the distribution of the number of impinging photons on the PMT and on the SiPM, as was shown above, depends on the density as well. α-particles with a larger range will propagate closer towards a specific detector which is why the resulting distribution is more anti-correlated. On the other hand, a higher density results in a reduction of this feature. The distributions for each pressure are shown in figure 5.2 for reflectivity coefficients of 0.0.

5.1.4 Results

As indicated above, the measurements for the calculation of the PDE were conducted at pressures of 0.8 bar, 1.0 bar and 1.25 bar at temperatures of −105 °C, −105 °C and −100 °C, respectively. The reasons why the temperature was altered for the third run will be discussed in the next section (see section 5.2). The data was taken for bias voltages of −25.5 V to −30.0 V in steps of 0.5 V for the SiPM for each pressure. The PMT was operated at a bias voltage of 800 V. The data was acquired by triggering on the PMT signal and then storing the signals of both PMT and SiPM. The resulting waveforms are analysed with the integration algorithm discussed in section 3.2.1. The resulting charge values could not be converted to photoelectron equivalent (p.e.) as will be discussed in section 5.2. Instead, the numbers of photons are given in charge equivalents.

The depiction of the simulated data shown above is shown in figure 5.3 for measured data at a pressure of 0.8 bar and for a bias voltage of −28 V. The specific correlation of the distribution predicted by the simulation is reproduced by the measurement, whereas the distribution is

blurred compared to the simulated data. Possible reasons for this are, for example, the unknown reflectivity coefficients of Cu and Al in the Xenon Cell. Furthermore, the DE and the PDE of PMT and SiPM as well as the losses due to reflection on the detectors' surfaces, that are not considered by the simulation, might have an effect. A comparison of the distributions at constant bias voltage for different pressures is shown in figure 5.4. The intensity of the cluster at low photon numbers at a pressure of 1.0 bar is significantly reduced compared to the one at a pressure of 0.8 bar. The observation indicates a partial liquefaction of the xenon, since the range of α-particles in LXe is in the order of µm, due to the larger density. Therefore, most of the α-particles do not reach the Al holder but rather deposit their total energy in the xenon. Another difference is the slight shift of the cluster at larger photon numbers towards lower photon numbers. Due to the increased density of LXe, the stopping power is increased. Thus, a part of the photons is emitted near the α-source yielding a decreased solid angle to the detectors. Furthermore, the longer path of the photons results in a higher absorption probability by impurities in the remaining GXe. On the other hand, the light yield in LXe is larger than in GXe, resulting in an increased total number of emitted photons (see section 1.2.2 and section 2.1). The measurement at 1.25 bar is hardly comparable to the other ones due to both different pressure and different temperature.

Combining all considerations from the previous section in this chapter, the final equation for calculating the PDE is:

$$PDE = \frac{A_{\mathrm{PMT}}}{A_{\mathrm{SiPM}}} \cdot \frac{N_{\gamma}^{\mathrm{SiPM}}}{N_{\gamma}^{\mathrm{PMT}}} \cdot DE \cdot \frac{1}{1 + P_{\mathrm{CA}}} \cdot \frac{1}{R} \tag{5.12}$$

where $N_{\gamma}^{\mathrm{SiPM}}$ denotes the number of detected photons corrected for both CT and AP. The PDE is not corrected for avalanches due to thermal excitation, since their influence is negligible. The area ratio and the DE of the PMT are fixed values, whereas the ratio of detected photons is measured. CT and AP are deduced from measurements in the absence of light resulting in P_{CA}, R results from the simulation. Since the gain of both the PMT and the SiPM could not be derived in supplementary dark measurements, as will be discussed in the next section (see section 5.2), the PDE could not finally be derived. The PDE is expected to increase with increasing overvoltage, i.e. bias voltage. This is shown qualitatively in figure 5.5, where the distribution of charge equivalent detected by the SiPM is shown as a function of the bias voltage. The mean values of these distributions are shown in figure 5.6 together with the mean values of the corresponding distributions of the PMT. As expected, the mean values of the PMT do not vary significantly. On the other hand, the mean charge equivalent detected by the SiPM increases with increasing bias voltage. Besides the expected increase of the PDE, this is due to both increasing gain and increasing optical crosstalk (CT) probability as well.

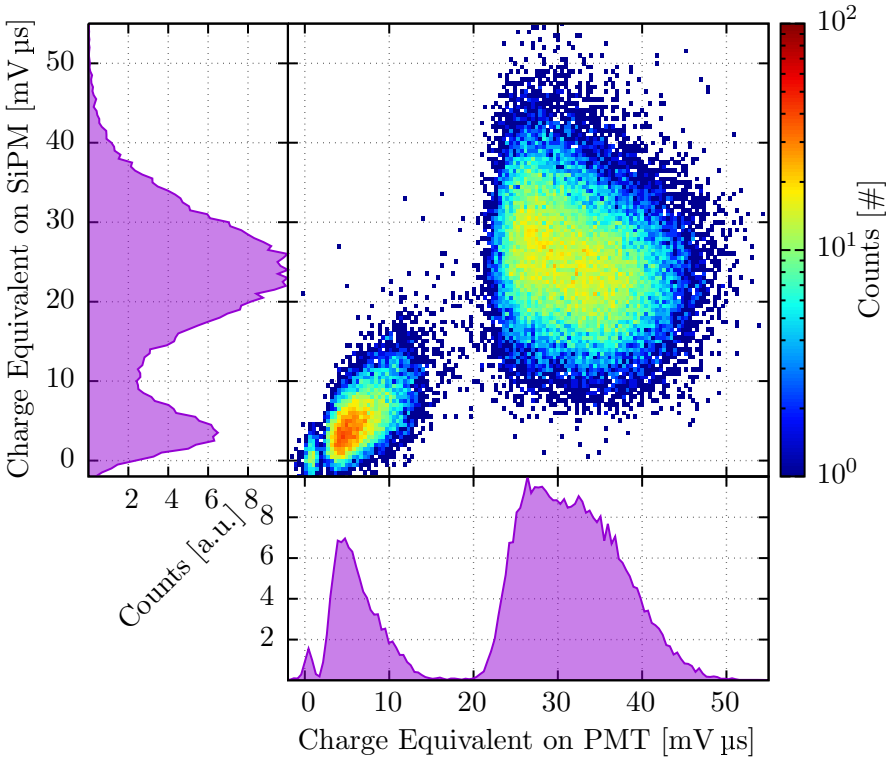

Figure 5.3: The main panel shows the charge equivalent per event detected by the SiPM in dependency of the charge equivalent detected by the PMT. The abundance is denoted by colour and is normalised to 25 000 events to simplify a comparison to the simulation. The different features of the figure are discussed in the text. The bottom and left panel show projections of the data in the main panel to each axis. For clarity, both distributions are normalised to a peak value of 10. The data shown results from a measurement conducted at a pressure of 0.8 bar at a bias voltage of −28 V for the SiPM.

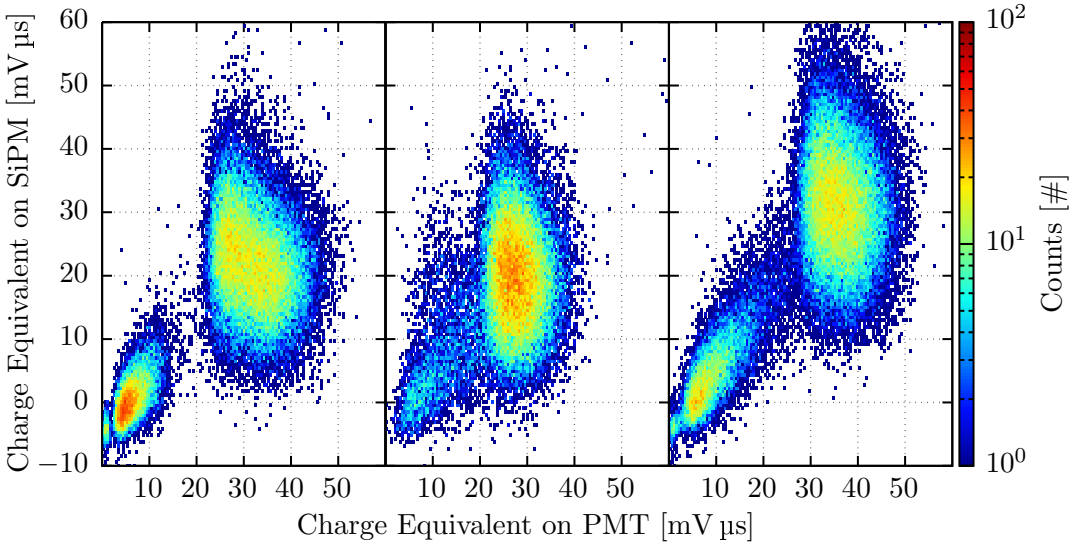

Figure 5.4: Each panel shows the charge equivalent per event detected by the SiPM in dependency of the charge equivalent detected by the PMT. The abundance is denoted by colour and is normalised to 25 000 events to simplify a comparison to the simulation. The data shown results from measurements conducted at a bias voltage of −28 V and at pressures of 0.8 bar (left), 1.0 bar (middle) and 1.25 bar (right). The figure is discussed in detail in the text.

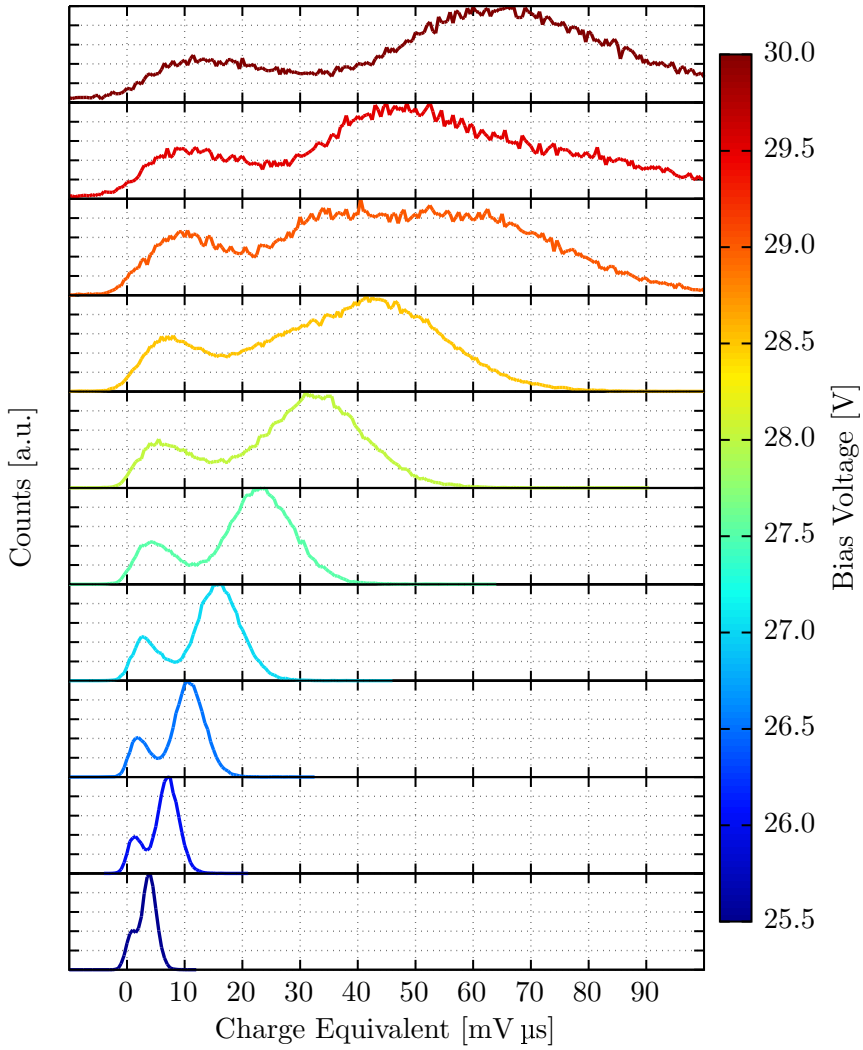

Figure 5.5: The charge equivalent detected by the SiPM is shown as a function of the bias voltage at a xenon pressure of 1.25 bar. The bias voltage is denoted by colour and the distributions are normalised to fit the associated panel. As discussed in the text in more detail, the distributions move towards larger charge equivalents with increasing bias voltage.

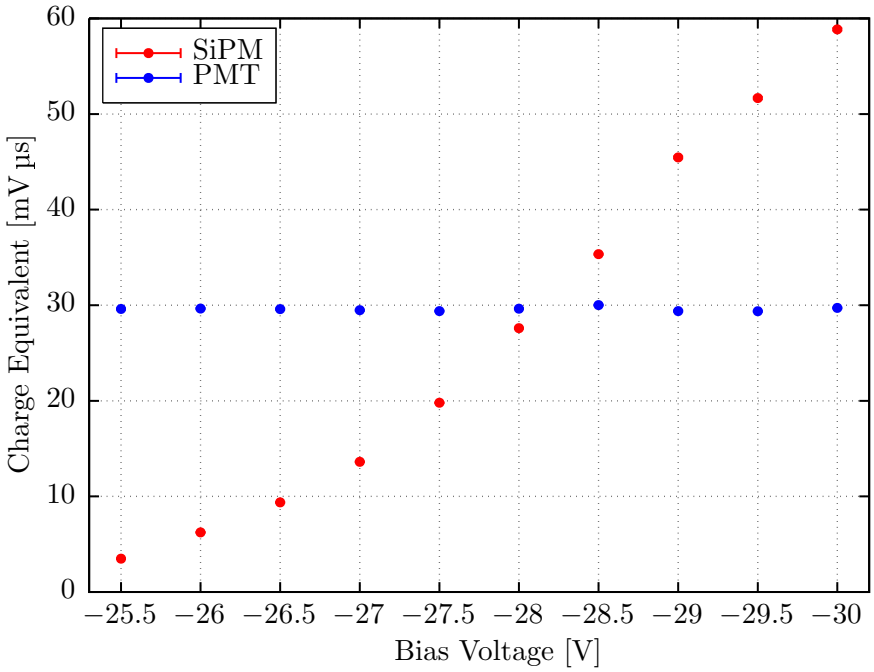

Figure 5.6: The mean charge equivalent detected by SiPM and by PMT are shown as a function of the bias voltage of the SiPM. The data results from measurements at a xenon pressure of 1.25 bar. The mean values result from averaging the distributions shown in figure 5.5 for the SiPM and analogously for the PMT. The observed trends are discussed in the text.

5.2 Limitations

The simulation of the Xenon Cell assumes perfectly pure xenon through which the photons propagate. In reality, in addition to any initial impurification of the xenon, impurities from the walls of the Xenon Cell accumulate over time. The impurities may absorb some of the xenon scintillation light, resulting in a decreased number of photons reaching the detectors. Due to the geometry of the setup, the travel distance of photons from the source to both detectors is different. This results in different absorption probabilities for photons impinging on the detectors, which has to be accounted for in the simulation and when calculating the flux ratio. The expected trend of the decreasing number of detected photons with time is reproduced as is shown in figure 5.7 for measurements with the PMT at 0.8 bar. On the other hand, the measurements at 1.0 bar show an increasing number of photons with time indicating a reduction of impurification. This might be explained by the fact that the α-source was covered with a thin layer of LXe as was discussed above. Since this was the only modified parameter, the observed trend indicates a better attachment of impurities in LXe than in GXe, resulting in a de facto purification of the remaining GXe. The measurements at 1.25 bar were taken at $-100\,^{\circ}\mathrm{C}$, where xenon is gaseous. Before warming up, the Xenon Cell was filled with additional xenon which was released during heating. These changes of the parameters leave the number of detected photons incomparable to the numbers resulting from previous measurements. Besides, the variation of the number of photons in the measurements at 1.25 bar is rather small. Therefore, these measurements would fit best for determining the PDE.

Another limitation of examining the PDE occurred in measurements in the absence of light. The performance of the device rendered a determination of the gain and of the CT impossible, since on the one hand, single photoelectron equivalents (p.e.s) could not be resolved. On the other hand, the device exhibited inverse pulses as well as rectangular pulses (see figure 5.8) which cannot be explained. Although some pulses appear to be genuine, they always occur with the same amplitude which is significantly larger than similar pulses of other devices and without revealing the quantised nature of the SiPM's response. Furthermore, these pulses are quite long compared to the ones of the other device tested (see chapter 3). Not knowing the gain, the charge equivalents deposited during the PDE measurements by scintillation light of xenon could not be converted to p.e.s which is why the number of photons could not be counted. Concluding from the observed features, this device does not seem to be well-suited for an application in the nEXO experiment, which is confirmed by measurements of collaborators as well.

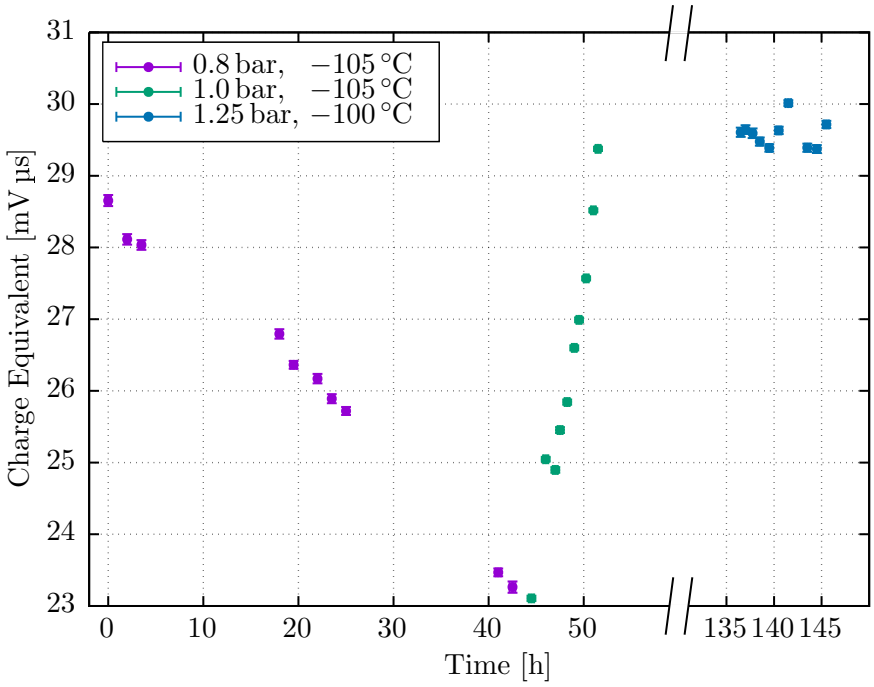

Figure 5.7: The mean charge equivalent detected by the PMT is shown as a function of time for various xenon pressures. The time is given relative to the first measurement. Its uncertainties result from considering the length of a measurement as well as a time measurement accuracy of 15 min. The trends are discussed in the text.

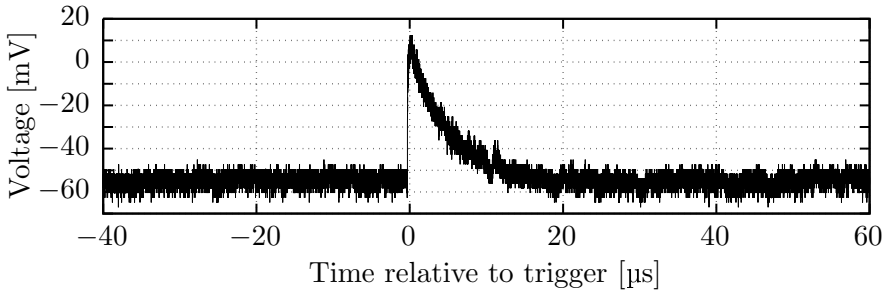

(a)

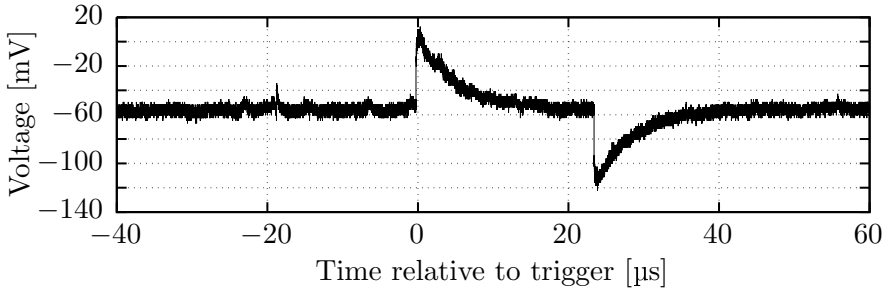

(b)

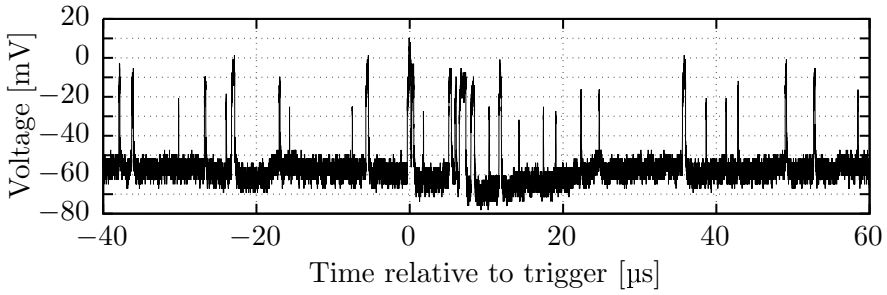

(c)

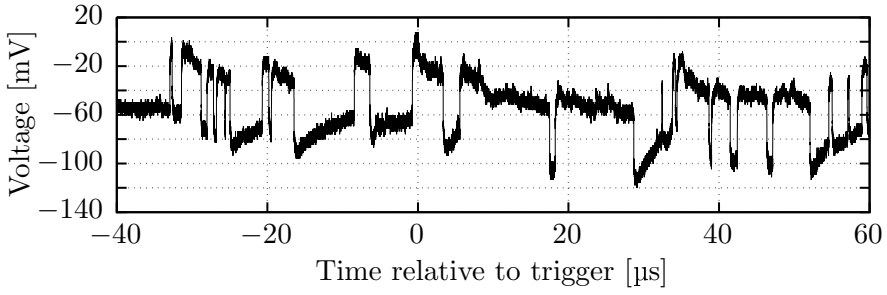

(d)

Figure 5.8: Several waveforms measured with the device. **(a)** shows a pulse that appears as expected. The discussion why even these pulses are peculiar is given in the text. **(b) - (d)** show waveforms possessing inverse pulses, fractions of pulses or erratic spikes. This behaviour cannot be explained and prevents a determination of the gain and hence a quantitative examination of the PDE.

Conclusion and Outlook

Within the scope of this thesis, several aspects concerning the R&D phase of Silicon Photomultipliers (SiPMs) in Erlangen for the future nEXO experiments were addressed. Given the recent formation of the work group, fundamental work had to be done on a variety of topics. These include, among others, designing a preamplification board and a corresponding construction that is compatible with different SiPMs. The latest design offers a mechanically stable way of operation while at the same time having an in situ amplification at cryogenic temperatures.

The main focus of this thesis was laid on the development of a C++ and ROOT based software for analysing SiPM data. In consultation with colleagues and in cooperation with collaborators, a modularised software was developed that can process data originating from different apparatuses. Additional apparatuses can be added in an easy way, without affecting the later analyses of the data. For the subsequent analysis of waveforms, three algorithms were developed, each suiting a different purpose. The algorithm that integrates pulses is best suited for photon detection efficiency (PDE) measurements due to many superimposed pulses. On the downside, it is not able to separate individual pulses as is required for advanced analyses of measurements in the absence of light. Measurements at dark condition are best analysed with either the peak finder algorithm or, better yet, the pulse fitting algorithm. Both algorithms can separate multiple pulses within a single waveform and yield the peak height corresponding to each pulse. Using these algorithms, several characteristics become accessible for investigation that could not be derived otherwise. However, more work is necessary to fine-tune certain parameters of the pulse fitting algorithm in particular, in order to enhance its accuracy and time resolution. Based on the analysis of waveforms, many characteristics of a SiPM can be derived. Therefore, a framework was designed within the software containing several algorithms that determine the physical parameters of a SiPM.

The characterisation of a SiPM of the type VUV-HD LF 2016 by FBK was performed successfully in the absence of light at cryogenic temperatures of $-105\,^{\circ}\mathrm{C}$ corresponding to the temperature in the nEXO experiment. Several characteristics of the device were examined, even beyond those that are necessary for the nEXO experiment. Some of the SiPM's characteristics meet the limits posed by the nEXO experiment even at high overvoltages, like for example the dark count rate. Others exceed these limits already at low overvoltages, like for example the optical crosstalk probability. The measured probability for afterpulsing is clearly larger than stated by the manufacturer [83], so complementary measurements by collaborators as well as a revision of the corresponding algorithms are necessary to resolve this discrepancy. Due to unidentified reasons, the device tested at dark condition did not work properly anymore after those measurements, which is why a measurement of the PDE was not possible. Measurements by collaborators indicate a PDE of about 20 % at overvoltages above 4 V for these devices which meets the requirements posed by the nEXO experiment on this parameter.

The scintillation light of xenon was measured with a SiPM of the type VUV-HD STD 2016 by FBK in coincidence with a PMT serving as reference detector. This setup was used to examine the PDE of the SiPM. Due to limitations in resolving individual photoelectron equivalents, the gain could not be determined, which prevented a quantitative analysis of the PDE. Furthermore, impurities are accumulated in xenon over time, reducing the mean number of detected photons. This feature could be limited by a continuous purification of the xenon, which is already planned. However, besides these issues, several aspects that have been predicted by a GEANT4 based simulation [84] could be reproduced by measurements. This fact is promising for further measurements in the Erlangen setup. On the downside, this type of device does not seem to be suited for the nEXO experiment. This evaluation is confirmed by measurements of collaborators as well.

The next steps concerning the Erlangen setup used for characterising UV-sensitive SiPMs for the nEXO experiment will dominantly entail the extension to work with liquid xenon instead of gaseous xenon. This measure allows for characterisations of SiPMs under more realistic conditions. In addition, more work on an automatised binary data taking software including temperature, pressure and data monitoring is necessary in order to increase convenience and to accelerate measurements. In the more distant future, the main focus of the R&D phase concerning the photodetectors for the nEXO experiment will be the characterisation of larger arrays of SiPMs consisting of several devices. As an overall goal, the Erlangen group tries to play an active role in the R&D phase and the future nEXO experiment, which aims to push the search for the neutrinoless double beta decay to new frontiers.

Appendix A

List of Abbreviations

$0\nu\beta\beta$ **decay**	neutrinoless double beta decay
$2\nu\beta\beta$ **decay**	double beta decay
AP	afterpulsing
APD	Avalanche Photo Diode
CE	collection efficiency
CT	optical crosstalk
DE	detection efficiency
DCR	dark count rate
GM-APD	Geiger-Mode Avalanche Photodiode
GND	ground
GXe	gaseous xenon
HFE	1-methoxyheptafluoropropane C3F7OCH3
LN	liquid nitrogen
LXe	liquid xenon
MS event	multi site event
NME	nuclear matrix element
PCB	printed circuit board
PDE	photon detection efficiency
p.e.	photoelectron equivalent
PMT	Photomultiplier Tube
PTFE	Polytetrafluoroethylene
QE	quantum efficiency
ROI	region of interest
R&D	research and development
SiPM	Silicon Photomultiplier
SPAD	Single Photon Avalanche Photodiode
SS event	single site event
TPC	time projection chamber

Appendix B

List of Figures

Appendix C

List of Tables

Appendix D

Bibliography

[1] C. L. Cowan et al. "Detection of the Free Neutrino: a Confirmation". In: *Science* 124.3212 (1956), pp. 103–104. DOI: 10.1126/science.124.3212.103.

[2] Y. Fukuda et al. "Evidence for Oscillation of Atmospheric Neutrinos". In: *Phys. Rev. Lett.* 81 (8 1998), pp. 1562–1567. DOI: 10.1103/PhysRevLett.81.1562.

[3] Q. R. Ahmad et al. "Measurement of the Rate of $\nu_e + d \rightarrow p + p + e^-$ Interactions Produced by ^8B Solar Neutrinos at the Sudbury Neutrino Observatory". In: *Phys. Rev. Lett.* 87 (7 2001), p. 071301. DOI: 10.1103/PhysRevLett.87.071301.

[4] E. Majorana. "Teoria simmetrica dell elettrone e del positrone". Italian. In: *Il Nuovo Cimento* 14.4 (1937), pp. 171–184. DOI: 10.1007/BF02961314.

[5] C. F. v. Weizsäcker. "Zur Theorie der Kernmassen". In: *Zeitschrift für Physik* 96.7 (1935), pp. 431–458. DOI: 10.1007/BF01337700.

[6] L. Maiani. "Selected Topics in Majorana Neutrino Physics". In: *Riv. Nuovo Cim.* 37.08 (2014), pp. 417–466. DOI: 10.1393/ncr/i2014-10103-9.

[7] M. Goeppert-Mayer. "Double Beta-Disintegration". In: *Phys. Rev.* 48 (6 1935), pp. 512–516. DOI: 10.1103/PhysRev.48.512.

[8] S. R. Elliott, A. A. Hahn, and M. K. Moe. "Direct evidence for two-neutrino double-beta decay in ^{82}Se". In: *Phys. Rev. Lett.* 59 (18 1987), pp. 2020–2023. DOI: 10.1103/PhysRevLett.59.2020.

[9] W. Rodejohann. "Neutrino-less Double Beta Decay and Particle Physics". In: *Int. J. Mod. Phys.* E20 (2011), pp. 1833–1930. DOI: 10.1142/S0218301311020186.

[10] H. V. Klapdor-Kleingrothaus. "First Evidence for Lepton Number Violation and the Majorana Character of Neutrinos". In: *The Identification of Dark Matter*. 2005, pp. 633–646. DOI: 10.1142/9789812701848_0094.

[11] C. E. Aalseth et al. "Comment on 'Evidence for neutrinoless double beta decay'". In: *Mod. Phys. Lett.* A17 (2002), pp. 1475–1478. DOI: 10.1142/S0217732302007715.

[12] Q. R. Ahmad et al. "Direct Evidence for Neutrino Flavor Transformation from Neutral-Current Interactions in the Sudbury Neutrino Observatory". In: *Phys. Rev. Lett.* 89 (1 2002), p. 011301. DOI: 10.1103/PhysRevLett.89.011301.

[13] M. Doi, T. Kotani, and E. Takasugi. "Double Beta Decay and Majorana Neutrino". In: *Progress of Theoretical Physics Supplement* 83 (1985), pp. 1–175. DOI: 10.1143/PTPS.83.1.

[14] J. J. Gomez-Cadenas et al. "The Search for neutrinoless double beta decay". In: *Riv. Nuovo Cim.* 35 (2012), pp. 29–98. DOI: 10.1393/ncr/i2012-10074-9.

[15] A. Escuderos et al. "Contributions of different neutron pairs in different approaches for neutrinoless double beta decay". In: *J. Phys.* G37 (2010), p. 125108. DOI: 10.1088/0954-3899/37/12/125108.

[16] F. Šimkovic, M. I. Krivoruchenko, and A. Faessler. "Neutrinoless double-beta decay and double-electron capture". In: *Prog. Part. Nucl. Phys.* 66 (2011), pp. 446–451. DOI: 10.1016/j.ppnp.2011.01.049.

[17] X. Qian and P. Vogel. "Neutrino Mass Hierarchy". In: *Prog. Part. Nucl. Phys.* 83 (2015), pp. 1–30. DOI: 10.1016/j.ppnp.2015.05.002.

[18] J. Schechter and J. W. F. Valle. "Neutrinoless double-β decay in SU(2)×U(1) theories". In: *Phys. Rev. D* 25 (11 1982), pp. 2951–2954. DOI: 10.1103/PhysRevD.25.2951.

[19] J. Gómez-Cadenas et al. "Sense and sensitivity of double beta decay experiments". In: *Journal of Cosmology and Astroparticle Physics* 2011.06 (2011), p. 007.

[20] J. Meija et al. "Isotopic compositions of the elements 2013 (IUPAC Technical Report)". In: *Pure and Applied Chemistry* 88 (3 2016), pp. 293–306. DOI: 10.1515/pac-2015-0503.

[21] S. Umehara et al. "Neutrino-less double-beta decay of Ca-48 studied by Ca F(2)(Eu) scintillators". In: *Phys. Rev.* C78 (2008), p. 058501. DOI: 10.1103/PhysRevC.78.058501.

[22] M. Agostini et al. "Search of Neutrinoless Double Beta Decay with the GERDA Experiment". In: *Nuclear and Particle Physics Proceedings* 273–275 (2016). 37th International Conference on High Energy Physics (ICHEP), pp. 1876–1882. DOI: 10.1016/j.nuclphysbps.2015.09.303.

[23] A. S. Barabash and V. B. Brudanin. "Investigation of double beta decay with the NEMO-3 detector". In: *Phys. Atom. Nucl.* 74 (2011), pp. 312–317. DOI: 10.1134/S1063778811020062.

[24] R. Arnold et al. "Technical design and performance of the NEMO 3 detector". In: *Nucl. Instrum. Meth.* A536 (2005), pp. 79–122. DOI: 10.1016/j.nima.2004.07.194.

[25] F. A. Danevich et al. "Search for 2 beta decay of cadmium and tungsten isotopes: Final results of the Solotvina experiment". In: *Phys. Rev.* C68 (2003), p. 035501. DOI: 10.1103/PhysRevC.68.035501.

[26] C. Arnaboldi et al. "Results from a search for the 0 neutrino beta beta-decay of Te-130". In: *Phys. Rev.* C78 (2008), p. 035502. DOI: 10.1103/PhysRevC.78.035502.

[27] A. Gando et al. "Search for Majorana Neutrinos near the Inverted Mass Hierarchy Region with KamLAND-Zen". In: *Phys. Rev. Lett.* 117.8 (2016), p. 082503. DOI: 10.1103/PhysRevLett.117.082503.

[28] R. Arnold et al. "Measurement of the $2\nu\beta\beta$ decay half-life of ^{150}Nd and a search for $0\nu\beta\beta$ decay processes with the full exposure from the NEMO-3 detector". In: *Phys. Rev.* D94.7 (2016), p. 072003. DOI: 10.1103/PhysRevD.94.072003.

[29] D. R. Artusa et al. "Searching for neutrinoless double-beta decay of ^{130}Te with CUORE". In: *Adv. High Energy Phys.* 2015 (2015), p. 879871. DOI: 10.1155/2015/879871.

[30] K. Alfonso et al. "Search for Neutrinoless Double-Beta Decay of ^{130}Te with CUORE-0". In: *Phys. Rev. Lett.* 115.10 (2015), p. 102502. DOI: 10.1103/PhysRevLett.115.102502.

[31] M. Auger et al. "The EXO-200 detector, part I: Detector design and construction". In: *Journal of Instrumentation* 7 (2012), P05010. DOI: 10.1088/1748-0221/7/05/P05010.

[32] M. Auger et al. "Search for Neutrinoless Double-Beta Decay in ^{136}Xe with EXO-200". In: *Phys. Rev. Lett.* 109 (2012), p. 032505. DOI: 10.1103/PhysRevLett.109.032505.

[33] J. B. Albert et al. "Search for Majorana neutrinos with the first two years of EXO-200 data". In: *Nature* 510 (2014), pp. 229–234. DOI: 10.1038/nature13432.

[34] M. Agostini et al. "Results on Neutrinoless Double-β Decay of Ge76 from Phase I of the GERDA Experiment". In: *Phys. Rev. Lett.* 111.12, 122503 (2013), p. 122503. DOI: 10.1103/PhysRevLett.111.122503.

[35] K. Asakura et al. "Results from KamLAND-Zen". In: *AIP Conf. Proc.* 1666 (2015), p. 170003. DOI: 10.1063/1.4915593.

[36] A. Gando et al. "Limit on Neutrinoless $\beta\beta$ Decay of ^{136}Xe from the First Phase of KamLAND-Zen and Comparison with the Positive Claim in ^{76}Ge". In: *Phys. Rev. Lett.* 110 (6 2013), p. 062502. DOI: 10.1103/PhysRevLett.110.062502.

[37] R. Arnold et al. "Search for neutrinoless double-beta decay of ^{100}Mo with the NEMO-3 detector". In: *Phys. Rev.* D89.11 (2014), p. 111101. DOI: 10.1103/PhysRevD.89.111101.

[38] R. Arnold et al. "First Results of the Search for Neutrinoless Double-Beta Decay with the NEMO 3 Detector". In: *Phys. Rev. Lett.* 95 (18 2005), p. 182302. DOI: 10.1103/PhysRevLett.95.182302.

[39] J. Argyriades et al. "Measurement of the Double Beta Decay Half-life of Nd-150 and Search for Neutrinoless Decay Modes with the NEMO-3 Detector". In: *Phys. Rev.* C80 (2009), p. 032501. DOI: 10.1103/PhysRevC.80.032501.

[40] J. Martín-Albo et al. "Sensitivity of NEXT-100 to neutrinoless double beta decay". In: *Journal of High Energy Physics* 2016.5 (2016), p. 159. DOI: 10.1007/JHEP05(2016)159.

[41] J. J. Gomez-Cadenas et al. "Present status and future perspectives of the NEXT experiment". In: *Adv. High Energy Phys.* 2014 (2014), p. 907067. DOI: 10.1155/2014/907067.

[42] *SNOLAB*. 2016. URL: https://www.snolab.ca/.

[43] *3M™ Novec™ HFE-7000*. 2016. URL: http://www.3m.com/.

[44] L. Yang. "Status and prospects for the EXO-200 and nEXO experiments". In: http://neutrino2016.iopconfs.org/IOP/media/uploaded/EVIOP/event_948/10.05__5__Yang.pdf, 2016.

[45] E. Aprile and T. Doke. "Liquid xenon detectors for particle physics and astrophysics". In: *Rev. Mod. Phys.* 82 (3 2010), pp. 2053–2097. DOI: 10.1103/RevModPhys.82.2053.

[46] J. Jortner et al. "Localized Excitations in Condensed Ne, Ar, Kr, and Xe". In: *The Journal of Chemical Physics* 42.12 (1965), pp. 4250–4253. DOI: 10.1063/1.1695927.

[47] B. Mong et al. "Spectroscopy of Ba and Ba^+ deposits in solid xenon for barium tagging in nEXO". In: *Phys. Rev. A* 91 (2 2015), p. 022505. DOI: 10.1103/PhysRevA.91.022505.

[48] P. A. R. Ade et al. "Planck 2015 results. XIII. Cosmological parameters". In: *Astron. Astrophys.* 594 (2016), A13. DOI: 10.1051/0004-6361/201525830.

[49] D. Renker and E. Lorenz. "Advances in solid state photon detectors". In: *Journal of Instrumentation* 4.04 (2009), P04004.

[50] K. A. Tadday. "Scintillation Light Detection and Application of Silicon Photomultipliers in Imaging Calorimetry and Positron Emission Tomography". PhD thesis. Ruperto-Carola-Universität Heidelberg, 2011.

[51] B. F. Aull et al. "Geiger-mode avalanche photodiodes for three-dimensional imaging". In: *Lincoln Laboratory Journal* (2002), pp. 335–350.

[52] R. H. Haitz. "Model for the Electrical Behavior of a Microplasma". In: *Journal of Applied Physics* 35.5 (1964), pp. 1370–1376. DOI: 10.1063/1.1713636.

[53] R. H. Haitz. "Mechanisms Contributing to the Noise Pulse Rate of Avalanche Diodes". In: *Journal of Applied Physics* 36.10 (1965), pp. 3123–3131. DOI: 10.1063/1.1702936.

[54] R. J. McIntyre. "Multiplication noise in uniform avalanche diodes". In: *IEEE Transactions on Electron Devices* ED-13.1 (1966), pp. 164–168. DOI: 10.1109/T-ED.1966.15651.

[55] R. J. McIntyre. "Theory of Microplasma Instability in Silicon". In: *Journal of Applied Physics* 32.6 (1961), pp. 983–995. DOI: 10.1063/1.1736199.

[56] H. Otono et al. "Study of the internal mechanisms of Pixelized Photon Detectors operated in Geiger-mode". In: *Submitted to: Nucl. Instrum. Meth.* (2008).

[57] N. Dinu. "Instrumentation on silicon detectors: from properties characterization to applications". PhD thesis. Université Paris Sud - Paris XI, 2013.

[58] *SensL White Paper from October 2015*. 2016. URL: http://sensl.com/downloads/ds/WP-Evaluate_and_Compare_SiPM.pdf.

[59] *SensL Technical Note from October 2012*. 2016. URL: http://www.sensl.com/downloads/ds/TN%20-%20Intro%20to%20SPM%20Tech.pdf.

[60] L. Fabris et al. "Concepts of SiPM readout electronics". In: *Workshop on large area, low background, VUV sensitive photo-detectors and associated electronics*. 2014.

[61] D. T. Pierce and W. E. Spicer. "Electronic Structure of Amorphous Si from Photoemission and Optical Studies". In: *Phys. Rev. B* 5 (8 1972), pp. 3017–3029. DOI: 10.1103/PhysRevB.5.3017.

[62] V. Solovov et al. "Measurement of the refractive index and attenuation length of liquid xenon for its scintillation light". In: *Nucl. Instrum. Meth. A* 516.2–3 (2004), pp. 462–474. DOI: 10.1016/j.nima.2003.08.117.

[63] I. Ostrovskiy et al. “Characterization of Silicon Photomultipliers for nEXO”. In: *IEEE Trans. Nucl. Sci.* 62.4 (2015), pp. 1825–1836. doi: 10.1109/TNS.2015.2453932.

[64] *ASTAR*. 2016. url: http://physics.nist.gov/PhysRefData/Star/Text/ASTAR.html.

[65] M. Miyajima, S. Sasaki, and E. Shibamura. “Absolute number of photons produced by alpha-particles in liquid and gaseous xenon”. In: *Nucl. Instrum. Meth. B* 63.3 (1992), pp. 297–308. doi: 10.1016/0168-583X(92)95113-6.

[66] K. Saito et al. “Absolute number of scintillation photons emitted by alpha-particles in rare gases”. In: *IEEE Trans. Nucl. Sci.* 49 (2002), pp. 1674–1680. doi: 10.1109/TNS.2002.801700.

[67] *WAVERUNNER® 6100A*. 2016. url: http://teledynelecroy.com/.

[68] *DRS4 Evaluation Board*. 2016. url: https://www.psi.ch/drs/drs-chip.

[69] *Photomultiplier Tube R8520-406*. 2016. url: https://www.hamamatsu.com/us/en/R8520-406.html.

[70] *EAGLE software*. 2016. url: https://cadsoft.io.

[71] *MMCX-J-P-H-ST-SM1 Mounts from SAMTEC*. 2016. url: https://www.samtec.com/products/mmcx-sm.

[72] *FBK*. 2016. url: https://srs.fbk.eu.

[73] M. Morháč et al. “Efficient one- and two-dimensional gold deconvolution and its application to γ-ray spectra decomposition”. In: *Nucl. Instrum. Meth. A* 401.2 (1997), pp. 385–408. doi: 10.1016/S0168-9002(97)01058-9.

[74] P. J. Naish and S. Hartwell. “Exponentially Modified Gaussian functions—A good model for chromatographic peaks in isocratic HPLC?” In: *Chromatographia* 26.1 (1988), pp. 285–296. doi: 10.1007/BF02268168.

[75] C. Rethmeier. “Characterization of VUV sensitive SiPMs for nEXO”. In: *Journal of Instrumentation* 11.03 (2016), p. C03002.

[76] A. L. Lacaita et al. “On the bremsstrahlung origin of hot-carrier-induced photons in silicon devices”. In: *IEEE Transactions on Electron Devices* 40.3 (1993), pp. 577–582. doi: 10.1109/16.199363.

[77] L. Gallego et al. “Modeling crosstalk in silicon photomultipliers”. In: *Journal of Instrumentation* 8.05 (2013), P05010.

[78] W. J. Kindt, H. W. van Zeijl, and S. Middelhoek. “Optical Cross Talk in Geiger Mode Avalanche Photodiode Arrays: Modeling, Prevention and Measurement”. In: *Solid-State Device Research Conference, 1998. Proceeding of the 28th European*. 1998, pp. 192–195.

[79] I. Rech et al. “Optical crosstalk in single photon avalanche diode arrays: a new complete model”. In: *Opt. Express* 16.12 (2008), pp. 8381–8394. doi: 10.1364/OE.16.008381.

[80] J. Schneider. “Charakterisierung von Siliziumphotomultipliern”. Bachelorarbeit. Friedrich-Alexander-Universität Erlangen-Nürnberg, 2015.

[81] Y. Du and F. Retière. “After-pulsing and cross-talk in multi-pixel photon counters”. In: *Nucl. Instrum. Meth. A* 596.3 (2008), pp. 396–401. DOI: 10.1016/j.nima.2008.08.130.

[82] A. Vacheret et al. “Characterization and Simulation of the Response of Multi Pixel Photon Counters to Low Light Levels”. In: *Nucl. Instrum. Meth.* A656.1 (2011), pp. 69–83. DOI: 10.1016/j.nima.2011.07.022.

[83] A. Gola et al. “Functional characterization of NUV-HD FBK Silicon Photomultipliers from 300 K to 40 K”. In: 2015.

[84] R. Bayerlein. “Simulation of Alpha Particle Scintillation Light in Liquid and Gaseous Xenon with Respect to Surface Reflections”. Master’s Thesis. Friedrich-Alexander-Universität Erlangen-Nürnberg, 2016.

[85] D. Orme et al. “Measurement of PDE of MPPC with different wavelengths of light”. In: *Proceedings of Science, International Workshop on New Photon Detectors (PD09)*. Vol. 19. 2009.

[86] M. Szydagis et al. “NEST: a comprehensive model for scintillation yield in liquid xenon”. In: *Journal of Instrumentation* 6.10 (2011), P10002.

Acknowledgements

I would like to thank the following persons, who supported me during the past months concerning this thesis:

My parents for the ongoing support all along and, in particular, during the process of this thesis.

PD Dr. Thilo Michel for the great supervision and for the opportunity to work on the nEXO experiment. The work has always been fascinating, sometimes tricky but all the trouble was worth it, for sure!

Prof. Dr. Gisela Anton for introducing me to the field of neutrino physics. Thank you for your brilliant support with the application for my Ph.D. fellowship.

Jutta Dziwis for being that patient with me when having messed up a business trip proposal again as well as of course the associated settlement or when asking for another special arrangement concerning a student assistant contract.

Hennry Schott for his technical support in the laboratory as well as for the interesting discussions during the remote shifts.

Ako Jamil, **Theresa Palm** and **Michael Wagenpfeil** for not just being great colleagues but rather for being great friends and for struggling with the manuscript of this thesis until the final evening.

Reimund Bayerlein, **Patrick Hufschmidt** and **Judith Schneider** and the whole **nEXO Erlangen Group** for the casual and productive working atmosphere and for their support that sometimes prevented them from concentrating on their work. Without them, many things would have taken much longer and many days would not have been that much fun.

The **EXO-200** and the **nEXO Collaboration** for providing the research opportunity on such diverse and interesting experiments and for being such a great community.

Statutory Declaration

I declare that I have developed and written the enclosed Master's Thesis completely by myself, and have not used sources or means without declaration in the text. Any thoughts from others or literal quotations are clearly marked. The Master's Thesis was not used in the same or in a similar version to achieve an academic grading or is being published elsewhere.

Erlangen, November 21, 2016

Tobias Ziegler